Nanoporous Flexographic Printing - Fundamentals, Applications and Scale-up

by

Dhanushkodi D. Mariappan

B.Tech., Indian Institute of Technology, Madras (2001)
S.M., Massachusetts Institute of Technology (2003)

Submitted to the Department of Mechanical Engineering
in partial fulfillment of the requirements for the degree of

Doctor of Philosophy in Mechanical Engineering

at the

MASSACHUSETTS INSTITUTE OF TECHNOLOGY

September 2019

Signature redacted

Author . . . .
Department of Mechanical Engineering
August 23, 2019

Signature redacted

Certified by . . . .
A. John Hart
Associate Professor of Mechanical Engineering
Thesis Supervisor
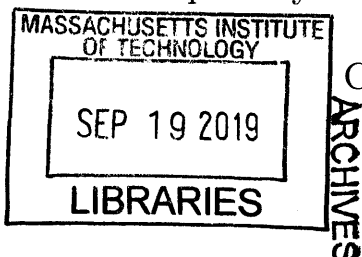
Signature redacted

Accepted by . . . .
Nicolas G. Hadjiconstantinou
Chairman, Department Committee on Graduate Theses

Nanoporous Flexographic Printing - Fundamentals, Applications and Scale-up

by

Dhanushkodi D. Mariappan

Submitted to the Department of Mechanical Engineering
on August 23, 2019, in partial fulfillment of the
requirements for the degree of
Doctor of Philosophy in Mechanical Engineering

Abstract

Printing of ultrathin layers of polymeric and colloidal inks is critical for the manufacturing of electronics on non-conventional substrates such as paper and polymer films, for applications such as smart packaging, asset tracking, and photovoltaics. Among conventional printing processes, flexography is a scalable, high-speed direct printing method, yet its resolution is limited by squeeze-out of ink between the non-porous stamp and substrate and by dewetting of the deposited ink film. Broadly, there remains an important need for improved printing technologies for ultrathin ($\sim$0.1 μm or smaller) and fine features ($\sim$ μm resolution) to advance printed electronics technology. In flexographic printing, it was recently demonstrated that significantly finer printed feature dimensions can be achieved when nanoporous stamps are used instead of traditional non-porous polymer stamps. This thesis studies the fundamentals, applications and scalability of flexography using nanoporous stamps.

- First, the dynamics of liquid transfer between nanoporous stamps and solid substrates are studied. The stamps comprise forests of polymer-coated carbon nanotubes (CNTs), and the surface mechanics and wettability of the stamp are engineered to imbibe colloidal inks and transfer patterns by conformal contact with the substrates. By high-speed imaging during printing we observe the dynamics of liquid spreading, which is mediated by progressing contact between the nanostructure stamp surface and the substrate, and by imbibition within the stamp-substrate gap. Via modeling of the liquid dynamics, and comparison with data, we elucidate the scale- and rate-limiting aspects of the process. Specifically, we find that the printed ink volume and resulting layer thickness are independent of contact pressure, and thickness decreases with retraction speed.

- Second, the design and evaluation of a benchtop plate-to-roll (P2R) machine for rapid prototyping of printed patterns is presented. The machine accommodates CNT stamps up to 20 x 20 mm size, and controls the contact force, contact

3

speed, and the alignment between the stamp and the substrate. Using the P2R machine, we show printing of honeycomb patterns with 3 μm linewidth at >0.1 m/s demonstrating the scalability of the process for high-throughput manufacturing.

- Third, simple devices are prototyped to leverage the capabilities of nanoporous flexography. Ultra-thin (<500nm), short channel (~10 μm) transistors are fabricated using flexoprinted silver electrodes (followed by sintering), with a uniform thin film of single walled carbon nanotubes (SWCNTs) as the active layer. The measured on-off ratios (~ $10^3 - 10^5$) and mobilities (25-95 cm^2/Vs) are comparable with that of other printed SWCNT network transistors. Last, two-color pixels of colloidal quantum dots with good optical absorbance are printed for potential use in filters for low-cost imaging spectrometers.

Together, the findings of this thesis suggest that flexography using nanoporous stamps is a promising approach to high-speed printing of colloidal nanoparticle inks, for manufacturing of electronic and sensing devices that require high-resolution printed features.

Thesis Supervisor: A. John Hart
Title: Associate Professor of Mechanical Engineering

Acknowledgments

My heart-felt gratitude to the following people without whom this thesis would not have been possible.

Contents

List of Figures

11

List of Tables

Chapter 1

Introduction

1.1 Printed electronics

There have been significant advances in silicon microfabrication technology since the invention of the transistors. The performance of the devices made by silicon microfabrication processes continues to advance [1, 2]. But, the process is limited to small area rigid substrates, low volume batch production, high research and development and production costs, and the need for sophisticated equipment and process controls. On the other hand, high-performance devices are not essential for several applications. [3, 4] To fabricate devices for such applications, manufacturing process requirements are complementary to that of silicon microfabrication. These include flexible substrates, large areas, low cost, and addressing fast changing product specifications. Such applications include flexible displays, solar photovoltaics, wearable devices, RFID tags, batteries, lighting solutions and sensors. There is a need for novel manufacturing processes to realize these applications.

1.2 Need for high throughput high resolution printing processes

Printing processes including screen, inkjet, gravure, flexography have been used to manufacture electronics for nearly two decades. [5–7] These processes meet the aforementioned requirements and have created a growing printed electronics industry. Yet, several of these processes are limited in their resolution (>10 μm) and control of printed layer thickness (>1 μm). Lateral resolution is an important measure of print quality that affects the performance of printed devices. For example, in transistors, shorter the channel length higher the switching speed; channel length is the spacing between the source and drain electrodes and it depends on the printing process resolution limit. Precision control of layer thickness and printing uniform layers are important in some applications. [8–10] Fully printed transistors include atleast four layers stacked on top of each other. The thickness and uniformity of the dielectric layer determines the breakdown strength and operating voltage of theses transistors. [11]

1.3 Limitations of flexography

Flexographic printing is widely used as it is a high-throughput process compatible with different substrates and inks. Printing with solid flexographic stamps causes the ink to squeeze out or dewet on the stamp surface depending on the ink volume on the stamp. [12–15] These lead to loss of pattern fidelity and limit the resolution of flexographic printing ($\sim$50-100m) with solid stamps. The transferred liquid volume is large leading to non-uniform drying and printing of thick, non-uniform layers. Due to these limitations of flexography, there is a need for high resolution, high speed printing process that can print ultra-thin layers.

1.4 Nanoporous flexography

A recent invention from our research group, engineered nanoporous stamps composed of polymer coated carbon nanotube (CNT) forests, are highly porous (>90%) and can retain the ink within their volume rather than on their surface only and can transfer highly uniform ink layers under mechanical contact [16]. Using this method, we have demonstrated direct printing of features with micron-scale lateral dimensions (<10μm), line edge roughness (<1μm) and highly uniform thickness in the sub-100nm range.

1.5 Scope of this thesis

Chapter two [16,17]describes the four process steps used to make nanoporous steps. VACNTs are grown in a CVD furnace and then exposed to plasma treatment. After plasma treatment, VACNTs are conformally coated to a tunable coating thickness. VACNTs are then treated with oxygen plasma. The chapter shows exemplary SEM images of samples before and after each of the four processing steps.

Chapter three [18] presents the dynamics of liquid transfer from nanoporous stamps during flexographic printing. A custom built high-speed, high-magnification imaging apparatus was used to capture the steps that lead to the transfer of colloidal ink from the nanoporous stamp to a substrate. The process steps developed based on the image analysis is presented. The mechanisms that govern the spreading, recession, and respreading dynamics are presented. The analytical modeling results to rationalize the experimental observations are presented. These findings provide guidance to control the uniformity and thickness of printed patterns, and to assess the potential rate and scale limits that are critical to industrial applicability of the technology.

Chapter four [16,19] describes the design and evaluation of a benchtop plate-to-roll (P2R) machine aimed to study the mechanics and rate limits of flexography using nanoporous CNT stamps.

Chapter five describes an application example where nanoporous flexographic printing is used to fabricate a thin-film transistor. The design, fabrication and characterization of a thin-film transistor with short channel lengths ($\sim 10\mu$m) and ultra-thin ($<$ 500 nm)electrodes printed using nanoporous flexographic printing is presented. The measured transistor mobility ($\sim$25-95) and on-off ratio ($\sim$103-105) are comparable with other printed SWCNT transistors.

Chapter six describes the use of nanoporous flexography for printing high-resolution pixels and color filters for QD spectrometers. As a proof of concept, two color super pixels (a sub-array of different QD color pixels) are printed with nanoporous flexographic printing

Chapter seven presents the contributions and limitations of this work. These are organized along three themes namely fundamentals, applications and scaling of nanoporous flexographic printing. Preliminary results from the work conducted to solve some of the open problems are also presented.
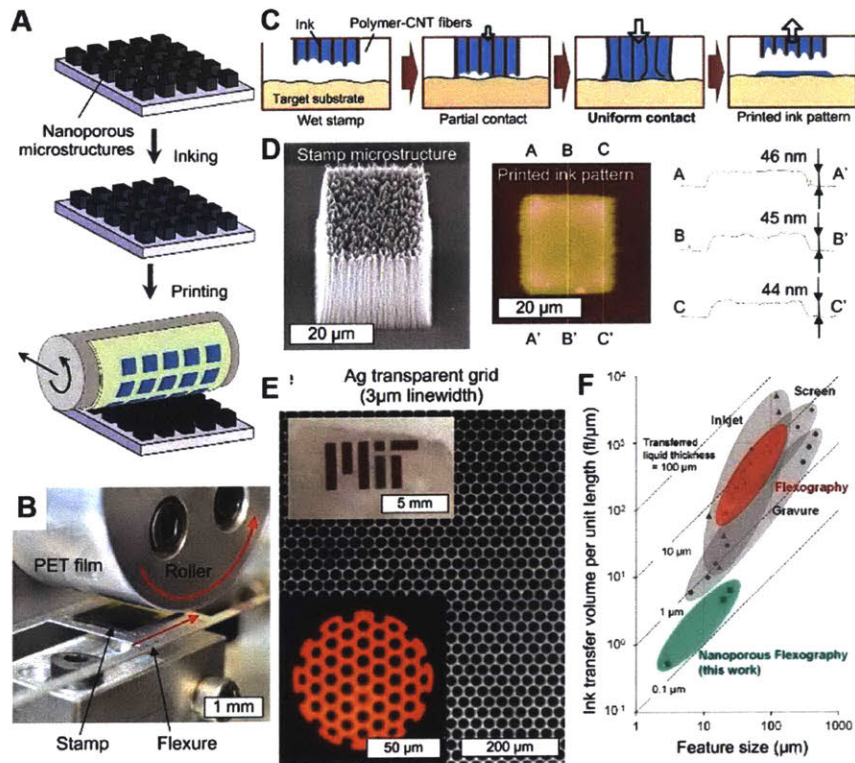
Figure 1-1: Nanoporous flexographic printing [16]: (a) simplified process sequence; (b) custom-built roll-to-plate apparatus; (c) principle of nanoscale ink transfer via conformal surface contact; (d) square stamp feature showing high-fidelity replication and uniform 50 nm thickness printed layer; (e) printed transparent Ag grids (3 um linewidth) and quantum dot pixels; (f) 10-fold improvement in transferred ink volume and minimum feature size compared to industrial flexography.

Chapter 2

Fabrication of nanoporous stamps

To fabricate the stamps [20], first vertically aligned CNT arrays (CNT forests) are grown on lithographically patterned silicon substrates by atmospheric pressure chemical vapor deposition (CVD). Then, the top entangled crust layer ($<$1 μm thickness) is removed by a brief oxygen plasma etching (Diener, Femto Plasma System) and coated with a thin layer ($\sim$20 nm) of poly-perfluorodecylacrylate (pPFDA) using initiated CVD (iCVD). [17, 20, 21]The plasma etching is critical to remove the stiff and rough crust which is not desirable for high-resolution printing because it results in non-uniform contact against the target substrate. The pPFDA coating followed by second plasma treatment allow liquid infiltration and solvent evaporation without shrinkage or collapse of the CNT forest by elastocapillary densification. The final plasma-treated pPFDA-CNT microstructures are highly porous ($>$90 % porosity) with nanometer pore size ($\sim$100-200 nm), allow liquid infiltration without deformation due to capillary forces, and are mechanically compliant, enabling uniform contact with the target substrates.

2.1 Patterning and catalyst deposition

Photolithography is used to pattern 100 mm (100) silicon wafers coated with 300nm of thermally grown SiO_2. The catalyst layer, 10 nm of Al_2O_3 and 1 nm of Fe, is deposited by electron beam physical vapor deposition. The wafer with the deposited

Step	Time (mins)	He	C_2H_4	H_2	Temperature(^{0}C)
1	5	1000	0	0	775
2	20	400	100	100	775
3	5	1000	0	0	25

Table 2.1: Dummy growth recipe

catalyst is diced into smaller wafers of 20 x 20 mm size.

2.2 CVD growth of VACNTs

Figure 2-1 shows the Chemical Vapor Deposition (CVD) furnace used to grow vertically aligned carbon nanotubes (VACNTs). The wafer is placed on boat which can be moved along the length of the tube furnace using a transfer arm. The process [22] consists of three steps

1. **Airbake**

   During the airbake step, the tube is heated for 30 minutes at 875^{0}C. After the air bake step, the tube is allowed to cool to room temperature.

2. **Dummy growth**

   During this step, CNT growth process is simulated in the tube without the sample. Table 2.1 shows the recipe used during the dummy growth step. The recipe consists of multiple steps. In each step one or more gases are flown for a set duration at a specified flow rate. Each step is either performed at room temperature or by heating the tube furnace to a higher temperature. For example, in step 2, helium, ethylene and hydrogen are flown at 400, 100 and 100 sccm for 20 minutes with the furnace at 775^{0}C.

3. **Dynamic growth**

   After dummy growth, the wafer is placed on the boat. The boat can be moved in and out of the furnace using a transfer arm. Table 2.2 lists the steps in the dynamic growth recipe. This recipe is referred to as dynamic recipe since the positioning the wafer can be changed in this process. During steps 1-4,
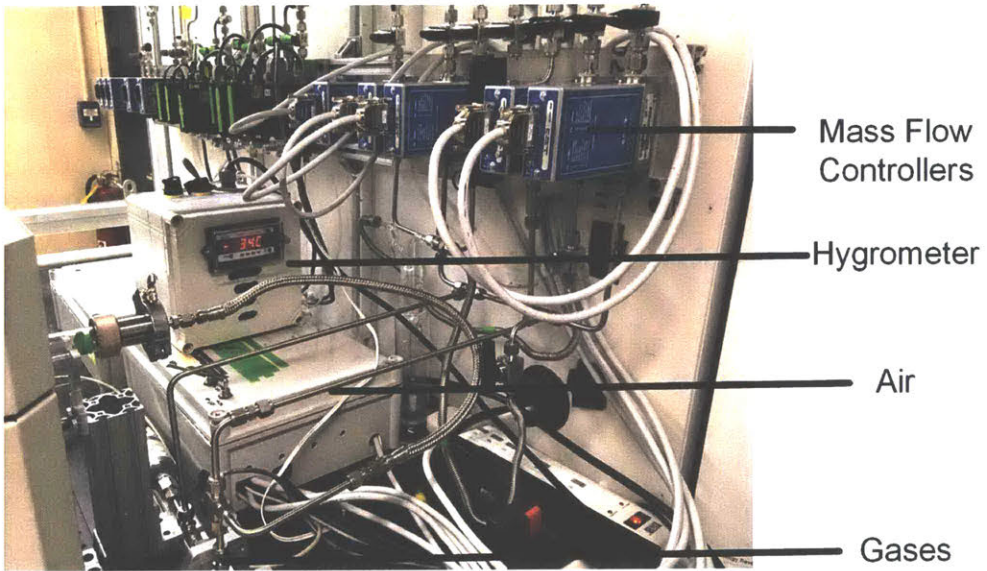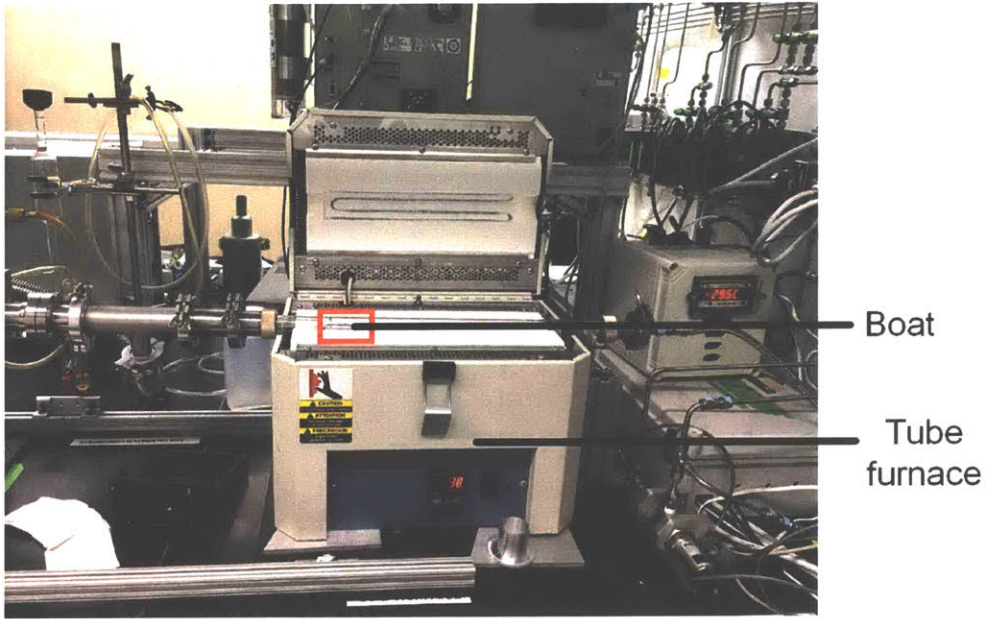
Figure 2-1: CVD Furnace in which the VACNTs are grown

Step	Time (mins)	He	C_2H_4	H_2	H_2O-He	Temperature(^{0}C)
1	3	500	100	500	100	25
2	5	1000	0	0	0	25
3	5	0	0	400	100	25
4	15	0	0	400	100	775
5	10	0	0	400	100	775
6	1	0	0	400	100	775
7	7	0	100	100	400	775
8	4	0	100	100	400	775
9	1	0	100	100	400	25
10	5	400	100	100	0	25
11	5	1000	0	0	0	25

Table 2.2: Dynamic growth recipe

wafer is kept outide the furnace. During step 5, wafer is moved to a 'sweetspot' inside the furnace and during this step, annealing is performed with the furnace temperature set at 775^{0}C and hydrogen and moisturized helium flowing through the tube. During Steps 6 and 7, the wafer is pulled out of the furnace. During step 8, which is the growth step, the wafer is pushed inside the furnace to the sweetspot. Fig. 2-2 shows the variation of furnance temperature setpoints and moisture at the gas inlet during the airbake, dummy and dynamic growth steps. Depending on the duration of step 8, the final height of the VACNTs vary and the growth rate is 100 μm /min

2.3   Plasma etching

The CVD-grown CNTs are exposed to a plasma treatment for 2.5 to 5 minutes with Argon and Oxygen flow rates of 80 and 20 sccm respectively in the Diener Femto Plasma System. The power and pressure used are 50-70Watts and 200mtorr. Figure 2-3A shows a micropillar array. Each micropillar is made of CVD grown VACNTs. Figure 2-3B shows the SEM image of the top surface of one of the micropillars. The top surface consists of crusts that are formed during the initial stages of the CNT growth. The plasma treatment removes these crusts and creates pores.Figure 2-3C
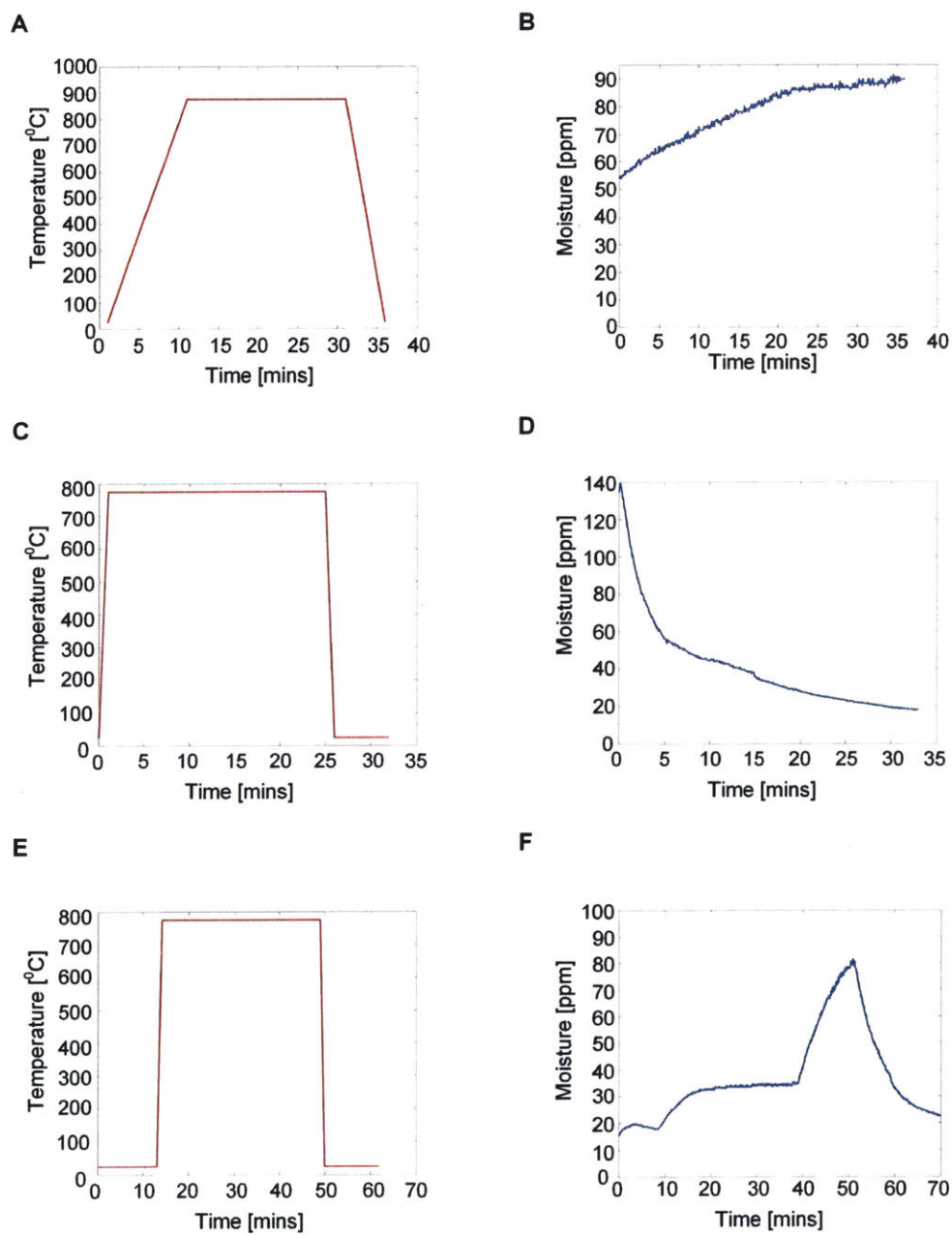
Figure 2-2: Furnace temperature and moisture level at gas inlet to the tube furnace. Furnace temperature profile A)Air bake .B) Dummy growth C)Dynamic growth Moisture level at the gas inlet to the tube furnace during D)Air bake E) Dummy growth F)Dynamic growth
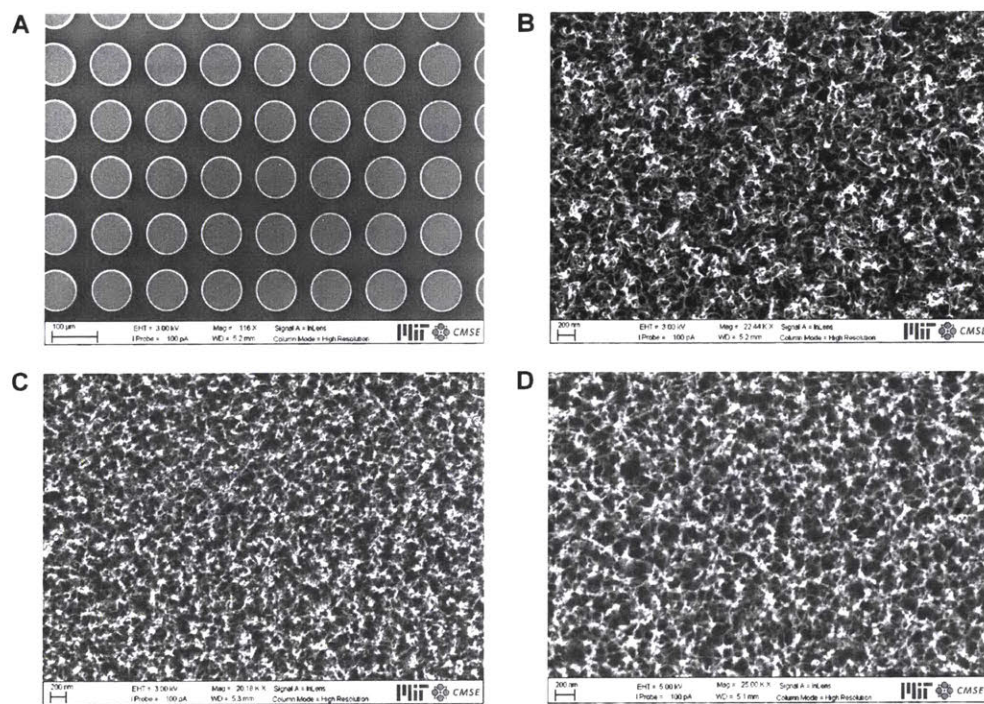
Figure 2-3: SEM images of nanoporous printing stamps at various stages of stamp fabrication A)Array of micropillars .B) Top surface of as-grown CNTs showing the crust layer C)Porous top surface after plasma etching D) Polymer coated CNT surface
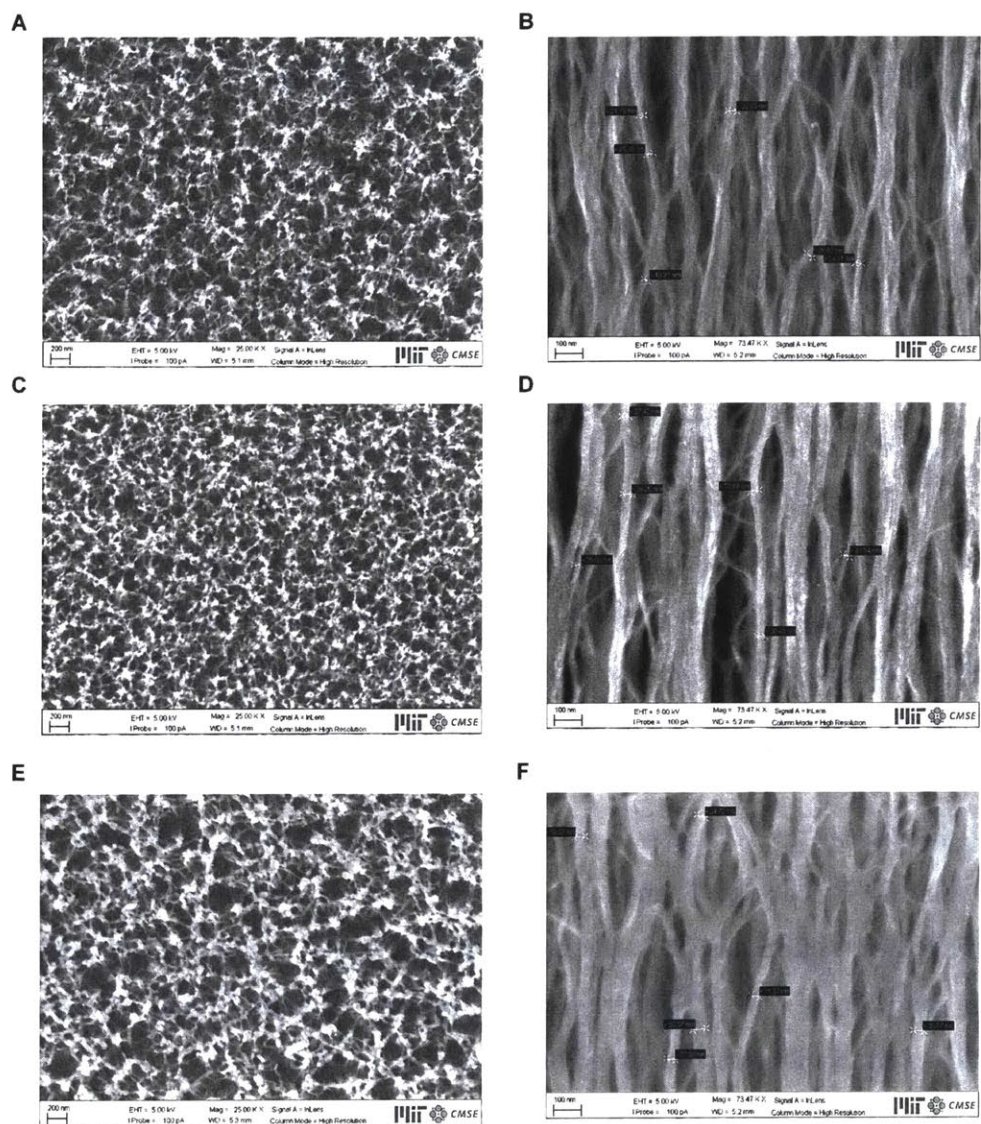
Figure 2-4: Tuning the coating thickness of CNTs using iCVD A)Top surface and side wall images of CNTs A,B) with 10nm coating thickness C,D) with 20 nm coating thickness E,F)with 30nm coating thickness

shows the SEM image of the top surface of the CNTs after the plasma treatment. A comparison of the figures 2-3B and C shows the creation of pores and the removal of crusts by plasma treatment.

2.4 Conformal polymer coating by iCVD

iCVD polymerization [16, 21] is done in a custom-built cylindrical reactor (Pancake reactor) to conformally coat the plasma etched CNTs. The reactor is maintained at a pressure of 60mTorr. The chiller maintains the substrate temperature at 30^0C. The iCVD polymerization leads to the deposition of the polymer and the reaction consists of processes A and B. In process A (insitu grafting), TBPO is kept at room temperature and is flown into the reactor at 1sccm. In process B, there are two steps : DVB and PFDA polymerization during which TBPO is flown at 3 and 1 sccm respectively. PFDA monomer is heated in a jar to 80^0C and is flown into the reactor at 0.2 sccm. Heating filaments placed on the top surface of the reactor are maintained at 250^0C, the temperature at which the peroxide bonds of TBPO are broken forming TBO, the initiator for the polymerization. A He-Ne laser signal source and detector are used to measure the coating thickness on a silicon chip placed inside the reactor using interferometry. It takes nearly 25 minutes to deposit a 30nm thick PFDA film. The CNT coating thickness can be varied by varying the deposition time and stopping the reaction based on the interferometer signal. ?? shows the SEM images of the sidewalls of VACNTs with varying coating thicknesses. The stamp porosity and flow permeability can be tuned using coating thickness.

2.5 Oxygen plasma etching

The polymer coated CNTs are hydrophobic preventing wetting and imbibition of liquid inks into the pores of the CNTs. The polymer coated CNTs are subject to oxygen plasma treatment to make them hydrophilic. The oxygen plasma treatment is performed in the Diener Femto Plasma system. The powere and pressure are

30Watts and 200mtorr. The flow rates of Oxygen and Argon are 20sccm and 80sccm respectively. For some samples, these conditions do not provide enough wettability. In such cases, oxygen flow rate and treatment time are increased to 40 sccm and 5 minutes respectively.

2.6   Conclusions

In this chapter, we described the process steps used to fabricate the nanoporous stamps. We have described the CVD process steps and conditions used to grow vertically aligned carbon nanotubes (VACNTs). After growth, the surface of the CNTs are treated with O_2/Ar plasma, following which the VACNTs are conformally coated with a polymer (pPFDA) in a reactor via iCVD polymerization process. Finally, the stamp wettability is achieved by subjecting the stamps to O_2 plasma treatment. The scanning electron microscope images of the top surface and sides of the CNTs and polymer coated CNTs enabled characterizing the samples. We show exemplary images of the samples after each of the processing steps. The images are used to assess the quality of the samples and identify defects introduced during each of the processing steps. We used these steps to fabricate stamps for the experiments conducted to study the dynamics of ink transfer (Chapter 3), validation experiments for the plate to roll printing apparatus(Chapter 4), and fabrication and characterization of transistors (Chapter 5).

Chapter 3

Dynamics of Liquid Transfer from Nanoporous Stamps in High-resolution Flexographic Printing

The contents of this chapter were published [18] as Dynamics of liquid transfer in nanoporous stamps in high-resolution flexographic printing.

3.1 Abstract

Printing of ultrathin layers of polymeric and colloidal inks is critical for the manufacturing of electronics on non-conventional substrates such as paper and polymer films. Recently, we found that nanoporous stamps overcome key limitations of traditional polymer stamps in flexographic printing, namely enabling the printing of ultrathin nanoparticle films with micron-scale lateral precision. Here, we study the dynamics of liquid transfer between nanoporous stamps and solid substrates. The stamps comprise a forest of polymer-coated carbon nanotubes (CNTs), and the surface mechanics and wettability of the stamp are engineered to imbibe colloidal inks and transfer patterns by conformal contact with the substrates. By high-speed imaging during printing we

observe the dynamics of liquid spreading, which is mediated by progressing contact between the nanostructured stamp surface and the substrate and imbibition within the stamp-substrate gap. From the final contact area, the volume of ink transfer is mediated by rupture of a capillary bridge; and, after rupture, liquid spreads to fill the area defined by a precursor film matching the stamp geometry with high precision. Via modeling of the liquid dynamics, and comparison with data, we elucidate the scale- and rate-limiting aspects of the process. Specifically, we find that the printed ink volume and resulting layer thickness are independent of contact pressure; and thickness decreases with retraction speed. Our results show that nanoparticle films with tailored thickness in the < 100 nm regime can be printed using nanoporous stamp flexography, at speeds commensurate with industrial equipment.

3.2 Introduction

High-throughput printing of electronic materials is critical to mass production of devices including thin film transistors, [23–27]RFID tags, [28] and transparent electrodes, for use in applications such as smart packaging, [29–32]asset tracking, and photovoltaics. [33, 34] Typically, the desired formats of printed electronics contrast those of wafer-based semiconductor fabrication, demanding lower manufacturing cost and large-area compatibility. [27, 35–38]Many traditional printing technologies including inkjet, flexography, gravure, slot die coating, and screen printing have been adapted to printing of inks suited as precursors to functional thin films. The performance of devices such as printed transistors, and the resolution of printed display pixels, is in particular limited by the performance of extant printing methods. For instance, flexography (Fig. 3-1A) is a highly scalable, high-speed direct printing method, yet it is limited to resolutions of 10s of microns [39] as a result of the ink being squeezed out [12, 13] between the stamp and substrate and due to dewetting of the deposited ink film. [14]Broadly, there remains an important need for improved printing technologies for ultrathin ($\sim$0.1μm or smaller) and fine features ($\sim$ μm resolution) to advance printed electronics technology. Most of the aforementioned printing technologies use

liquid or polymeric inks, often containing colloidal nanoparticles that are sintered to form films after drying of the printed ink pattern. As such, limitations to the feature size and thickness are attributed to the coupled, time-dependent fluid and solid mechanics of the printing process. In flexographic printing, we recently demonstrated that significantly finer printed feature dimensions can be achieved when nanoporous stamps are used instead of traditional non-porous polymer stamps. [20] The key difference is that nanoporous stamps retain the ink within their volume (Fig. 3-1B), enabling the printed pattern to precisely replicate the shape of stamp features without suffering the squeeze-out and dewetting instabilities of traditional flexography. For instance, nanoporous stamps comprising polymer-coated vertically aligned carbon nanotubes (CNTs) enabled high speed (0.1 m/s) printing of features with 3μm minimum size, from conductive, dielectric, and semiconducting nanoparticle inks.

In traditional flexography, when the elastomer printing stamp is brought into contact with the substrate, the ink on the surface of the stamp forms a liquid bridge between the stamp and the substrate. As the stamp and substrate are separated, the liquid bridge ruptures and a small volume of liquid is transfered to the substrate under each stamp feature. Early studies of liquid transfer in flexography, using millimeter-scale features and glycerol showed that the relative contact angles between the liquid and the surfaces determined the transfer fraction under quasi-static conditions. [40, 41] Fast separation led to the liquid separating equally between the two surfaces irrespective of the wettability. [42] Experiments using distilled water, PMMA stamps, and a variety of acceptor surfaces established that the difference in the receding contact angles of the donor and acceptor surfaces determines the transfer ratio at low separation speeds. [43–45] Amirfazli et al. also studied the combined effects of inertia, ink viscosity, and receding contact angles on the liquid transfer and developed empirical relations for the transfer ratio as a function of capillary number ($Ca = 10^{-7}$ to 1), Reynolds number ($Re = 10^{-8}$ to 10^2) and contact angles ($\theta = 30^0$ to 113^0). [46 48]Qian and Breuer [49]developed mathematical models validated by their experiments to study the liquid transfer from a constant volume liquid bridge between a donor surface where the contact line is pinned and a hydrophobic acceptor surface
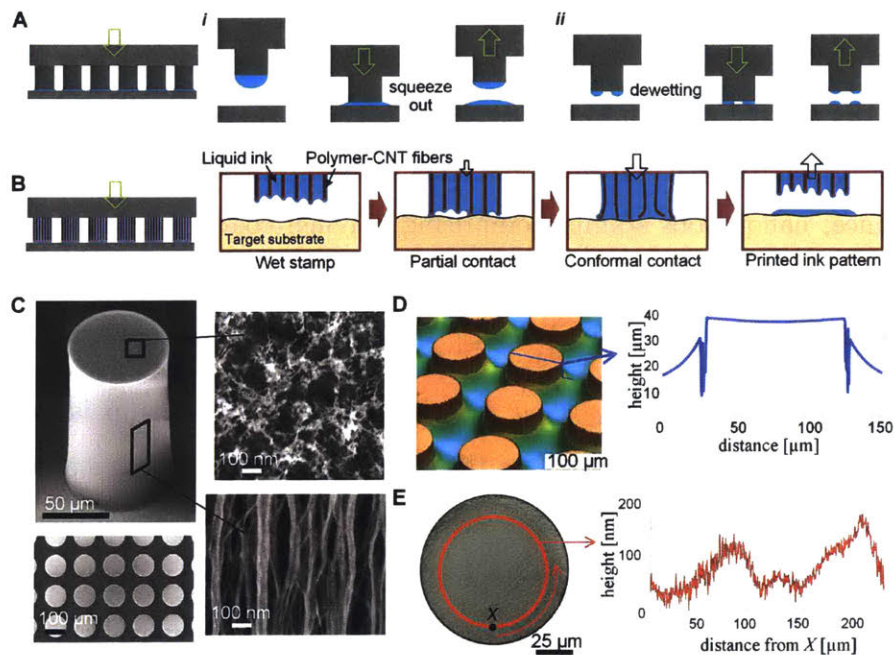
Figure 3-1: Nanoporous stamps for ultrathin flexographic printing. (A) Spreadout and film dewetting lead to loss of resolution and uniformity in flexography with non-porous elastomer stamps. (B) Simplified schematic of ink transfer from CNT micropillar stamp loaded with ink. (C) SEM images of typical circular CNT micropillar array (100 μm pillar diameter, 150 μm height) used for nanoporous flexography; close-up top and side surfaces of a micropillar reveal pores with 100 nm width. (D) Confocal microscope images of the stamp after infiltration of Ag (in tetradecane) nanoparticle ink. The 2D profile shows the wetted liquid surface around the stamp pattern. (E) Top view confocal microscope image of a single micropillar, and height profile extracted from the image.

where the contact line is free to move. They used stability analysis to predict the onset of contact line motion and the onset of bridge rupture, and thereby predicted the influence of drop volume on the transfer ratio. In summary, at low speeds, the receding contact angles on the two surfaces determine the ink transfer ratio, with a greater fraction remaining on the surface with higher wettability. As the speed increases, the process becomes less dependent on surface properties and the transfer ratio tends towards 50%. The transfer ratio decreases at even higher speeds due to volume lost to the formation of satellite droplets during rupture. Yet, non-uniform drying and capillary flow produce printed features with non-uniform thickness, which remains a limitation to practical use of flexography in printed electronics. Using nanoporous stamps, we may expect that the relative wettability and separation speed will similarly be important, yet the role of the stamp texture and porosity on the formation and recession of the liquid-solid interface during printing, can influence the speed limits of the process as well as the amount of ink transferred. Here, we study the dynamics of ink transfer between nanoporous stamps and solid substrates. We capture the printing process with a high-speed, high-magnification imaging apparatus positioned behind a transparent substrate. Based on image analysis, and analytical modeling, we then discuss the dynamics of ink spreading, recession, and re-spreading during printing. These findings provide guidance to control the uniformity and thickness of printed patterns, and to assess the potential rate and scale limits that are critical to industrial applicability of the technology.

3.3 Methods

3.3.1 Visualized printing experiments

The experimental setup was designed to accommodate CNT stamps up to 20 x 20 mm in size, and to control the contact force, stamp approach and retraction speeds, and the alignment between the stamp and the substrate. During printing, the CNT stamp is placed on the flexure stage, and the printing substrate is placed in a circular

slot of an acrylic fixture. The flexure is clamped at its ends and a capacitance probe placed between the flexure holder and the flexure is used to measure the deflection and set the contact force between the stamp and substrate. The flexure holder is attached to a single axis motion stage via a tip-tilt stage which is used to align the stamp with the substrate. The printing substrate is a spherical lens. A custom-built microscope along with a high speed camera (Vision Research, Phatom v2511) was placed behind the substrate and was used to take videos during the printing experiments. The dry stamp is placed on the flexure and is brought into contact with the spherical lens so that the contact pressure on the stamp is within the range [20] required to achieve conformal contact and the stamp is aligned with the substrate. The stage displacement required to achieve the contact pressure is recorded and the stamp is removed from the flexure. After inking and excess ink removal, as outlined in the inking section, the wet stamp is placed on the flexure and brought into contact with the lens. During such a printing step including stamp approach and retraction, high speed videos are recorded at up to $\sim$25,000 frames per second.

3.3.2 Stamp fabrication

To fabricate the stamps [20], first vertically aligned CNT arrays (CNT forests) are grown on lithographically patterned silicon substrates by atmospheric pressure chemical vapor deposition (CVD). Then, the top entangled crust layer ($<1\mu$m thickness) is removed by a brief oxygen plasma etching (Diener, Femto Plasma System) and coated with a thin layer ($\sim$20 nm) of poly-perfluorodecylacrylate (pPFDA) using initiated CVD (iCVD). [17, 20, 21]The plasma etching is critical to remove the stiff and rough crust which is not desirable for high-resolution printing because it results in non-uniform contact against the target substrate. The pPFDA coating followed by second plasma treatment allow liquid infiltration and solvent evaporation without shrinkage or collapse of the CNT forest by elastocapillary densification. The final plasma-treated pPFDA-CNT microstructures are highly porous ($>$90 % porosity) with nanometer pore size (100-200 nm), allow liquid infiltration without deformation due to capillary forces, and are mechanically compliant, enabling uniform contact

with the target substrates.

3.3.3 Inking

The ink used in this study is composed of silver nanoparticles dispersed in tetradecane (Sigma-Aldrich, 736511). The surface tension and viscosity of the ink are 27 mN/m and 10 mPa-s, respectively, and the ink exhibits good conductivity (30-60% of bulk silver) after annealing. [20] The particle concentration is 50-60 wt% with particle sizes less than 10 nm. A 100 μl droplet of ink is pipetted onto the stamp and then the stamp is spun to 1500 rpm for 1-3 minutes in a spincoater.

3.4 Results and Discussion

Nanoporous stamps are fabricated by chemical vapor deposition (CVD) growth of CNT forests from a lithographically patterned catalyst film on a silicon wafer (see Methods). An exemplary stamp with an array of cylindrical micropillars is shown in Fig. 3-1C. The mechanical compliance, surface roughness, and wettability of the stamp structures are tailored via plasma treatment of the CNTs and subsequent coating with a thin layer of polymer (pPFDA, 20 nm) by initiated chemical vapor deposition (iCVD). [17, 20, 21] The combined treatment allows liquid inks to wick inside the structures without significant densification or swelling (Fig. 3-1D and E). The wet stamp has ink infiltrated in the stamp microstructures and in the gaps between the stamp features as shown in the microscope image (Fig. 3-1D) taken using a laser scanning confocal microscope (Keyence, VK-X250). In order to remove the ink in the gaps, we bring the wet stamp into contact with another stamp consisting of CNT forests with no patterns in them, as described in our previous work. [20] The stamp after the removal of excess ink has ink wetting the stamp surface conformally as shown in the confocal microscope image (Fig. 3-1E).

Ink transfer from the nanoporous stamps to glass substrates is visualized using a custom-built printing apparatus integrated with a high magnification, high speed imaging system (Fig. 3-2A). A colloidal silver nanoparticle ink (Sigma Aldrich, <10
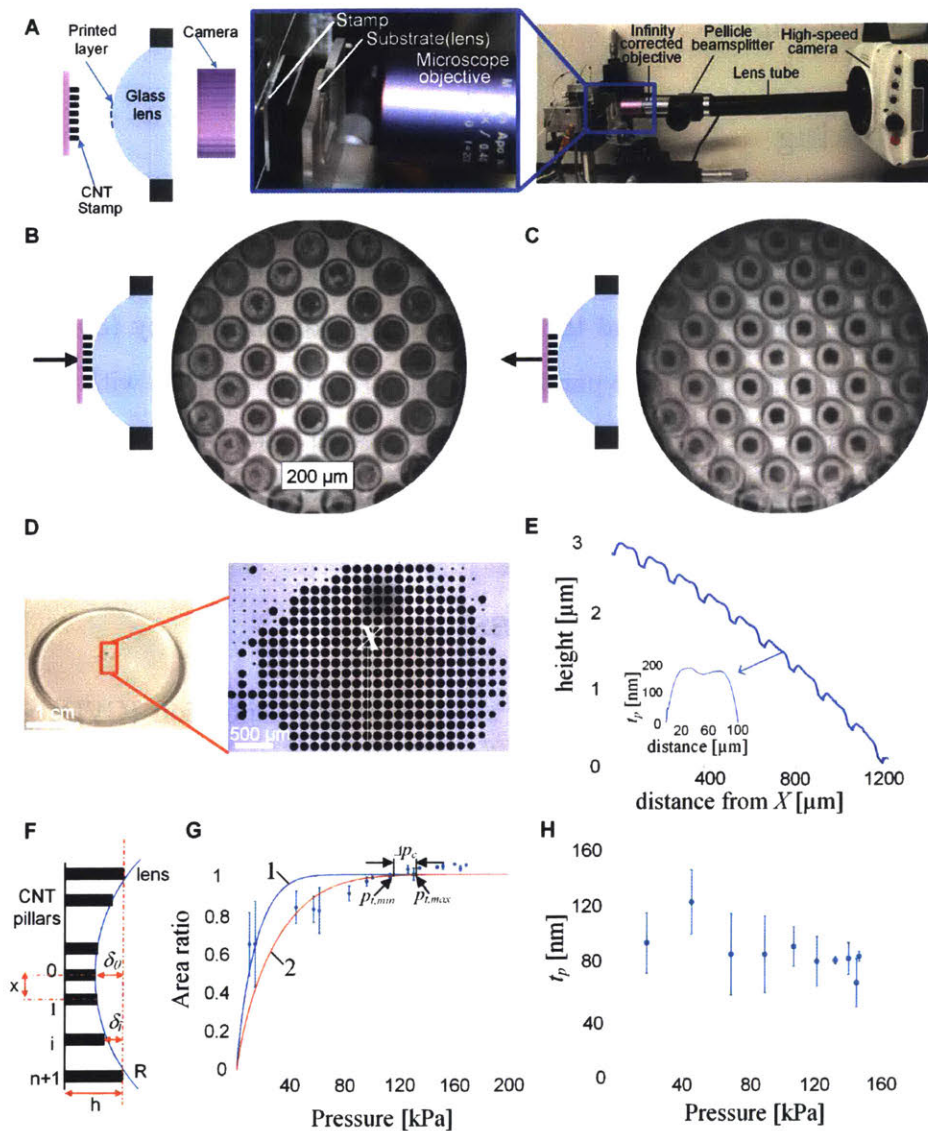
Figure 3-2: Experimental setup and procedures for visualization of liquid transfer. (A) Apparatus where contact between the stamp and a spherical lens is imaged through the back side of the lens using a high speed camera. (B, C) Snapshots from an exemplary experiment during approach of the stamp and retraction of the stamp from the lens, respectively. The stamp pattern is an array of 100 μm circles with 30 μm spacing, and the experiment is shown in Videos S1 and S2. (D) Pattern printed onto the lens. (E) Surface profile of the printed patterns measured by a stylus profilometer after solvent evaporation, along the line indicated in (E). (F) Schematic showing the compression of stamp pillars when in contact with the spherical lens. (G) Calculated area ratio of patterns printed on lens versus contact pressure and comparison with contact model (λ_{CNT}=45nm, σ_l =30 nm and λ_{CNT}=45nm, σ_l =15nm are the parameter values in Models 1 and 2 respectively [16]). (H) Measured thickness of printed layers versus calculated contact pressure at the retraction speed of 0.3 mm/s.

nm in tetradecane, 50-60 wt%) was used in all experiments, and the ink was applied to the stamp by pipetting a 100 drop on the stamp followed by spin coating at 1500 rpm for 3 minutes. [20] In each experiment, an inked stamp was brought into contact with a spherical glass lens (0.50 m radius, ThorLabs) with a prescribed velocity and stopped when a prescribed force was reached (see Methods). Contact was maintained at the specified force for 10 seconds, then the stamp was retracted from the lens with a second prescribed velocity. The stamp-substrate interface was viewed through the back (flat) side of the lens during the entire printing process (Figs. 3-1B,C and Videos S1 and S2). The convex curvature of the lens ensured a contact region with locally uniform pressure, being essentially flat in comparison to the size of the individual stamp micropillars. In Fig. 3-2D and Fig. 3-2E we show an exemplary printed pattern and thickness profile on the lens after solvent evaporation. When the micropillar array stamp contacts the lens, each micropillar prints a circular feature, and is compressed by an amount determined by the position of the stamp along the motion axis and the local position of the lens surface where it contacts the micropillar (Fig. 3-2F). As a result, a single experiment creates an array of printed features under locally different contact pressures, and correlations between contact pressure, print thickness, and print area (relative to the micropillar area) are assessed (Figs. 3-2G,H). The print area ratio (ratio of area of stamp pattern to printed pattern) increases with contact pressure (Fig. 3-2G) whereas the measured thickness (Fig. 3-2H) of the printed layers is not influenced by the contact pressure. Thus, the videos must be used to understand the dynamics of ink transfer. From the videos, we identify the dynamics of contact and ink transfer between the stamp and substrate, as shown in Fig. 3-3 and Videos S3a-c, S4a-c, S5a,5b, for individual inked micropillars with circular, annular, and square shapes. Upon initial contact between the micropillar and substrate, wetting initiates; the position of contact is determined by the surface profile of the micropillar stamp, which has a waviness of ~ 1 micron over 100 microns. Then, liquid spreads outward to fill the gap between the stamp and substrate, while the stamp continues to approach the surface. For the circular micropillar (Fig. 3-3B) of radius r_s, liquid spreads radially outward $(r(t))$. For the annular stamp (Fig. 3-3C), initial contact

occurred along the outer circumference, followed by liquid spreading along a ring which expanded to fill the annulus. For the square stamp (Fig. 3-3D), spreading began near the left edge of the image, then reached the top and bottom edges, and then swept to the right. In all cases, the rate and direction of spreading is influenced by the local gap height and stamp waviness, until spreading stops when the liquid is pinned by the edge of the stamp feature. According to the experiment procedure, motion of the stamp is stopped when the prescribed contact pressure is reached; here, the local pressure ensured that the stamp contact area became fully wetted. Contact may remain partial if the pressure is insufficient, which results in incomplete wetting and thus non-uniform printing. [20] When retraction of the stamp begins, a liquid bridge forms, pinned to the edges of the stamp and filling the small gap. As retraction continues, the liquid bridge recedes inward until it ruptures and leaves a droplet on the substrate. After rupture of the liquid bridge, the separated drop respreads back to the original shape that was wetted during stamp contact. This behavior is particularly evident when we observe the annular and square stamps, and appears to be critical to the shape fidelity of the printing process. Below we further discuss each stage of observation, and understand the governing attributes of the liquid transfer dynamics and the printed liquid volume.

3.4.1 Initial contact $(r_i \ll r_s)$

At the instant of first contact between a small area of the stamp and the substrate, a liquid bridge forms, as in Fig. 3-4A. If the stamp is inked conformally (Fig. 3-1D), such that there is not an excess layer of liquid on its top surface, [20] the point of initial contact is the highest point on the stamp determined by the waviness of the polymer-coated CNT forest. The stamp may have micron-scale waviness due to non-uniformity in the CNT growth, and has nanoscale roughness (Fig. 3-1E, 50nm) due to the height variation of the CNTs after growth, coating, and plasma treatment. Stamp waviness and angular alignment with the substrate both produce micron-scale variations in gap height across the stamp feature, and collectively determine the initial gap height (h_a) at which the liquid bridge forms.
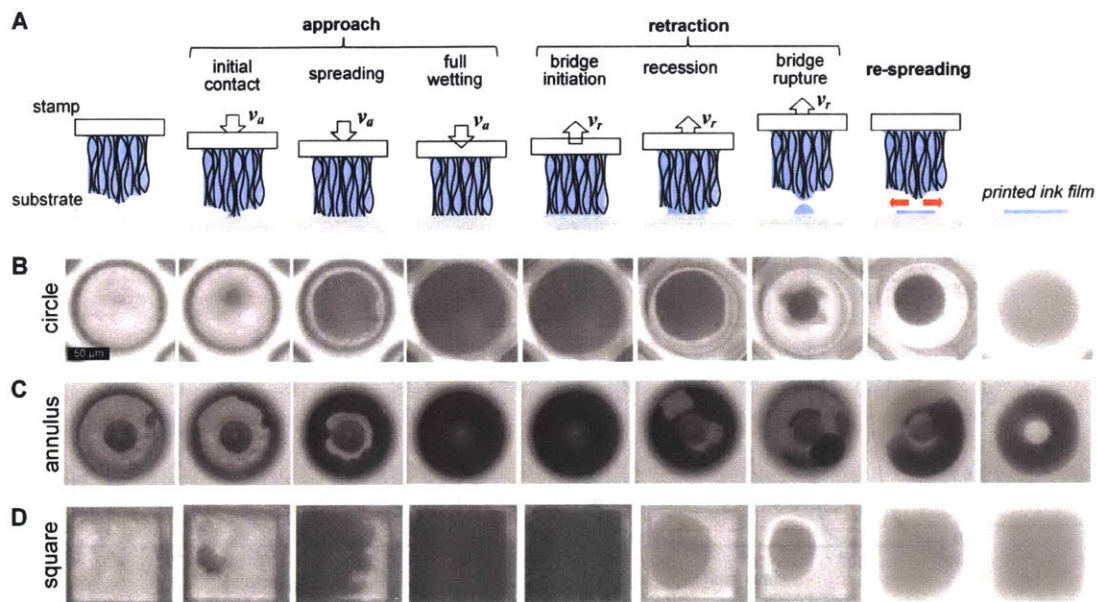
Figure 3-3: Visualization of ink transfer. (A) Schematic sequence of steps as observed by high-speed imaging. Images corresponding to each step from videos of (B) 100 μm circular stamp (videos in S3a-c) (C) annular stamp with 100 μm outer diameter and 30 μm inner diameter (videos in S4a-c), and (D) square with 100 μm side length. (videos in S5a,b).
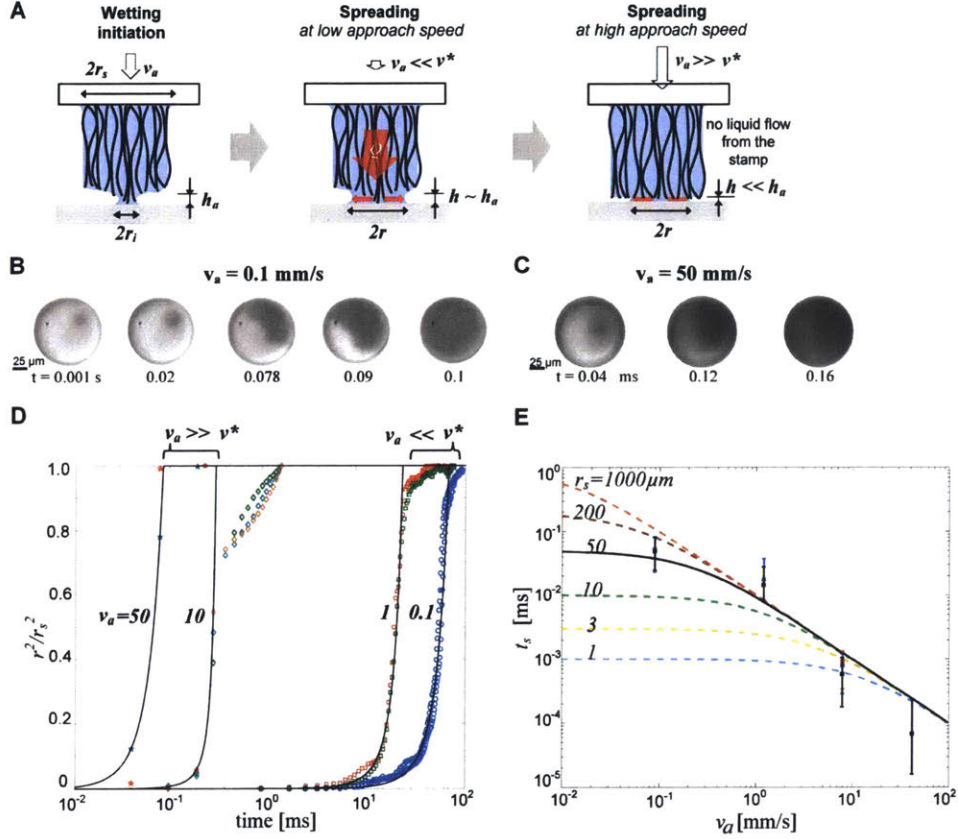
Figure 3-4: Spreading dynamics during the stamp approach. (A) Schematics of liquid spreading at the contact interface as the stamp approaches the substrate - Wetting initiation and spreading at low ($v_a \ll v^*$) and high approach speeds ($v_a \gg v^*$). (B) Snapshots from the high speed videos showing the liquid spreading on the substrate at different approach speeds of 0.1 mm/s (C) and 50 mm/s. (D) Ratio of the area covered by spread liquid to stamp area plotted as a function of time elapsed since wetting initiation for four different approach speeds, 0.1, 1, 10, 50 mm/s, (solid lines are based on Eq. 3.2 and dots represent experimental data from videos shown in S6a-d). (E) Average spreading time of the liquid versus stamp approach speed (dashed lines show modeling predictions for different stamp radii and the solid line is that for stamp radius of 50 μm. The dots and error bars are the average and standard deviation of experimental data using stamp radius of 50 μm).

3.4.2 Spreading $(r_i < r < r_s)$

Spreading (Fig. 3-4B) between the nanoporous stamp and substrate is fundamentally different from that between two solid surfaces [13,43,45–47,49](as in classical flexography); here, one surface is porous and filled with liquid, allowing a liquid supply to the gap during spreading. Accordingly, the volume of liquid between the stamp and the substrate may continuously change during the spreading step. Considering a small volume of liquid in a gap closing at constant speed (v_a) with height of $h = h_a - v_a t$, we equate the rate of volume change of liquid within the gap to the flow rate from the porous medium,

$$\frac{d}{dt}\pi r^2 h = \frac{4\Delta P\sqrt{\kappa_{zz}\kappa_{rr}}}{\mu r} \tag{3.1}$$

Here, ΔP [Pa] is the pressure difference from deep in the porous stamp to the outer radius of the liquid meniscus in the gap, μ [Pa-s] is the ink viscosity, and κ_{zz} and κ_{rr} [m^2] are the axial and radial permeabilities of the stamp. The term on the right is the approximate flow rate from a semi-infinite, anisotropic porous medium driven by a pressure difference. [50–52]We approximate the stamp near the contact interface as a porous medium consisting of parallel cylinders, [51] for which, to leading order, $\kappa_{rr} = \frac{\kappa_{zz}}{2}$. The pressure in the gap is lower than that in the stamp, and this difference provides the driving force for ink flow during spreading. The pressure difference is estimated as $\frac{\gamma}{\lambda_{CNT}}$, where γ [N/m] is the surface tension of the ink and λ_{CNT} is the CNT-CNT spacing, and is taken to be constant during spreading. Solving Eq. 3.1 we derive the time-varying radius of ink in the gap as

$$\frac{r}{r_s} = \frac{2v^*}{v_a}(1 - \frac{v_a t}{h_a})^{-\frac{1}{2}} - \frac{2v^*}{v_a} \tag{3.2}$$

where v^* is a critical velocity,

$$v^* = \frac{2\Delta P\sqrt{\kappa_{zz}\kappa_{rr}}}{\pi\mu r_s} \tag{3.3}$$

To validate this model, we conducted printing experiments at approach speeds ranging from 0.1- 50 mm/s. From the high-speed video images (Figs. 3-4B, C), an

43

effective spreading radius is extracted and compared to the model (Fig. 3-4D). For $r^2/r_s^2 < 0.95$, the model captures the general trends in the experimentally measured spreading profiles for both low and high approach speeds. Here, v^* and h_a are used as fitting parameters to match the model to the measured curves. Ink loading determines the precise value of ink pressure within the stamp (ΔP) and will contribute to variations in v^* (3.3) between prints. As r^2/r_s^2 approaches unity, spreading slows and our model does not account for how the liquid comes to rest. One contributing factor is the approximation of symmetric spreading; while we model spreading as always starting at the center of a radially symmetric geometry, the initial liquid bridge usually initiates at least slightly off-center, as seen in Figs. 3-4B,C. Therefore, at short times relative to the total spreading time the radial approximation is valid, yet once the ink reaches an edge the spreading becomes asymmetric and deviates from the model predictions. Since ink does not flow beyond the edge, the average spreading rate slows, as seen at later times in Fig. 3-4D. Moreover, at low approach speeds, the rate of spreading is approximately constant, while at higher approach speeds, the rate of spreading is proportional to approach speed, Fig. 3-4E. We classify these as capillary- and compression-driven spreading, respectively. Defining the average velocity of the spreading meniscus $v_s = r_s/t_s$, where t_s the total spreading time, 3.1 gives,

$$\frac{v_s}{v^*} = \frac{r_s}{h_a}\frac{v_a}{v^*}(1 - (1 + \frac{v_a}{2v^*})^{-2})^{-1} \tag{3.4}$$

By taking low and high speed limits of Eq. 2,

$$v_s = \frac{r_s}{h_a}v^* \tag{3.5}$$

when $\frac{v_a}{v^*} \ll 1$

$$v_s = \frac{r_s}{h_a}v_a \tag{3.6}$$

when $\frac{v_a}{v^*} \gg 1$

Therefore, when $v_a << v^*$, capillary-driven flow from the porous stamp dominates the spreading rate, and spreading can be approximated as if the stamp was station-

ary (Fig. 3-4B). For $v_a \gg v^*$, however, the gap is closing at a much faster rate than the rate at which ink can flow from the stamp (Fig. 3-4C). In this regime, an initial liquid bridge that wets across the gap will undergo approximately constant volume deformation with negligible ink flow from the stamp during spreading. Therefore, the spreading rate is simply determined by the ratio of feature width to initial gap distance and is proportional to the approach speed. Importantly, at high speeds, the spreading rate is independent of liquid properties and stamp porosity. We estimated $v^* = 0.3$ mm/s using the known ink properties and approximating the stamp permeability using an analytical expression for an array of aligned cylinders [51]. This is in reasonable agreement with the value of $v^* = 0.2$ mm/s used to fit the model to the measured data in Fig. 3-4E. Differences arise due to the precise value of ink pressure within the stamp, the distribution of CNT diameters and imperfect alignment, the modeling assumption of symmetric ink spreading, and experimental uncertainty.

3.4.3 Full wetting and contact dwell time $(r \approx r_s)$

After the stamp comes to rest, the equilibrium shape of the wetted area is determined by the contact pressure on the micropillar, and by the uniformity of the stamp relative to the opposite surface. Fig. 3-2G shows the pressure range (Δp_c) where the area ratio (ratio of area of stamp pattern to printed pattern) is ~ 1 using the measurements of printed patterns on the spherical lens and comparison with the predictive model. [16] Below the minimum threshold contact pressure $(p_{t,min})$ at the lower limit of the pressure range (Δp_c), at the end of the approach step, contact area is less than the stamp cross sectional area and there are regions in the stamp-substrate interface where the gap is $\gg \lambda_{CNT}$. Therefore, there is no driving force for the flow of liquid from the stamp even with long dwell times and the wetted area is smaller than the stamp cross sectional area producing incomplete pattern transfer. Above the maximum threshold contact pressure $(p_{t,max})$ at the upper limit of the pressure range, excess stamp compression will squeeze out additional ink into the space between stamp features, forcing wetting over a larger area than defined by the stamp feature and resulting in oversized printed features. Therefore, when the contact pressure on the

45

micropillar lies within the range (Δp_c), the nanoporous stamp fully contacts the opposite surface, i.e., coated CNTs are in contact throughout the area of the stamp feature. After contact, the stamp is held against the substrate at constant force before being pulled away. During this period, the ink meniscus can relax to an equilibrium shape $(\Delta P = 0)$ through visco-capillary flow into or out of the stamp features. The relaxation likely occurs much faster than the 10 s contact time used in the experiments reported here, but has not been characterized. A long contact time was used to decouple the approach and retraction stages of the printing process, but a much shorter dwell time may be used in practice and is unlikely to affect the printing results if full contact is achieved.

3.4.4 Retraction $(r_r < r \leq r_s)$

Starting from the condition of full contact and wetting of the interface, a thin liquid bridge is initially drawn from the stamp upon retraction, and is pinned to the substrate at the edges of the stamp feature (Fig. 3-5A). At this instant, the wetted contact area remains constant while the contact angle of the ink with the substrate decreases to the receding angle. The height of the liquid bridge within the gap when the contact line first begins to move (h_r) defines the initial volume of ink in the gap during recession. Then, the retraction speed, v_r influences the balance between liquid bridge deformation and the flow from the porous stamp. At low retraction speeds, liquid flow from the stamp will be sufficient to maintain a filled gap between the stamp feature and the substrate as the stamp moves upward. The ink volume in the gap maintains a constant radius of $r = r_s$ until the aspect ratio of the liquid bridge exceeds the stability limit, and the bridge ruptures. Equating the volume flow rate from the stamp on the right side of Eq. 3.1 to the rate of volume increase in the gap, this low speed regime is predicted for $v_r < 2v^*$. However, during retraction v^* may differ from that during the approach, because it is proportional to ΔP (Eq. 3.3) which has decreased during the contact dwell time.

For $v_r > 2v^*$, the meniscus will recede despite capillary pressure driven flow from the porous stamp. The radius of the receding contact can be approximated by the
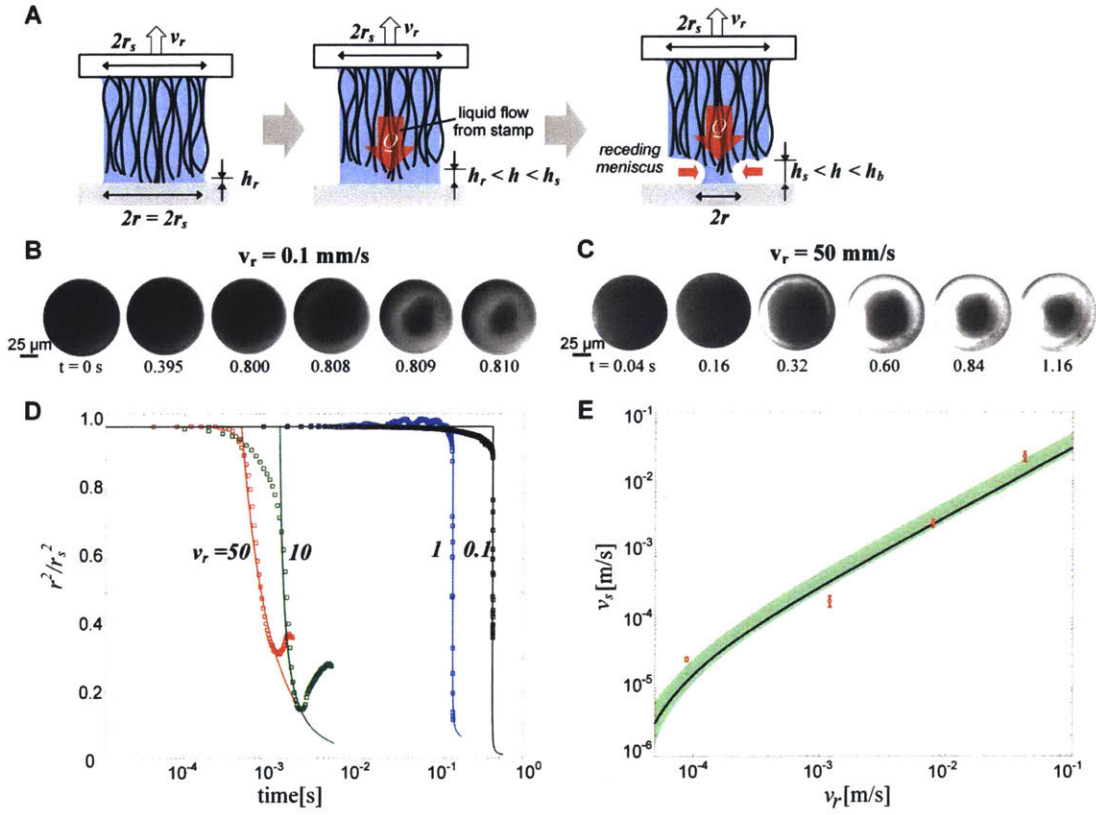
Figure 3-5: Receding dynamics during the stamp retraction. (A) Schematics of the liquid bridge initiation as the stamp retracts away from the substrate, contact line pinning and recession during retraction. (B) Snapshots showing the base of the liquid bridge on the substrate at low and high retraction speeds of 0.1 mm/s (C) and 50 mm/s. (D) Ratio of the area covered by liquid to the feature area plotted as a function of time for four different retraction speeds, 0.1, 1, 10, 50 mm/s, (solid lines are based on Eq.6, full videos shown in S7a-d). (E) The average recession speed of the liquid bridge versus stamp retraction speed. (The bounds of the shaded region show model predictions of $r_s/h_a = 10$, $v^* = 0.012$ mm/s and $r_s/h_a = 2$, $v^* = 0.02$ mm/s. The dots and error bars are the velocity calculated from the video observation)

same method as for spreading, except here the gap height, $h = h_r + v_r t$, is increasing at a constant speed. Designating the gap height at which the ink radius begins to recede as h_r, Eq. 3.1 predicts that the ink radius decreases as

$$\frac{r}{r_s} = \frac{2v^*}{v_r} - (\frac{2v^*}{v_r} - 1)(1 + \frac{v_r t}{h_r})^{-1/2} \tag{3.7}$$

when $\frac{v_r}{2v^*} > 1$

From the high-speed video images (Figs. 3-5B, C), an effective contact line radius is extracted and compared to the model (Fig. 3-5D). Using v^* and h_r as fitting parameters in Eq. 3.7, model retraction curves are matched to measured time traces. In Fig. 3-5E, we show the measured average recession speed of the contact line for different stamp retraction speeds, compared with the above model. The model curves follow the general retraction behavior but deviate from the experimental results in a few important ways. Once the contact line begins to recede, the measurements show an initially slow but accelerating motion not captured by the model (Fig. 3-5D). Whereas the model assumes a symmetric, radial ink recession, images of the ink contact during retraction reveal a more irregular shape contributing to modeling inaccuracy. Further, the model does not account for the dynamics of transition of a pinned contact line into a receding one. The images in Fig. 3-5B, C suggest the possibility that the contact line initially remains pinned over some sections of the edge while receding from others, accentuating the asymmetry and resulting in a slower increase of the contact line speed as the gap increases. In the experiments, the contact line location is determined by viewing the ink through the transparent substrate. A certain thickness of ink will be required to obtain sufficient contrast to discern the contact line position. This leads to measurement uncertainty in the retraction time traces, and is greatest at the highest speed of 50 mm/s in the present experiments.

3.4.5   Rupture $(r = r_b)$

The geometry of the receding liquid bridge, and the dynamics of bridge rupture, determine the liquid volume that is printed. The receding liquid bridge ruptures
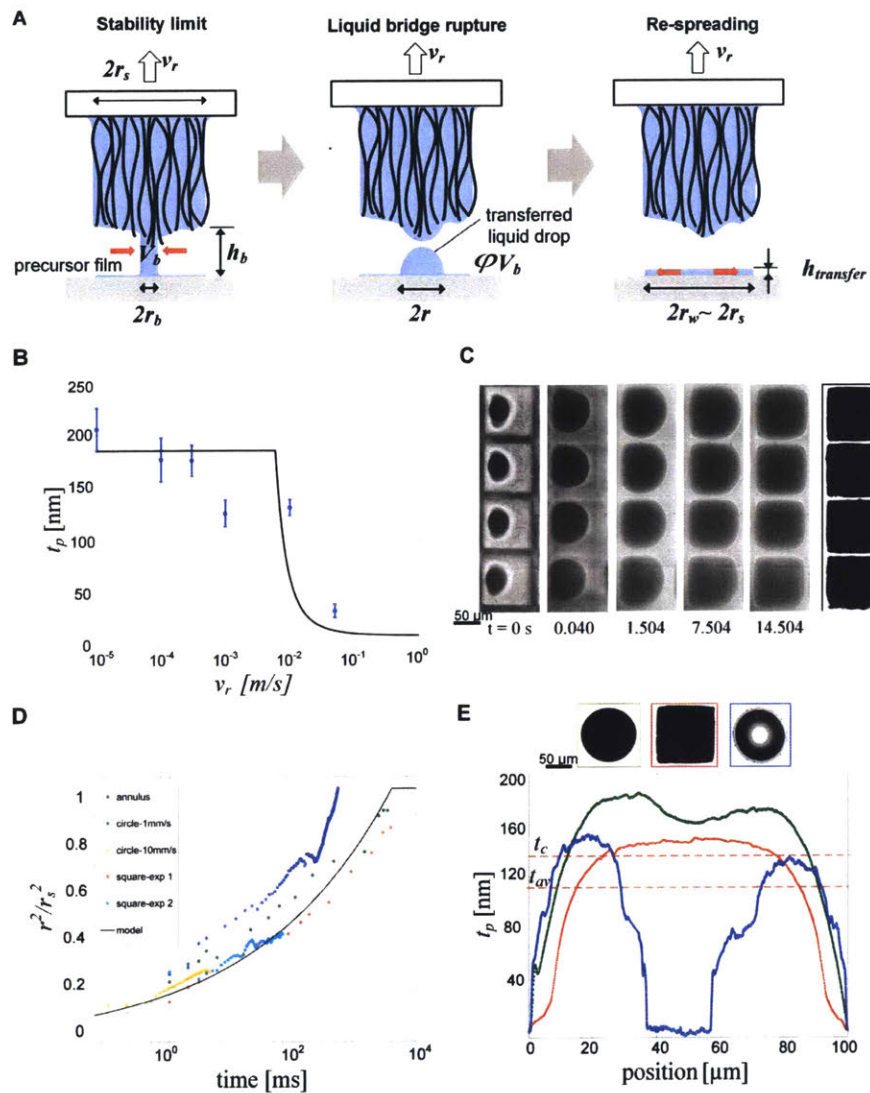
Figure 3-6: Transferred liquid film after bridge rupture and re-spreading. (A) Schematic of the liquid bridge at the moment of rupture, transferred liquid drop on the substrate after bridge rupture, and of transferred liquid drop re-spreading on the substrate to the stamp feature shape. (B) Thickness of printed solid layer after solvent evaporation versus retraction speed and comparison with model (solid line) (C) Snapshots from high speed videos of re-spreading of transferred drops forming films with the shape of four squares matching the stamp pattern closely. (D) Ratio of re-spread film area to stamp area versus time for three shapes and comparison with model in Eq. 3.7 (solid line). (E) Measured profile of printed solid layer for three shapes along with microscope images of the printed patterns.

49

(Fig. 3-6A) when the aspect ratio of the stretched meniscus exceeds its stability limit. For low capillary numbers ($Ca = \mu v_r/\gamma$), a liquid bridge with pinned contact lines stretched quasi-statically will become unstable at an aspect ratio of $h_b/r_b = 2\pi$ (r_b and h_b are the bridge radius and height at the instant of rupture), and breaks by visco-capillary necking. [53] The lowest point in Fig. 3-5D corresponds to the instant at which the capillary bridge breaks. By analyzing the videos, we find that the radius and height at the moment of rupture reasonably agree with the quasi-static stability limit. Assuming this limit defines the moment of rupture for all retraction speeds (Ca=0.00027-0.14), the radius, height, and volume ($V_b{\sim}\pi r_b^2 h_b$) of the liquid bridge at the moment of rupture can be estimated by approximating the liquid bridge geometry to be a cylinder. The retraction profiles in Fig. 3-5D show noticeable discrepancies in the radius of rupture between the model and the measurements. The model approximates the liquid bridge as a cylinder, but the actual liquid bridge deviates from this shape, both due to the non-circular cross-section observed in Fig. 3-5C and the off-perpendicular contact angle it makes with the substrate. Images of the liquid bridge just after rupture (Figs. 3-3B-D) show an off-center breaking position, indicating significant asymmetry in ink recession. Nevertheless, we accurately predict that the volume of ink in the capillary bridge at rupture decreases with retraction speed because at higher speeds, there is less time for ink to flow into the gap before rupture. At high speeds ($v_r \gg v^*$), ink transfer from within the stamp is negligible and the volume at rupture plateaus to the ink volume in the gap just before contact line recession began. The model predicts that the printed volume levels off to within 10% of the high-speed limit at v_r=0.2 m/s and is within 2% at v_r=1 m/s. At the limit of low speeds ($v_r \leq 2v^*$), we expect that the gap remains filled until rupture occurs. Therefore, the upper-bound for the ink transfer volume is determined by the stability limit of a liquid bridge pinned along the periphery of the stamp feature, $V_b = 2\pi^2 r_s^3$. Moreover, the symmetry of breakage is known to strongly depend on the differences in contact angles. [46] The transferred liquid volume can simply be estimated as ϕV_b, where ϕ is the transfer ratio. Assuming subsequent drying of the ink to a uniform layer of nanoparticles, for a 50% by weight colloidal ink, we estimate the printed layer

50

thickness (Fig. 3-6B) as $t_p = \phi V_b \rho_{Ag}(A\rho_{sol})$, where ρ_{Ag}, ρ_{sol} are the densities of silver and solvent and A is the area of the printed layer $(= \pi r_s^2)$. Therefore, the predicted printed layer thickness is constant for $v_r \leq 2v^*$ and then it decreases with retraction speed to level off to a constant value at high speeds $(v_r \gg v^*)$. We measured the profiles (Fig. 3-2E) of 5-10 samples of printed patterns on the spherical lens along a line and calculated the average thickness of each printed pattern. The measured values of average thickness (Fig. 3-6B) of the printed layers is higher than 200 nm at low retraction speeds $(v_r < 1$ mm/s), then it decreases to less than 50 nm at v_r=50 mm/s. The initial ink volume on the stamp varies between experiments conducted at different speeds and this leads to differences between the measured and predicted values of printed layer thickness.

3.4.6 Respreading $(r_b < r < r_s)$

Importantly, the liquid respreads to match the stamp feature after rupture (Videos S4a-c, S5a, 5b), and therefore the nanoporous stamps can be used to produce features with internal holes (e.g., annuli) and sharp corners (Figs. 3-6A, C) with high fidelity. We attribute this respreading to the presence of a precursor film, [54] a thin layer of liquid that forms on the wetted areas of the substrate during contact and remains after the stamp retracts. We expect this precursor film to be present even when printing with solid stamps, however, in that case, excess ink is squeezed out of the gap between the stamp and the substrate during printing, wetting a larger area than the original stamp feature. In contrast, nanoporous stamps make conformal contact with the substrate without significant squeeze out, creating a precursor film that matches the stamp area with high accuracy. The experimental time traces of respreading (Fig. 3-6D) show a relaxation of the ink radius without oscillation, verifying that inertial effects are negligible. Droplet spreading of this type is governed by Tanners Law, [54, 55]

$$\frac{r}{r_s} \propto \left(\frac{\gamma}{\mu r_s}\right)^{1/10} \tag{3.8}$$

51

This scaling reasonably tracks the measured respreading time traces, as shown in Fig. 3-6D. Similar to the approach and retraction models, respreading is approximated as occurring symmetrically. However, as seen in Fig. 3-6C, the ink bridge can rupture in an off-center position with an asymmetric shape. Furthermore, the ink reaches some sections of the edge earlier than other sections. This leads to deviation from the model throughout much of the respreading process. The model assumes radial respreading with a circular contact shape, and therefore also does not resolve the slower respreading into the corners of the square feature at later times (Fig. 3-6D). Similarly, the model does not attempt to capture the significant circumferential component of respreading from the annular feature, leading to significant deviation in that case (Fig. 3-6D). As with the approach and retraction models, the ink is approximated as a simple fluid, but the presence of nanoparticles may further complicate the spreading dynamics especially for layers with thickness comparable to the particle size within the fluid.

3.4.7 Towards precision, high-speed printing using nanoporous stamps

Precise control of the printed layer thickness, thickness uniformity, and shape accuracy compared to the stamp features, is necessary for fabrication of devices whose performance is coupled to these parameters. Here, using nanoporous flexography, we print Ag nanoparticle films with average thicknesses ranging from <30 nm to >150 nm, at retraction speeds of 0.1-50 mm/s. Therefore, we conclude that, keeping all other variables constant including the ink concentration and the surface properties, the retraction speed of the stamp is the principle means of controlling layer thickness. Previously, we demonstrated printing at linear speeds of up to 0.2 m/s using a plate-to-roll apparatus, and this speed was limited by the operating range of the linear motion stage in our apparatus. [19, 20] In the roll-to-plate configuration, which mimics industrial equipment, the retraction speed (v_r) between the stamp and the

roller is

$$v_r = v_t\sqrt{(h_b/R) - (h_b/2R)^2} \tag{3.9}$$

where v_t and R are the tangential speed and the radius of the roller respectively. Using values for R=0.254 mm and v_t=10 m/s typical in industrial flexography, we estimate the retraction speed to be 0.2 m/s which is in the asymptotic regime (t < 50 nm, FiG. 3-6B) using the conditions of our present experiments. From this point, the printed layer thickness (after drying) may be controlled by the particle concentration in the ink. The average thicknesses values calculated from the measured profiles (Fig. 3-6E) of the printed layers of circle, square and annulus are 146.6, 112.8, and 101.9 nm respectively. Though the thickness tapers sharply toward the edges of each printed shape, the printed features are locally very smooth, and uniform within the edge regions. The calculated average roughness (R_a) ranges from 1.5 to 5 nm, and the RMS roughness (R_q) ranges from 2 to 7 nm. These values are at least 10-fold less compared to layers printed using conventional flexographic printing with solid elastomer stamps. [12, 56] Returning to the overall distribution of printed features on the lens (Fig. 3-2E), we find that the measured thickness of the printed layers is not influenced by the contact pressure (Fig. 3-2H). This suggests that ink released from the stamp due to compression of the CNTs during contact is not affecting the printed volume. It is possible that any additional ink volume released during compression is quickly reabsorbed during decompression. This is also very desirable for industrial printing, because local and global variations in the stamp and substrate surface can be accommodated by compliance of the stamp, without detriment to printing uniformity. The lateral error, defined as the difference between the lateral dimension of the printed layer and that of the stamp pattern, is another major consideration for precision printing. The lateral dimension of the transferred film is determined at the moment of full wetting, as we found that the ruptured ink droplet tends to re-spread to fill the previously wetted shape. To achieve conformal contact between the stamp and substrate, the contact pressure between the stamp and substrate must lie within a range determined by the stiffness of the CNTs, CNT-CNT spacing (λ_{CNT}), and the

53

standard deviation (σ_l) of the lengths of CNTs, assuming the lengths are normally distributed. [20] Fig. 3-2G shows the pressure range (Δp_c) where the area ratio (ratio of area of stamp pattern to printed pattern) is 1 using the measurements of printed patterns on the spherical lens and comparison with the predictive model. [20] At the moment of full wetting, if the contact pressure is within this range, then during respreading, the transferred liquid drop fills the wetted area that matches the stamp pattern. If the pressure is less than the lower limit of this range, the printed area will be less than the stamp area due to partial or incomplete contact between the stamp and substrate. When the pressure is greater than the upper limit of this range, the area ratio is greater than 1 due to excessive deformation of the nanoporous stamp. Moreover, the vertical motion precision required to maintain the contact pressure range that was experimentally determined to achieve full contact without overprinting is $2\lambda_{CNT}^2\Delta p_c/k_{cnt}$, where $kcnt$ is the stiffness of the CNT. Therefore, the motion precision required is $\sim$150 nm to minimize lateral error in printing.

3.4.8 Limitations of this study

Our liquid transfer model elucidates other key factors that determine the transfer behavior and resulting dimensions of the transferred film, such as liquid surface tension and viscosity, stamp permeability, and initial ink load on the stamps. Further insights can be gained by studying the effect of the stamp porosity by varying the coating thickness of polymer on the CNTs or the CNT diameter or by varying both. However, varying the porosity by these methods will change the stiffness of the stamp and hence will alter the stamp-substrate contact mechanics. Experimental validation using inks with a wide range of liquid properties and stamps with controlled pore sizes will be beneficial for further understanding. Also, colloidal nanoparticle inks exhibit shear thinning rheology dependent on particle concentration. [57–67] This non-Newtonian behavior remains small for particle volume fractions below 25%, [60] making a Newtonian flow approximation reasonable for the 7% volume fraction ink used in this study. However, printing with inks at higher loading, and/or printing of much smaller features may require consideration of non-Newtonian behavior. The

influence of stamp compression on the ink flow within the gap, and the dynamics of retraction, must be considered for features whose dimensions approach the motion and alignment precision of the printing apparatus, or when stamp compression is relied upon to accommodate substrate curvature or roughness. Further, the present model approximates the ink volume in the gap as being cylindrical and groups a number of factors including capillary pressure within the stamp, contact angles, and ink loading into a fitting parameter, ΔP, without attempting to find a relation for this parameter based on the physical system. Nevertheless, our analysis captures the key dependencies of transferred ink volume on retraction speed, and of spreading time on approach speed.

3.5   Experimental setup

In the case of a planar stamp making contact with the spherical lens, the contact pressure can be controlled by the force, geometry, and mechanical properties of the materials in contact. Assuming Hertzian contact between the spherical lens and stamp, we estimated that, with a glass lens of 500 mm radius, we can achieve an average contact pressure of 33 kPa with an applied force of 100 mN. Accordingly, we designed a flexure made of aluminum (bending stiffness = 240 N/m) to apply this required force. The CNT stamp is placed on the flexure and brought into contact with the lens. By making the flexure much more compliant than CNT stamps (stiffness = 10-100 kN/m), the contact force between the stamp and the lens can solely be determined by the flexure stiffness and deflection. That is, for a known flexure stiffness, we can control the flexure deflection and hence the contact force and pressure. For example, a deflection of 10 microns will correspond to the minimum force of 2 mN. The flexure is clamped at its ends and a capacitance probe (Lion Precision, C8-2.0-2.0) placed between the flexure holder and the flexure is used to measure the deflection. The flexure holder is attached to a single axis motion stage (Aerotech, ANT130L) via a tip-tilt stage (Thor Labs, PY 003). The microscope consists of a collimated light source (AmScope, LED-11WYR), pellicle beam splitter (Thor Labs,

CM1-BP145B1), infinity corrected 5x objective lens (Mitutoyo, M Plan Apo 5X) and a tube lens (focal length = 250mm) to achieve 25x magnification so that we can capture images with a resolution of 1.1 microns. The light source arrangement allows for illumination even when the stamp is in contact with the substrate, enabling video capture at high frame rates of 25000 fps. The infinity corrected objective provides a working distance of 20 mm to accommodate the fixture and work space required to mount and unmount lenses before and after each printing cycle. The high speed camera (Vision Research, Phantom v2511) was placed on a custom-built motion system with three degrees of freedom to adjust the focus and field of view while taking videos during the experiments.

3.6 Calculation of radius and height at the moment of rupture

The base radius of the liquid bridge is directly obtained from the image at the instant of bridge rupture. The deflection sensor records the force between the stamp and the substrate. The deflection sensor readings are used to record the time (t_1) at which the stamp loses contact with the substrate. The high speed videos have time stamps associated with each frame. Using the time stamps on the high speed videos, we record the time (t_2) at which the bridge rupture occurs. The height of the liquid bridge at rupture is given by $v_r(t_2 - t_1)$ where v_r is the retraction speed of the motion stage.

3.7 The transfer ratio

The differences in material and structure between the stamp and substrate likely mean differences in contact angles, and hence, a value for the transfer ratio (ϕ) different from 0.5. No value of the transfer ratio is assumed in the text. It is included in the fitting parameter used to match experimental data in Fig. 3-6B.

Symbol	Description
γ	Surface tension of the liquid ink
ΔP	Pressure difference from deep in the porous stamp to the surface of ink meniscus in the gap between the stamp and the substrate
Δp_c	The contact pressure range in which the printed area ratio is $\tilde{1}$
κ_{rr}	Radial permeability of the porous stamp
κ_{zz}	Axial permeability of the porous stamp
μ	Viscosity of the liquid ink
σ	Root mean square (R.M.S.) roughness of the wetted stamp surface
ϕ	Transfer ratio
h	Height of the liquid bridge (modeled as a cylinder) during approach
h_b	Height of the (cylindrical) liquid bridge at the moment of rupture
h_r	The gap distance at the which the ink contact line on the substrate begins to recede
h_a	Distance between the bottom of the stamp surface and substrate at the moment of wetting initiation
$h_{transfer}$	Thickness of the liquid layer at the end of respreading
k_{CNT}	Stiffness of CNT
$p_{t,min}$	Minimum contact pressure at which the printed area ratio is ~ 1
$p_{t,max}$	Maximum contact pressure at which the printed area ratio is ~ 1
r	Radius of the liquid bridge (modeled as a cylinder) during approach
r_b	Radius of the (cylindrical) liquid bridge at the moment of rupture
r_i	Average radius of the base of liquid bridge on the substrate at the moment of wetting initiation
r_s	Radius of the circular stamp
r_w	Radius of the fully wetted contact area
R_a	Average roughness of the printed layer
R_q	RMS roughness of the printed layer
V_b	Volume of the liquid bridge at the moment of rupture
v^*	Critical velocity
v_a	Stamp approach speed
v_r	Stamp retraction speed
v_s	Average spreading speed
t_p	Thickness of the printed solid layer after drying
t_c	Reference thickness used for calculating roughness of the central region of the printed layer
t_{av}	Average thickness of the printed layer

Table 3.1: List of Symbols

3.8 Contact angle measurement

The contact angle of the silver nanoparticle ink on the lens was measured to be 8.84^0 using a rame-hart contact angle goniometer. The contact angle hysteresis is negligible and is less than the measurement error of 1%.

3.9 Roughness of printed layer

The steps used to calculate the roughness of the printed layer are

1. From the measured thickness profile, select the a region by setting a reference thickness,t_{ref}. All the values $> t_{ref}$ are used to calculate the roughness of the printed layer. We used two different reference values

    (a) Central region ($t_{ref} = t_c$) : For example, in Fig. 3-6E, in the printed layer profile of square pattern, we choose the thickness values larger than 142 nm. This creates a sample subset of thickness values in the central region (27 μm < X position < 72 μm). The dotted line shows the reference thickness tc used for calculating the roughness for square.

    (b) Entire region ($t_{ref} = t_{av}$) : For example, in Fig. 3-6E, in the printed layer profile of square pattern, we choose the thickness values larger than 112 nm. The dotted line shows the reference thickness t_av used for calculating the roughness for square.

2. Calculate the mean (μ) of the thickness values from the sample of size N

3. Using the mean, calculate the average and RMS roughness using the following equations

$$R_a = \frac{\sum_i t_p(i) - \mu}{N} \tag{3.10}$$

$$R_q = \frac{\sqrt{\sum_i (t_p(i) - \mu)^2}}{N} \tag{3.11}$$

Printed Pattern Shape	Reference thickness, t_c(nm)	Sample mean, μ (nm)	Average roughness, R_a (nm)	RMS roughness, R_q (nm)
Square	142	146.54	1.59	1.97
Circle	160	171.38	5.89	7.07
Annulus Sample 1	140	147.04	3.04	3.41
Annulus Sample 2	$120 < t_p < 138$	127.86	3.27	3.79

Table 3.2: Roughness values calculated for the central region of the printed layer

Printed Pattern Shape	Reference thickness, t_{av} (nm)	Average roughness, R_a (nm)	RMS roughness, R_q (nm)
Square	112.8	39.2	48.4
Circle	146.6	33.6	44
Annulus	101.9	32.8	38.4

Table 3.3: Roughness values calculated for the entire printed layer

The tables below show the values of chosen reference thickness and computed mean, average and RMS roughness of the profiles of printed patterns of three shapes.

3.10 Conclusions

We have studied the dynamics of ink transfer from nanoporous stamps enabling precision printing of ultra-thin liquid films by displacement-controlled mechanical contact. Using high-speed imaging and analytical modeling, we have shown that, at low stamp approach speeds, liquid spreading is driven by capillary forces and flow from the nanoporous stamp, while at high approach speeds, liquid spreading is driven by the stamp compression rate during contact. The same model was applied to retraction to show how the flow within the stamp influences the volume of liquid transferred at different stamp speeds. Further, we show how the respreading of liquid over a precursor film, matching the maximal stamp-substrate contact area, enables direct printing of non-circular features. These findings have implications for applying nanoporous print-

ing stamps in industrial scale roll-to-roll printing of electronics devices. Yet , further work is required on registration and materials compatibility in multilayer printing, surface treatment to optimize wettabilities, and sintering of printed nanoparticles to form continuous layers with desired electrical properties.

Chapter 4

A desktop plate to roll apparatus for development of flexographic printing processes

The contents of this chapter is expanded from a conference paper [68] - Plate to roll apparatus for flexography using nanoporous stamps.

4.1 Abstract

Flexographic printing is widely used for high-throughput manufacturing of printed electronics including displays, RFID tags, solar photovoltaics, and sensors. Print quality measured by the feature resolution and layer thickness affects the performance of the printed devices; resolution and layer thickness depend on precise control of flexographic printing parameters including stamp-substrate contact pressure, stamp ink volume, print speed and surface wettabilities. We present the design and fabrication of a desktop printing apparatus to conduct flexographic printing experiments and gain a physics based understanding of the relationship between printing process parameters and print quality. In a prior work, printing of ultra-thin($\sim$100nm), high-resolution ($\sim$3μm) features at high speeds (>0.1m/s) was achieved with nanoporous stamps comprising of polymer coated vertically aligned carbon nanotubes (VACNTs). The

machine includes a flexure, a Z motion stage and a capacitance probe to set a desired contact force and low run-out ($<5\mu$m) roller to minimize the stamp-substrate contact force variation. Strain-gages on the flexure beams are used to achieve alignment along the roller-stamp contact line. Furthermore, independently driven rotary and linear motors are synchronized to eliminate shear at the stamp-substrate interface and achieve slip-free smooth motion while printing at low and high speeds. We use this printing apparatus and show printing of high resolution features with nanoporous printing stamps across a range of speeds. The machine can be used to conduct experiments to understand the physics of flexographic printing processes and prototype devices such as TFTs.
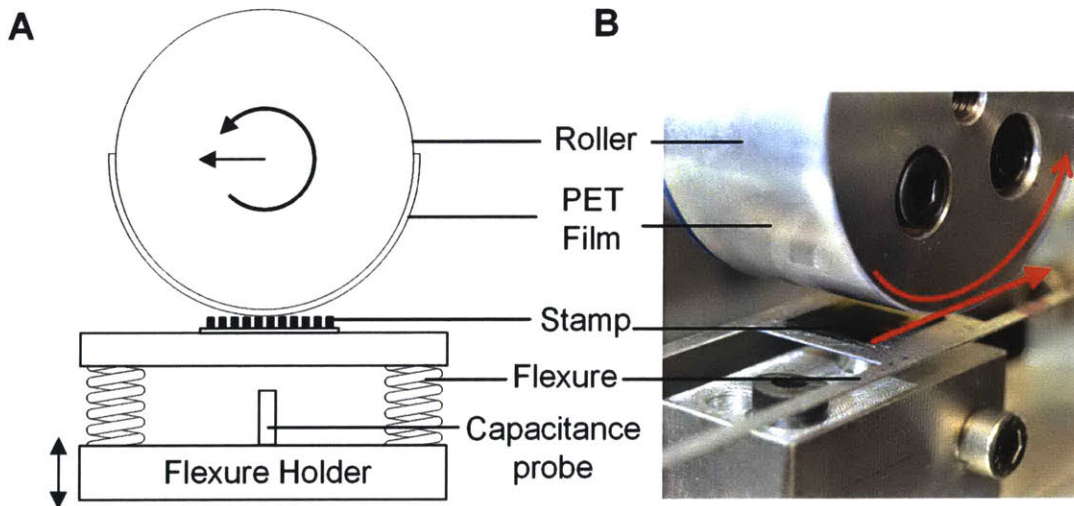

Figure 4-1: A desktop plate to roll apparatus with slip-free smooth rotary and translation motions, adjustable contact force and alignment control for high-resolution printing applications A) Schematic and B) Photograph of the machine showing the printing stamp, flexible substrate, flexure used for setting the contact force, displacement sensor and the roller.

4.2 Introduction

Flexographic printing is a manufacturing process used to print patterns on rigid or flexible substrates by transferring liquid from a patterned elastomer stamp [13]. Flexography is a highly scalable printing method and can be used to print continuously at high speeds on large substrate areas. From printing graphics, flexography has been adapted to print devices such as transistors, solar cells, RFID tags, and transparent electrodes [69–72]. The flexographic printing parameters including print speed, ink volume, and printing force determine the print quality measured in terms of print resolution and layer thickness [12, 73]. These dimensions influence the performance and design limits of underlying elements such as thin-film transistors [24, 74, 75]. An understanding of the process physics and determination of the optimal printing conditions is essential to achieve a desired print quality[3]. To perform such studies, we need a desktop printing apparatus in which experiments can be conducted by varying the printing parameters. The printing apparatus can be used to conduct printing experiments and study the effect of process parameters on print quality by characterizing the printed samples. Here, we report the design and evaluation of a benchtop plate-to-roll (P2R) machine (Fig. 4-1) for flexographic printing. Mainstream printing technologies including inkjet, screen, gravure (intaglio), as well as flexographic (relief) printing are limited to feature sizes no smaller than tens of microns [39, 76]. In flexography, while rubber stamps with sub-micron feature resolution can be manufactured, challenges arise in loading these stamps with thin layers of ink and controlling the quantity of ink transferred to substrates [12, 13, 39]. In flexographic printing, we recently demonstrated that significantly finer printed feature dimensions can be achieved when nanoporous stamps are used instead of traditional non-porous polymer stamps [16]. The key difference is that nanoporous stamps retain the ink within their volume, enabling the printed pattern to precisely replicate the shape of stamp features without suffering the squeeze-out and dewetting instabilities of traditional flexography. For instance, nanoporous stamps comprising polymer-coated vertically aligned carbon nanotubes (CNTs) enabled high speed (0.1 m/s) printing of features

with 3 μm minimum size, from conductive, dielectric, and semiconducting nanoparticle inks [16].

4.3 Design of the plate to roll apparatus

The machine (Fig. 4-2) is designed to accomodate CNT stamps up to 20 x 20 mm in size, and controls the contact force, contact speed, and alignment between the stamp and the substrate across the contact line. During printing, the CNT stamp is placed on the flexure stage, and the printing substrate (e.g., a polyethylene terephthalate film) is wrapped around the circumference of the roller forcing the roller and stamp to form a line contact. Under nominal conditions, we seek to match the roller and substrate motion so there is no slip at the contact line, with a design target maximum speed of 350 mm/sec. The design of the four sub-systems of the P2R apparatus including the roller assembly, flexure assembly, contact alignment system, and the motion system are explained in the following sections.

4.3.1 Flexure assembly

Control of the force is critical to achieve high quality relief printing. In previous work, we showed that uniform ink transfer from a CNT microstructure to a solid substrate can be achieved only when the contact pressure ranges from 28-150 kPa [16]. This pressure range was derived based on modeling of contact mechanics of the nanoporous stamp and the substrate and manual plate-to-plate printing experiments. In the case of plate-to-roll contact, the contact pressure can be controlled by the force, geometry, and mechanical properties of the materials in contact. Assuming Hertzian contact between the roller and stamp, we estimated that, with an aluminum roller of 50mm diameter, we can achieve average contact pressure ranging from 15-167 kPa by controlling the applied force from 2-250 mN (Fig. 4-3). Accordingly, we designed a flexure made of aluminum (bending stiffness = 243.3 N/m) to apply this required force. The CNT stamp is placed on the flexure and brought into contact with the roller. By making the flexure atleast 50 times more compliant than CNT stamps

A

Roller Assembly
Motor Mounting Bracket
Bearing Housing
Roller

Stage Assembly
Z Actuator
Flexure
Z Motion Stage

Motion System
Roller Motor
Linear Motor

Z
Yaw
X
Y
Pitch

Pitch-Yaw (Tip-Tilt) Stage
Pitch Adjustment Micrometer
Yaw Adjustment Micrometer

Contact Alignment System

B

Z-actuator

Roller
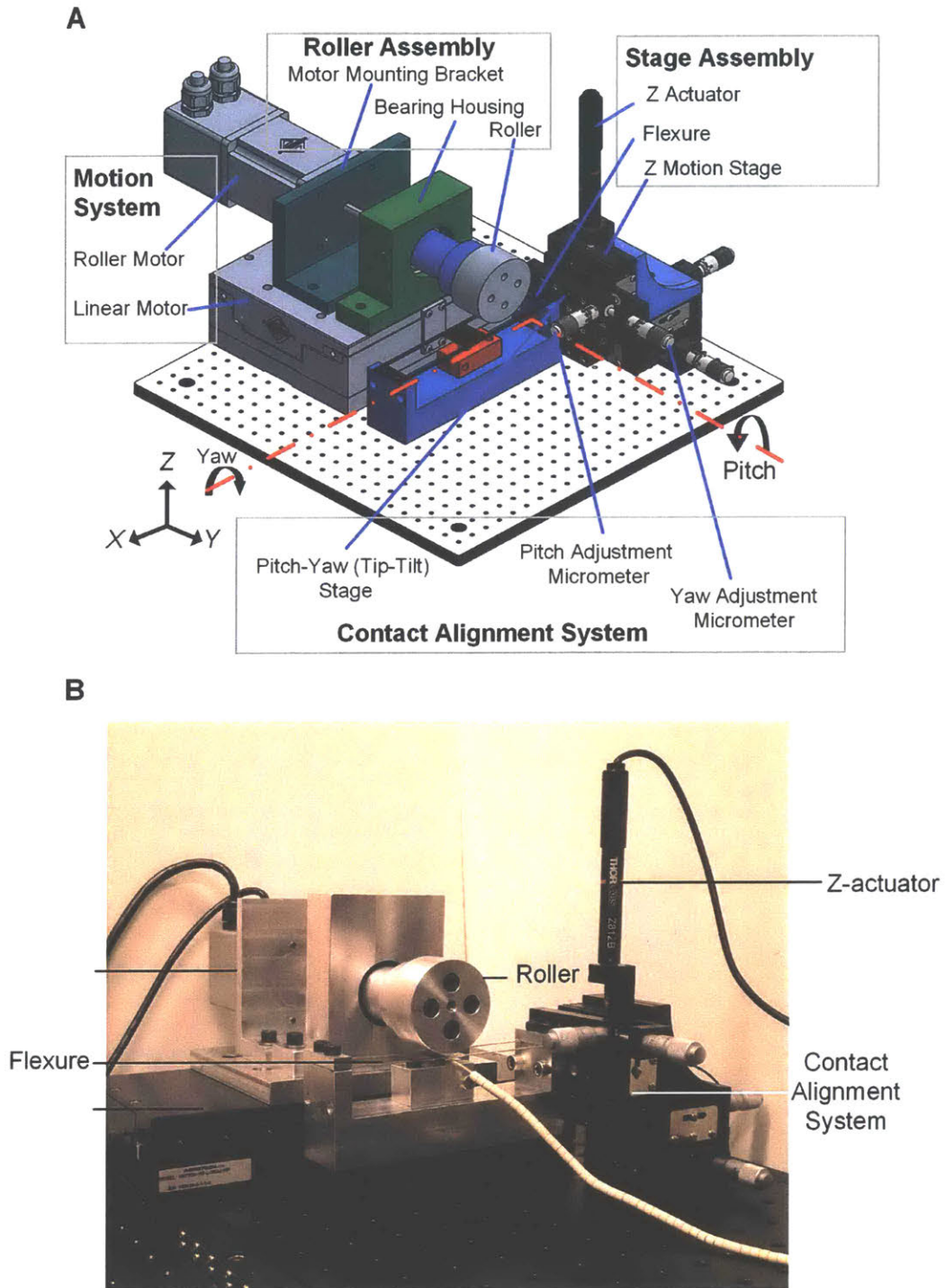
Flexure

Contact Alignment System

Figure 4-2: CAD model of the plate to roll machine A) Schematic and B) Photograph of the machine showing the four subsystems including roller assembly, stage assembly, motion and the contact alignment systems

(stiffness = 10-100 kN/m), the contact force between the plate and the roller can be determined solely by the flexure stiffness and deflection. That is, for a known flexure stiffness, we can control the flexure deflection and hence the contact force and pressure. For example, a deflection of 10 microns will correspond to the minimum force of 2 mN. The flexure is clamped at its ends. A capacitance probe (Lion Precision, C8-2.0-2.0) placed between the flexure holder and the flexure is used to measure the deflection (Fig. 4-3). The capacitance probe has a resolution of 2.1nm [77]. The flexure holder is attached to a single axis motion stage via a tip-tilt stage.

4.3.2   Roller assembly

We designed the roller assembly so that experiments can be performed with rollers of different diameters, lengths and materials. The assembly (Fig. 4-2) consists of the roller, shaft, angular contact bearings, and the bearing housing. The nominal design is an aluminum roller of 50 mm diameter. The roller is mounted at the end of a stepped shaft supported by two angular contact bearings (ABEC-7) assembled in a back-to-back configuration. By keeping the length of the shaft as small as possible and assembling the bearings in back-to-back configuration, we achieve a high moment stiffness and reduce shaft deflections due to dynamic loads. Surface grinding (Fig. 4-4) was performed on the roller after assembly, resulting in a total indicated run out of 5 m (Fig.. 4-4)

4.3.3   Contact alignment system

The roller and CNT stamp come into contact along a line. During the printing process, the roller rotates about its axis and translates in the X direction (Fig. 4-5). In order to achieve uniform ink transfer between the stamp and the substrate, the contact pressure must be maintained within 28-150 kPa. Moreover, the contact pressure must be uniform across the contact line. To adjust any misalignment between the plate and roller, we assembled a pitch-yaw stage (ThorLabs, PY003, resolution = 109.1 arc seconds) on top of the Z motion stage (Fig. 4-5). Four strain gages attached to the
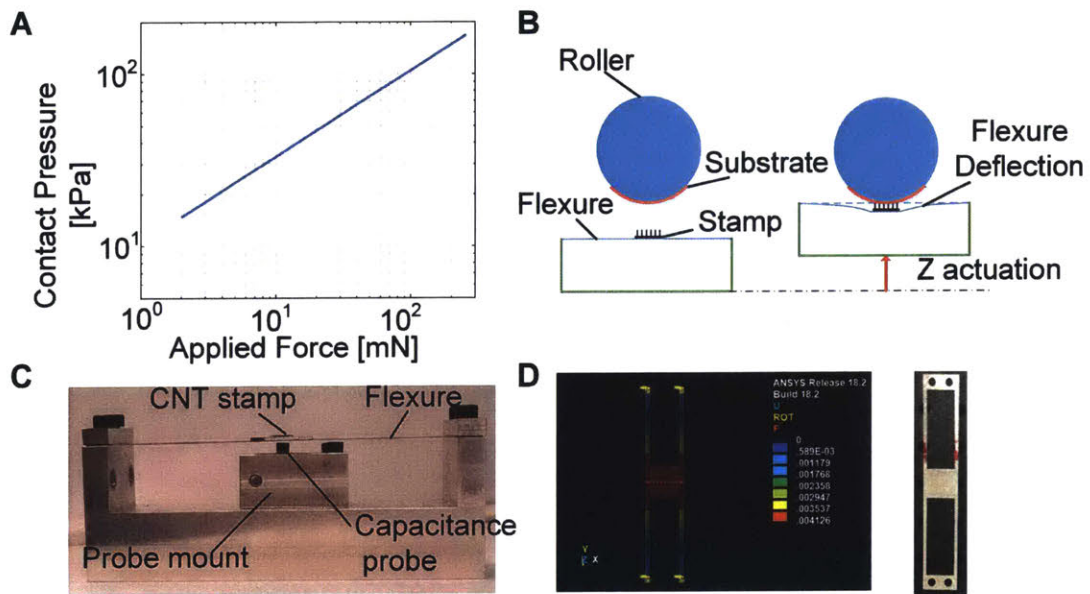
Figure 4-3: A Flexure, capacitance based displacement sensor and a micrometer stage are used to set the contact force between the plate and the roller A)Relationship between the contact pressure and applied force based on the cylinder-plane Hertzian contact mechanics modeling B)Schematic and C) photograph showing the method of application of contact force via a flexure, displacement sensor and Z motion of a rigid flexure holder D) Resultant displacement of the flexure in response to the force applied along a contact line calculated using finite element analysis (Applied force = 1N, Maximum displacement = 4.1mm, Calculated stiffness in Z direction = 243 N/m)

A
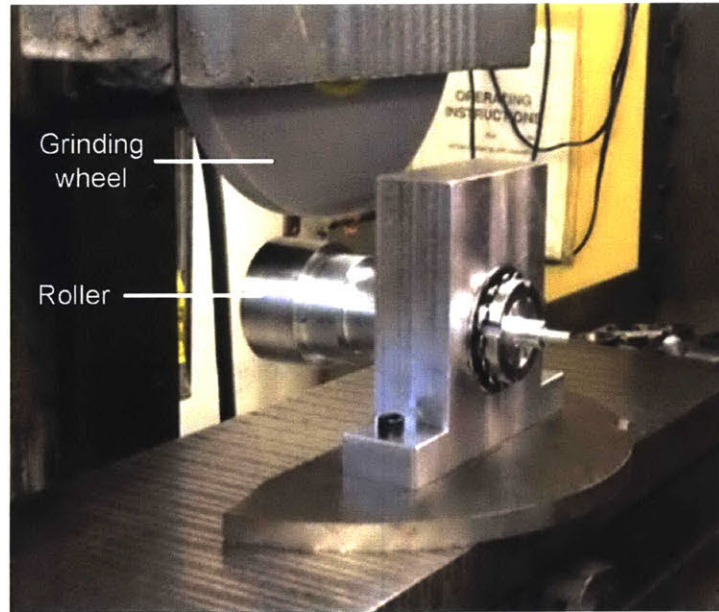
B
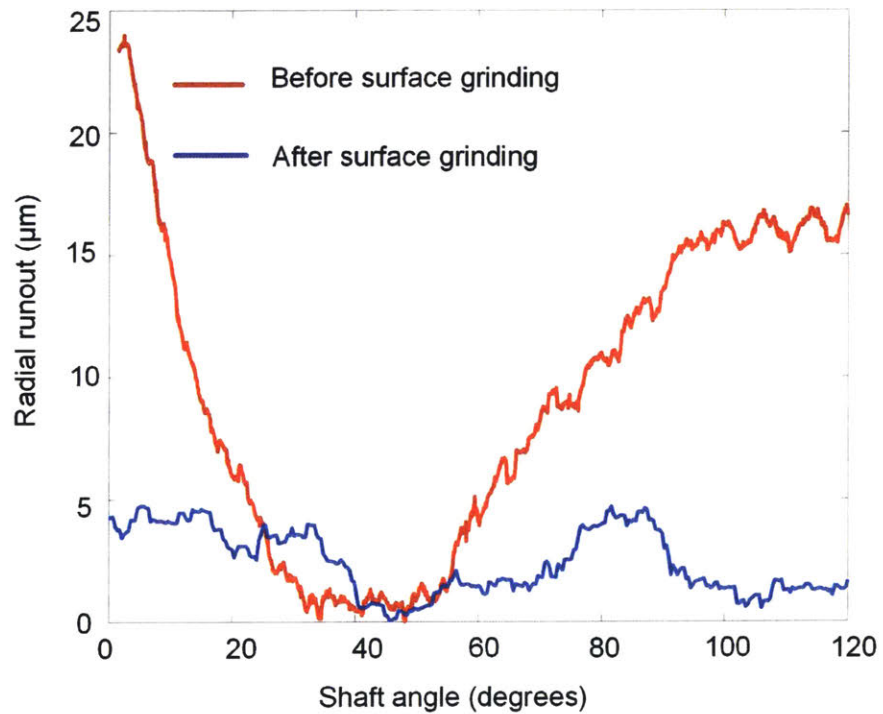
Figure 4-4: Surface grinding of the roller A) Photograph shows the surface grinding wheel and the roller as part of the roller assembly after surface grinding B) Radial runout measurements of the shaft showthe reduction in radial runout after surface grinding to less than 5 microns keeping the force variations during printing to within 1.2mN

beams of the flexure stage measure the deflections of the beams and S1,S2,S3 and S4 are the strains measured by the gages. The yaw adjustment micrometer is used to control the alignment ($\phi=0$) along the contact line aligned with the Y axis (Fig. 4-5). The pitch adjustment micrometer is used to control the alignment and maintain the condition $\phi=0$ as the contact line moves in the X direction during printing and as becomes either positive or negative. As shown in Fig. 4-5, at the starting position, S_1 equals S_2 and is greater than S_3 which equals S_4. During printing and when the roller is in the middle of the flexure stage, all strains are equal. At the stopping position, S_3 equals S_4 and is greater than S_1 which equals S_2. These conditions are set by adjusting the yaw and pitch micrometer stages using the strain values.

4.3.4 Motion system

While the roller rotates about its axis and translates, there should be no slip at the roller-stamp interface. This condition can easily be achieved in two ways: (1) driving the rotor about the rotary axis (ω) and letting the interfacial friction provide the linear motion (V); or (2) driving the stamp or the roller along the linear axis (V) and letting the friction provide the rotary motion (ω). However, the CNT stamps cannot endure the shear stress induced by the friction due to their own mechanics and the limited adhesion between CNT microstructures and their base substrate. To overcome this limitation, we designed the motion system with independent drives for the roller rotation and translation. The challenge in the design and implementation of such a system is achieving exactly synchronized motion between the rotation and translation so that $R\omega = V$. To provide rotary motion for the roller, a slotless, brushless DC motor (Aerotech, BMS60) is used[16]. The motor has a built-in rotary encoder, and the positon resolution of the roller along the circumference is 39 nm and can provide smooth motion at low and high speeds. A linear motor (Aerotech, ANT 130L) with 160 mm travel range, 1 nm resolution, and 350 mm/sec speed limit provides the translation for the roller [78]. With the BLDC motor and direct drive linear motor, velocity control can be implemented to eliminate slip and achieve smooth motion at low and high speeds.
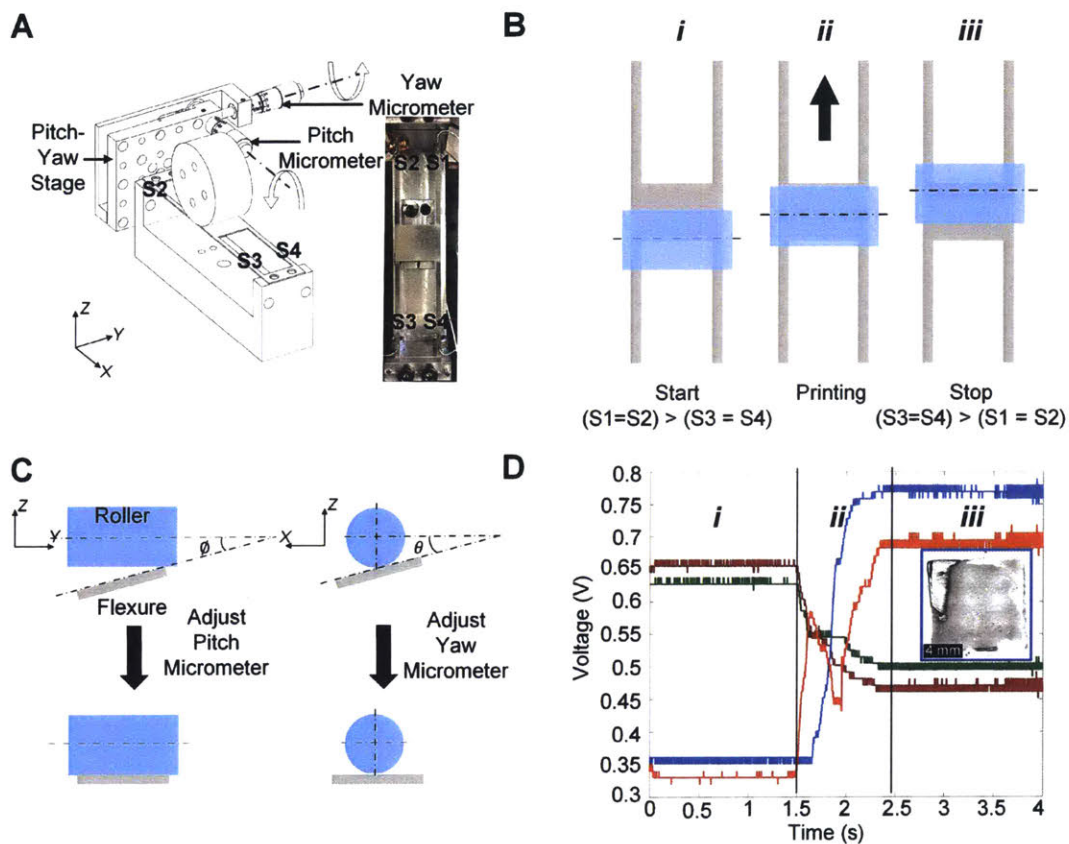
Figure 4-5: Pitch-Yaw micrometer stages and four strain gages attached to the beams in the flexure stages are used to align the roller and plate during printing A) CAD model showing the pitch yaw stage, micrometers, roller, flexure holder, flexure and the locations of the strain gages S1, S2, S3, and S4. B) Schematics showing the position of the roller and the contact line at the start and stop of printing and during printing. C)Schematics showing the misaligned aligned positions of the flexure and roller about the pitch and yaw axes. D)Values of the strain gages S1, S2, S3 and S4 at the start and stop of printing and during printing in terms of the amplified voltages when there is no misalignment between the flexure and roller about the pitch and yaw axes (inset shows the printed pattern when the roller and stamp are aligned about the pitch and yaw axes)
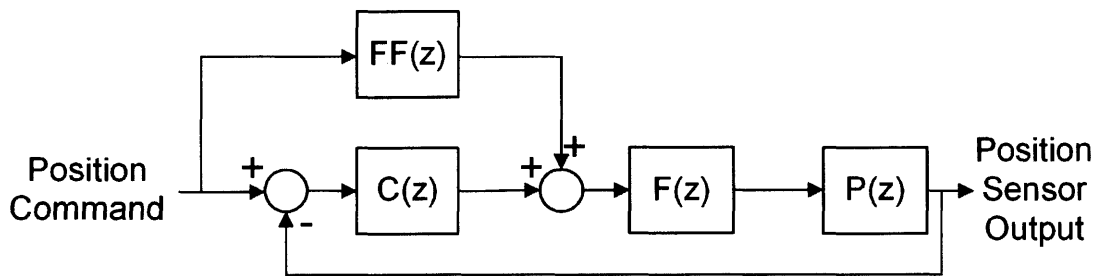
Figure 4-6: Roller and linear motion stages use tuned feedforward and PID controllers to achieve smooth motion (P(z) , C(z), FF(z), and F(z) are the transfer functions of the plant, PID controller feedforward controller, and servofilters respectively)

71

4.3.5 Control system

Fig. 4-6 shows the block diagram of the closed-loop system. The transfer functions of the plant and controller are $P(z)$ and $C(z)$ respectively. The plant consists of the dynamic system driven by the BMS 60 motor for the rotary motion and the one driven by the ANT130L motor for the linear motion. The transfer functions of the filter and feedforward controller are $F(z)$ and $FF(z)$ respectively. The closed loop transfer function is given by

$$\frac{Y}{X} = \frac{FF(z)F(z)P(z) + C(z)F(z)P(z)}{1 + C(z)F(z)P(z)} \tag{4.1}$$

Fig. 4-7 shows the measured open loop and closed transfer functions of the rotary and linear motors. The closed loop transfer functions show that the magnitude is 1 for the frequency range of 0-100Hz. The magnitude and phase show that the closed loop rotary and linear motion systems have significant phase and gain margins. These high margins render the rotary and linear motion systems stable and able to track trajectories and hence eliminate slip between rotary and linear motions. See supporting information for the controller block diagram and its transfer function.

4.4 Plate-to-roll printing experiments

4.4.1 Experimental procedure

Nanoporous stamps are fabricated using the chemical vapor deposition (CVD) growth of CNT forests from a lithographically patterned catalyst film on a silicon wafer. [16] Fig. 4-8A shows SEM images of the nanoporous stamp with an array of cylindrical micropillars. The mechanical compliance, surface roughness, and wettability of the stamp structures are tailored via plasma treatment of the CNTs and subsequent coating with a thin layer of polymer (pPFDA, 20 nm) by initiated chemical vapor deposition (iCVD). [16,17,21] A 100 μl droplet of ink is pipetted onto the stamp and then the stamp is spun to 1500 rpm for 1-3 minutes in a spincoater. The wet stamp is
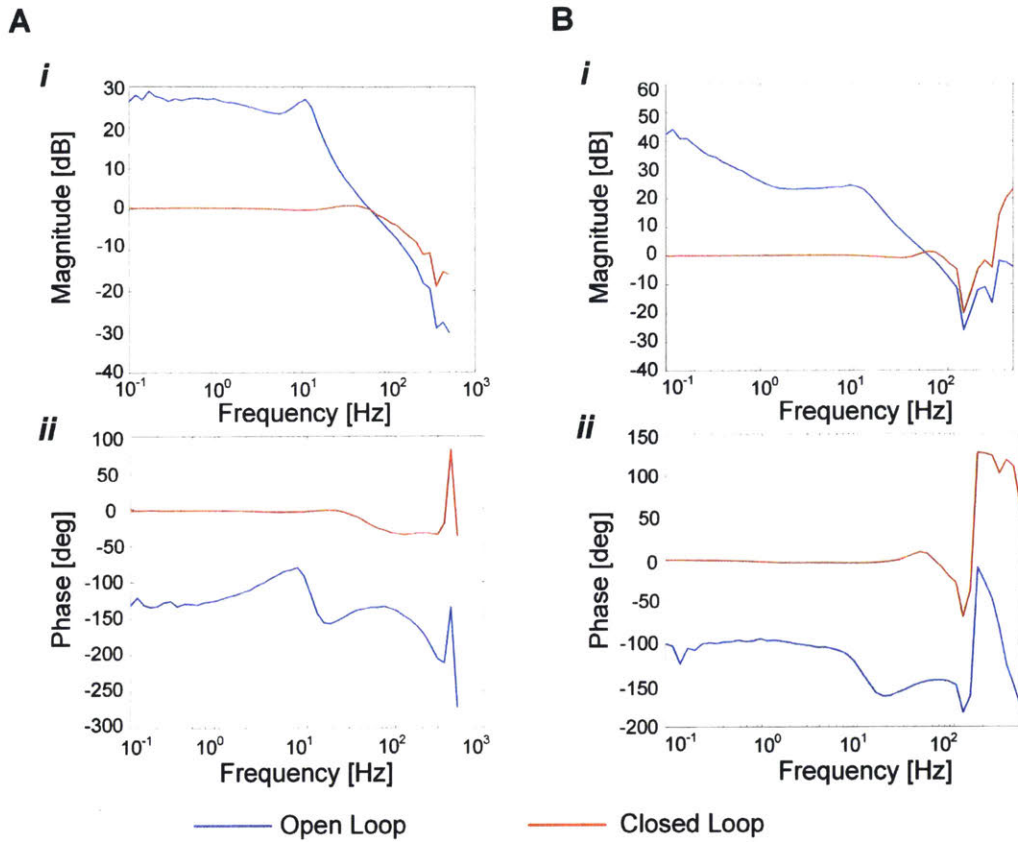
Figure 4-7: Frequency response measurements show a stable dynamic system with flat amplitude response for frequency up to 500 Hz and sufficient phase and gain margins as in the A) The closed loop frequency response of the roller and B) The linear motion stages.

brought into contact with another stamp consisting of CNT forests with no patterns in them, as described in our previous work. [16] After the removal of excess ink, ink wets the stamp surface conformally. We conducted the printing experiments using a five-step procedure. First, PET film is attached to the roller, and the printing stamp is placed on the flexure and brought into contact. Next, we determine the motion stage displacement at which the contact force lies within the range of 2-250 mN and align the stamp and substrate as explained in section 2.3. In the third step, we detach the stamp from the flexure, apply the ink on the stamp and remove the excess ink as outlined in section 3.1. Then, we attach the wet stamp to the flexure. Fig. 4-5 shows the start position of the roller and linear motion stage before printing. Last,

we command the motors to execute the printing step, schematically shown in Fig. 4-5
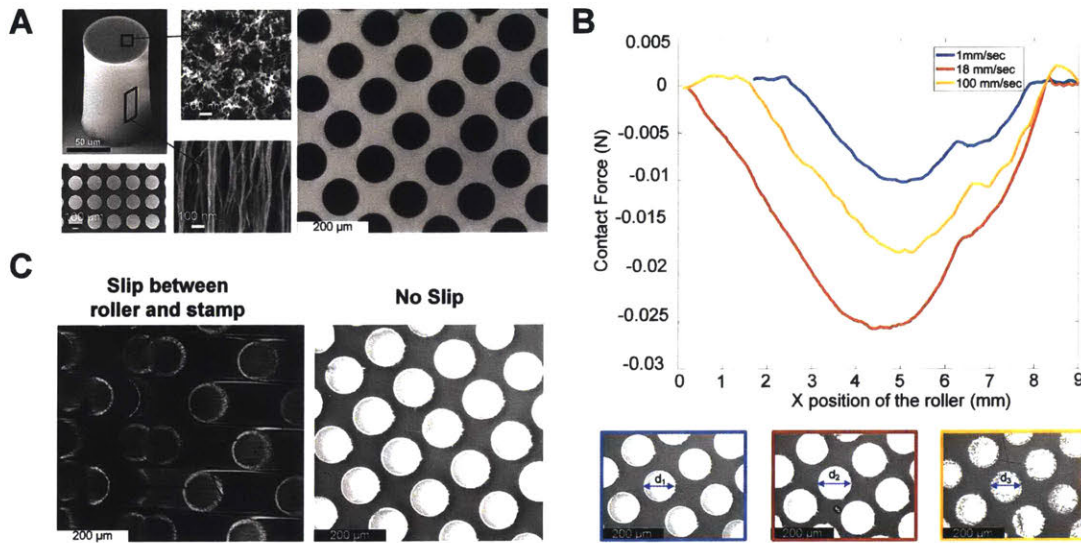
Figure 4-8: Nanoporous Printing Stamp, Printed Patterns and the Printing Force A) SEM image of the micropillar in the printing stamp, nanoscale pore shown on the top surface and the sidewalls of the micropillar and the optical image of the printing stamp B) Microscope image of printed patterns at low (1 mm/sec), intermediate (18 mm/sec) and high speeds (100 mm/sec) C) Printing force variation during printing at low, intermediate, and high speeds.

4.4.2 High resolution P2R printing by force control with no slip at various speeds

Fig. 4-8B shows the force measured during the printing process for three different translation speeds - 1, 18, and 100 mm/sec. The contact force is calculated from the measured deflection of the flexure. The capacitance probe measures the deflection

| Speed | Diameter | | Center to Center Distance | |
| (mm/sec) | (μm) | | (μm) | |
	Mean	Std. Dev.	Mean	Std. Dev.
1	100.34	1.62	130.48	0.58
18	105.53	2.37	131.44	0.46
100	99.79	1.88	131.27	1.12

Table 4.1: Analysis of printed patterns

of the flexure at the midpoint, whereas the contact line moves with the roller during printing. As the contact line moves, the deflection in the middle of the flexure increases to a maximum value and then decreases. This variation is shown in the measured printing force at all speeds. Though the measured printing force varies, it is force is >2 mN and <25 mN; these values are within the optimal range in which the contact pressure is sufficient for the stamp to make conformal contact with the substrate. Between printing experiments, PET samples were attached to and removed from the roller for experiments conducted at different speeds. The printing force vary with the printing speed due to variations introduced to the substrate surface profile in the way samples were attached. By applying the contact force required to achieve conformal contact between the stamp and substrate and eliminating the slip between roller and slip, we print patterns of different lateral dimensions (3-100 μm) across a range of speeds (1-100 mm/sec). Fig.4-8A-C show the optical microscope image of the stamp consisting of 100 μm diameter micropillars and the printed patterns on the PET substrates at low and high speeds. Fig. 4-9A and B show the microscope images of stamp with a honeycomb pattern with a line width of 3 microns and the printed pattern on flexible glass (SCHOTT, Thin Glass AF32) at 100 mm/sec respectively. The lateral error, defined as the difference between the lateral dimension of the printed layer and that of the stamp pattern, is a major consideration for precision printing. The mean and standard deviation of the diameters and center to center distances measured from the printed patterns (Fig. 4-8B) are summarized in Table. 4.1

The mean and standard deviation of the diameters and center to center distances measured from the stamp are 100±1.75μm and 131.3±0.47μm respectively. The
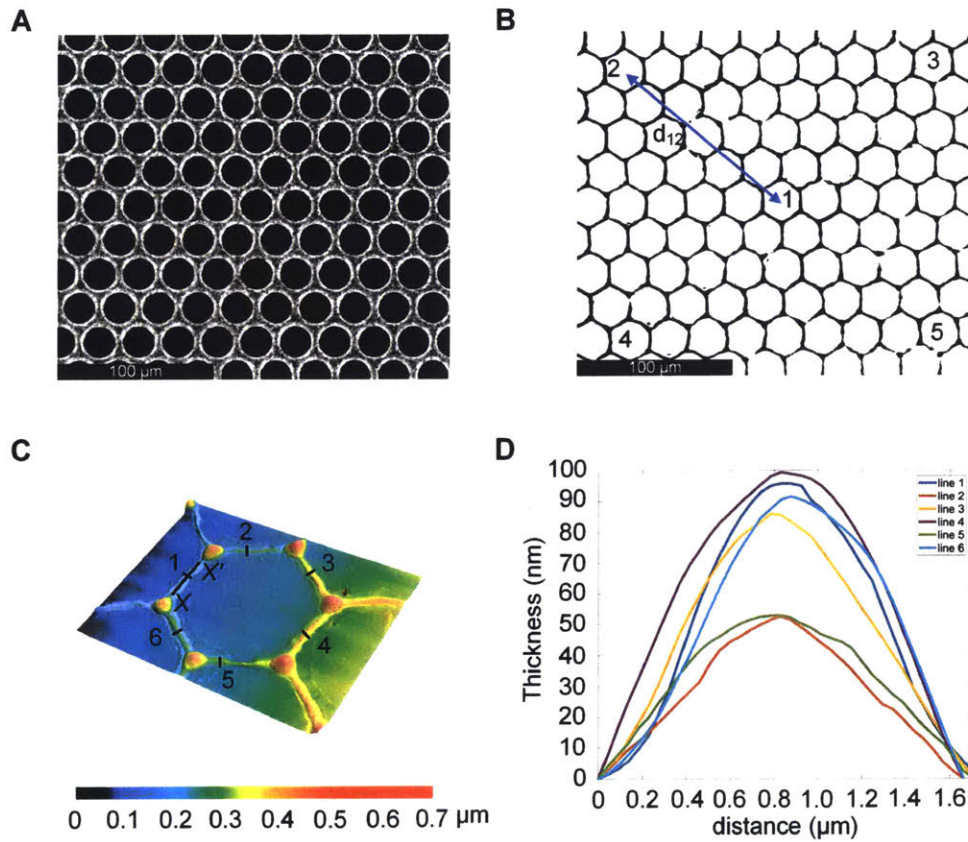
Figure 4-9: Printing of high resolution patterns at 100 mm/sec A) Optical microscope image of stamp shows a honeycomb stamp consisting of hexagons with line width of 2 microns B) Printed pattern sides of the hexagons and the center-center distances of the hexagons have a standard deviation of 1 and 0.26 microns respectively C) Laser scanning confocal microscope image of one of the hexagons in the printed pattern D) Measured profile of the sides of the hexagons show that their average thicknesses are less than 50 nm and have an RMS roughness of 1.1nm except at the corners.

mean diameter of the circle printed at 18 mm/sec is higher than the ones printed at 1 and 100 mm/sec because the excess ink was incompletely removed from the stamp in this experiment.The mean and the standard deviation of the measured sides of the hexagons and the distances between the centers of the hexagons in the printed honeycomb patterns (Fig. 4-9B) are 13.03±1.01μm and 132.71±0.26μm respectively.

4.4.3 Printed layer thickness and uniformity

The profile (Fig. 4-9C) of one of the hexagons in the printed honeycomb pattern was measured using a laser scanning confocal microscope (Keyence Model VK-X250). The thickness (Fig. 4-9D) of the printed layers was measured along the lines that section the sides of the hexagons. The mean and standard deviation of the thicknesses measured along the lines 1-6 are 43.8±11.3 nm. The printed profile measured along XX is highly uniform (RMS roughness = 1.1 nm) except at the corners where the sides meet.

4.5   Conclusions

We designed and fabricated a plate to roll printing apparatus for studying the physics of flexographic printing processes and to prototype devices. We conducted printing experiments by controlling the contact force, alignment, and slip between the substrate and nanoporous printing stamps. With the printing apparatus, we show printing of features of different shapes, resolution and at low and high speeds. The lateral dimensions and the thickness of the printed features show that the machine meets the functional requirements including control of contact force, alignment and slip between the stamp and substrate. Furthermore, the machine can be used to study the physics of nanoporous flexographic printing process, develop physics based models and prototype devices such as transparent conductive electrodes and thin film transistors.

Chapter 5

High-mobility SWCNT Thin-film Transistors Fabricated using Nanoporous Flexographic Printing

5.1   Abstract

The performance of printed electronic devices including displays, RFID tags, and sensors are limited by the speed and thickness of the in-built thin-film transistors. The existing printing technologies such as gravure, inkjet, screen and flexography are limited by the minimum resolution and thickness of the printed layers. Ultra-thin (<500nm), short channel ($\sim 10 \mu$m) transistors with carbon nanotubes (SWCNTs) network semiconductor were fabricated using flexographic printing with nanoporous stamps made of polymer-coated vertically aligned carbon nanotubes (VACNTs). The measured on-off ratios and mobilities of the fabricated devices are 10^3-10^5 and $\sim$25-95 comparable with that of other printed SWCNT network transistors. These are among the thinnest printed TFTs with high mobility and on-off ratio.

5.2 Introduction

High-throughput, low cost manufacturing of electronics including RFID tags [28], sensors, and LEDs will enable applications including smart packaging, flexible and wearable electronics and displays. Silicon microfabrication processes are limited in terms of substrate and throughput and hence there is a need for new manufacturing processes to realize these emerging applications. The adaptation of printing technologies including inkjet, screen, gravure and flexography from printing dyes to functional materials offers a promising alternative. There has been a growth in the last two decades in the production of printed electronic devices. [79, 80] The performance of these devices are determined in most applications by the thickness and speed of the constituent thin-film transistors. [11] The channel length controlled by the separation of the source and drain electrodes and the carrier mobility of the semiconductor determine the speed of the thin-film transistor. Furthermore, thick and non-uniform dielectric and electrode layers lead to lower breakdown voltages due to localized large electric fields. [11] The performance of printed transistors are limited by the performance of extant printing methods. For instance, flexography is a highly scalable, high-speed direct printing method, yet it is limited to resolutions of ~10s of microns as a result of the ink being squeezed out [12, 13, 39] between the stamp and substrate and due to dewetting of the deposited ink film. [14] Broadly, there remains an important need for improved printing technologies for ultrathin (~0.1 μm or smaller) and fine features (~ μm resolution) to advance printed electronics technology. [10] Most of the aforementioned printing technologies use liquid or polymeric inks, often containing colloidal nanoparticles that are sintered to form films after drying of the printed ink pattern. As such, limitations to the feature size and thickness are attributed to the coupled, time-dependent fluid and solid mechanics of the printing process. In flexographic printing, we recently demonstrated that significantly finer printed feature dimensions can be achieved when nanoporous stamps are used instead of traditional non-porous polymer stamps. [20] The key difference is that nanoporous stamps retain the ink within their volume, enabling the printed pattern to precisely

replicate the shape of stamp features without suffering the squeeze-out and dewetting instabilities of traditional flexography. For instance, nanoporous stamps comprising polymer-coated vertically aligned carbon nanotubes (CNTs) enabled high speed (0.1 m/s) printing of features with $\sim 3\mu$m minimum size, from conductive, dielectric, and semiconducting nanoparticle inks.

Nanoporous flexographic printing can be used to print ultra-thin, electrodes with short-channel length. This can be combined with the semiconductor channel consisting of SWCNT networks to produce transistors with high-mobility and on-off ratio. SWCNTs, in addition to having high mobility (>10 cm^2/Vs) can be processed in solution with commercially available inks. [81–84] We show the design, fabrication and characterization of a thin-film transistor (Fig. 5-1A)with short channel lengths and ultra-thin electrodes printed using nanoporous flexographic printing. The measured transistor mobility ($\sim$25-95) and on-off ratio ($\sim 10^3 - 10^5$) are comparable with other printed SWCNT transistors. The thickness of the TFT except the substrate is < 500 nm and can be reduced further by reducing the dielectric layer thickness. Furthermore, nanoporous flexographic printing can be used to print transistors on flexible substrates at high speeds (>0.1 m/s).

5.3 Methods

5.3.1 Stamp fabrication

The stamp consists of pairs of source and drain electrodes with different channel lengths (L=5-150μm) and fixed width (W=200m). An exemplary stamp is shown in Fig. 5-1B. To fabricate the stamps [20], first vertically aligned CNT arrays (CNT forests) are grown on lithographically patterned silicon substrates by atmospheric pressure chemical vapor deposition (CVD). Then, the top entangled crust layer (<1 μm thickness) is removed by a brief oxygen plasma etching (Diener, Femto Plasma System) and coated with a thin layer ($\sim$20 nm) of poly-perfluorodecylacrylate (pPFDA) using initiated CVD (iCVD). [17, 20, 21]The plasma etching is critical to remove the

A

V_G V_S V_D

Source/Drain Electrodes (Ag)

Dielectric (SiO$_2$)

Gate (p-doped Si)

Semiconducting layer (SWCNT network)

200 µm

B

10 µm

100 nm

100 µm

100 nm
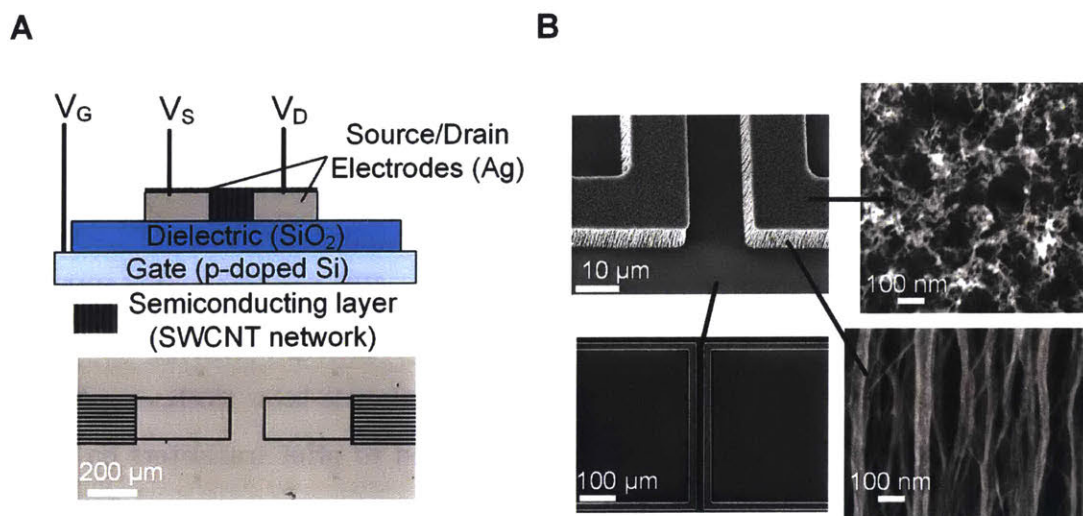
Figure 5-1: Ultra-thin Transistors with short channel lengths ($\sim$10 µm) S/D Electrodes Printed using Nanoporous Flexography Stamps A)Schematic of the device shows the bottom gate (p-doped Silicon), Silicondioxide dielectric layer, printed source and drain electrodes and the top contact semiconducting SWCNT layer and microscope image of the printing stamp showing the channel geometry defined by the source and drain electrodes B) SEM images of the stamp to print source and drain electrodes (10 µm length, 200 µm width) used for nanoporous flexography; close-up top and side surfaces of the stamp reveal pores with $\sim$100 nm width.

stiff and rough crust which is not desirable for high-resolution printing because it results in non-uniform contact against the target substrate. The pPFDA coating followed by second plasma treatment allow liquid infiltration and solvent evaporation without shrinkage or collapse of the CNT forest by elastocapillary densification. The final plasma-treated pPFDA-CNT microstructures are highly porous (>90 % porosity) with nanometer pore size ($\sim$100-200 nm), allow liquid infiltration without deformation due to capillary forces, and are mechanically compliant, enabling uniform contact with the target substrates.

5.3.2   Inking

The ink used in this study is composed of silver nanoparticles dispersed in tetradecane (Sigma-Aldrich, 736511). The surface tension and viscosity of the ink are 27 mN/m and 10 mPa-s, respectively, and the ink exhibits good conductivity (30-60% of bulk silver) after annealing. [20] The particle concentration is 50-60 wt% with particle sizes less than 10 nm. A 100 μl droplet of ink is pipetted onto the stamp and then the stamp is spun to 1500 rpm for 1-3 minutes in a spincoater.

5.3.3   Sintering

A hot plate was used to do rapid sintering of the silver nanoparticles after printing the source and drain electrodes. The hot plate was set to the 300 0^C and the chips were placed on the hotplate after it reached the setpoint. The wafer was left on the hot plate for 1 minute for sintering.

5.3.4   Device characterization

A DC probe station and semiconductor parameter analyzer (Agilent 4155C, Easy Expert software) were used for the measurement of conductivity of the sintered electrodes, and the output and transfer characteristics of the TFTs.

5.4 Results and Discussion

5.4.1 Device design and fabrication

We designed and fabricated bottom gate, top-contact transistors (Fig. 5-1A). The device consists of p-doped silicon gate electrode (resistance $= 0.001$-0.005 Ω-cm, thickness $= 500$ μm), thermally grown silicon dioxide (thickness $= 300$nm) dielectric layer, silver source and drain electrodes (thickness ~ 100-200nm), and single-walled carbon nanotubes (SWCNTs) network semiconducting layer. We used commercially available silicon wafers (University Wafer Product No. 1583) on which the source and drain electrodes were printed with silver nanoparticle inks using nanoporous flexographic printing stamps. After printing and solvent evaporation, silver nanoparticles were sintered to form a continuous layer with high conductivity (50-60% of bulk silver). We deposited the SWCNTs by spincoating to achieve a high-density network (>40 SWCNTs/μm^2)

5.4.2 High resolution printing ($L < 10\mu$m) using nanoporous stamps

Nanoporous stamps retain the ink within their volume, enabling the printed pattern to precisely replicate the shape of stamp features without suffering the squeeze-out and dewetting instabilities of traditional flexography. The contact pressure between the stamp and substrate must lie within a range determined by the stiffness of the CNTs, CNT-CNT spacing, and the standard deviation of the lengths of CNTs, assuming the lengths are normally distributed. In a prior work, we estimate the pressure range where the area ratio (ratio of area of stamp pattern pattern to printed pattern) is ~ 1 using experiments and analytical modeling. We apply the pressure within this range to print the electrodes so that the channel length in the printed patterns match that in the printing stamp. The thickness of the printed layer can be controlled via the speed at which the stamp is retracted away from the substrate after contact. During printing, we retracted the stamp quasi-statically enabling printing of layers

with thickness > 200nm. After solvent evaporation, printed layers composed on silver nanoparticles are highly uniform.
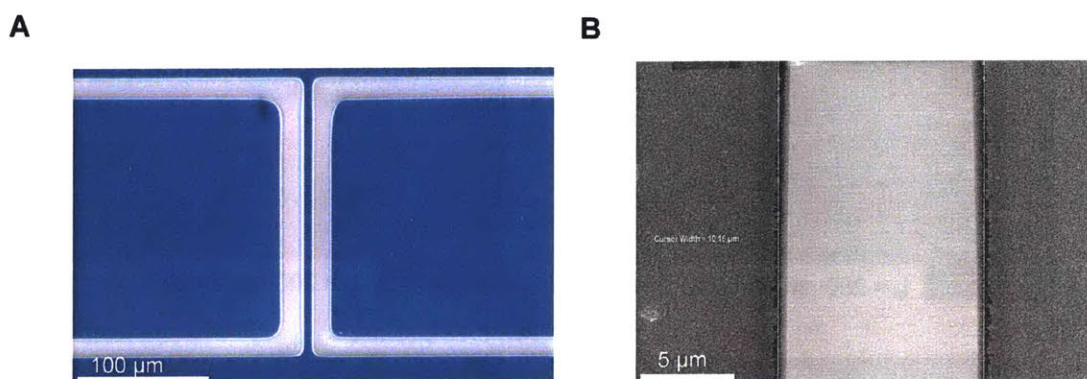

Figure 5-2: Fabrication of S/D electrodes by printing silver nanoparticles and forming a continuous layer by sintering A) Microscope image of the sintered source and drain electrodes has a channel of ~10μm length and 200μm width B) SEM image of the sintered source and drain electrodes shows coarsened and densified silver nanoparticles forming a continuous thin film

5.4.3 Sintering of silver nanoparticles

The samples were sintered by placing them on a hot plate for 1 minute after the hot plate had reached a set temperature of 300^{0}C (Fig. 5-2). During sintering, nanoparticles coarsen and densify to form a continuous film with few voids. We sintered the printed samples of varying thickness (50 < t < 250nm) at 200, 250, 300, 350 and 400^{0}C for 10 minutes(Fig. 5-3, 5-4). We used the SEM images of the sintered
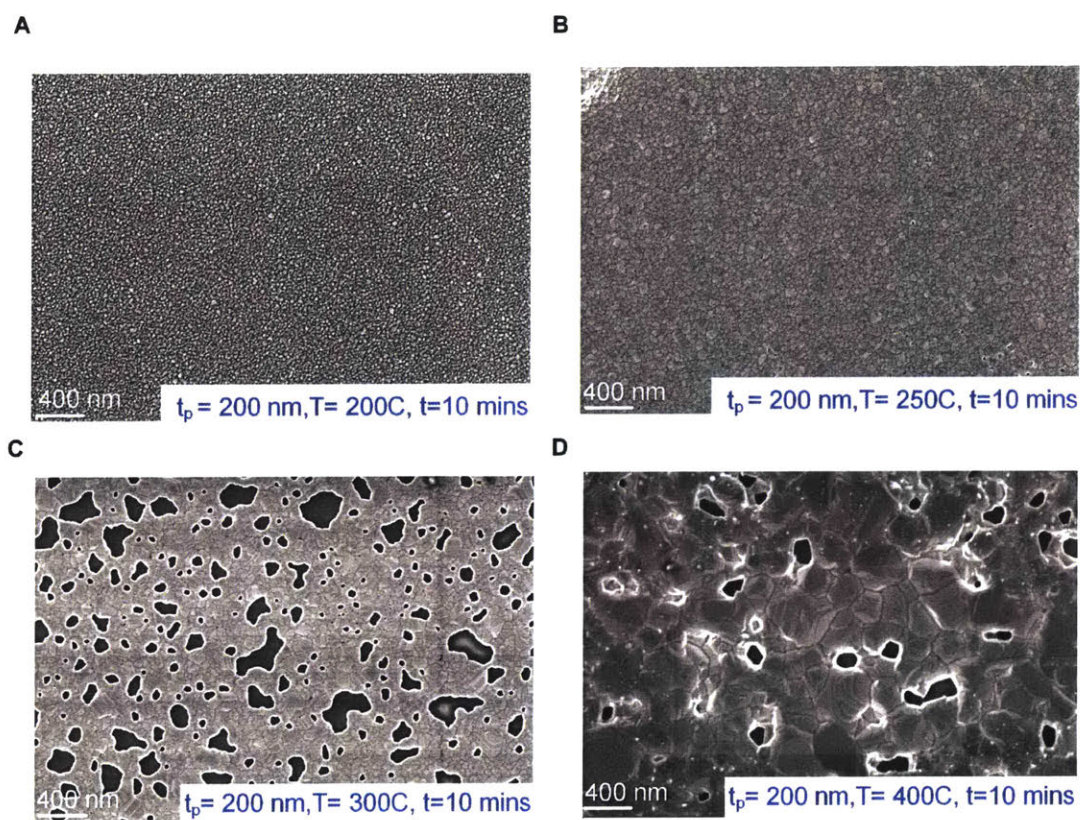
Figure 5-3: Sintering causes coarsening and densification of ~200nm thick layer of silver nanoparticles printed with nanoporous stamp A)Coarsened silver nanoparticles after 10 minutes of sintering at a temperature of 200^0C B)Sintering at 250^0C shows coarser grains compared to the ones formed at 200^0C and formation of continuous layer by densification C)At 300^0C, layers consist of larger grains, more densification yet voids have formed leading to the formation of discontinuous regions D) Sintering at higher temperatures (400^0C) leads to formation of larger voids and discontinuous layer

samples to assess the continuity of films qualitatively and measured the conductivity of films. From the SEM images and conductivity measurements, we determined the optimal sintering condition was 300^0C for 1 minute. At temperatures below 300^0C, coarsening and densification is insufficient lowering the conductivity. At temperatures above 300^0C, though continuous films with large grains form locally, several voids form leading to lower conductivity for thin films (t<100nm). Therefore, we determined the optimal sintering condition was 300^0C for 1 minute(Fig. 5-5). The measured conductivity (Fig.)of the sintered source and drain electrodes was 4.5 x 10^7 S/m, which is 70% of that of bulk silver(Fig. 5-6).
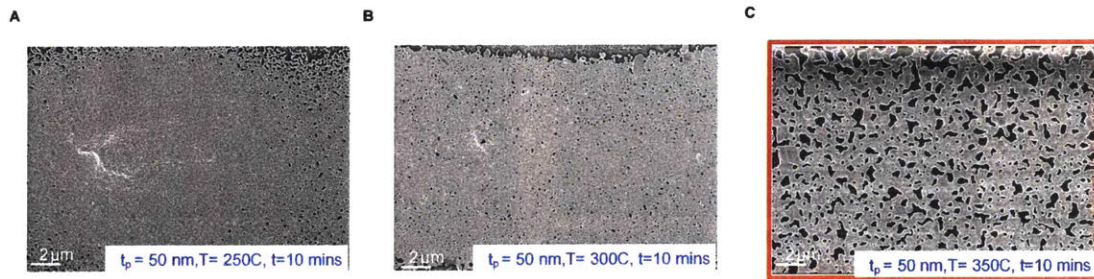
Figure 5-4: Dewetting of Ultra-thin ($\sim$50nm) printed layers by sintering at high temperatures ($>350^0C$ A)Continuous layers are formed by sintering at 250^0C B) Formation of voids are observable at 300^0C C) at 350^0C, voids grow and join leading to dewetting leading to a discontinous sintered layer
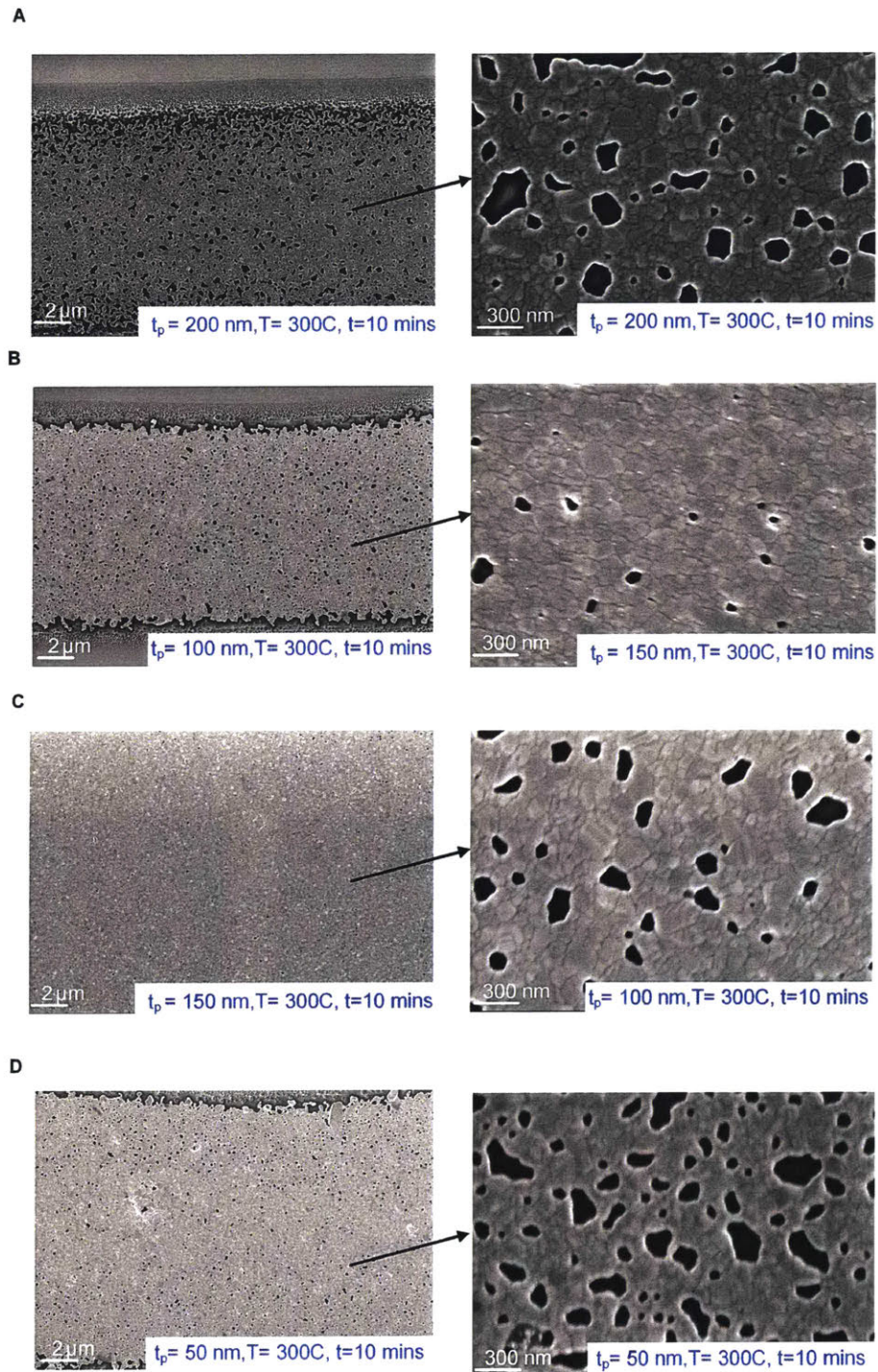
Figure 5-5: Optimal sintering temperature is 300^0C for $50 < t_p < 200nm$ to form continuous layers with minimal numbers of voids as illustrated by layers sintered for 10 mins at 300^0C with thickness of A) 200nm B) 150nm C)100nm D) 50 nm
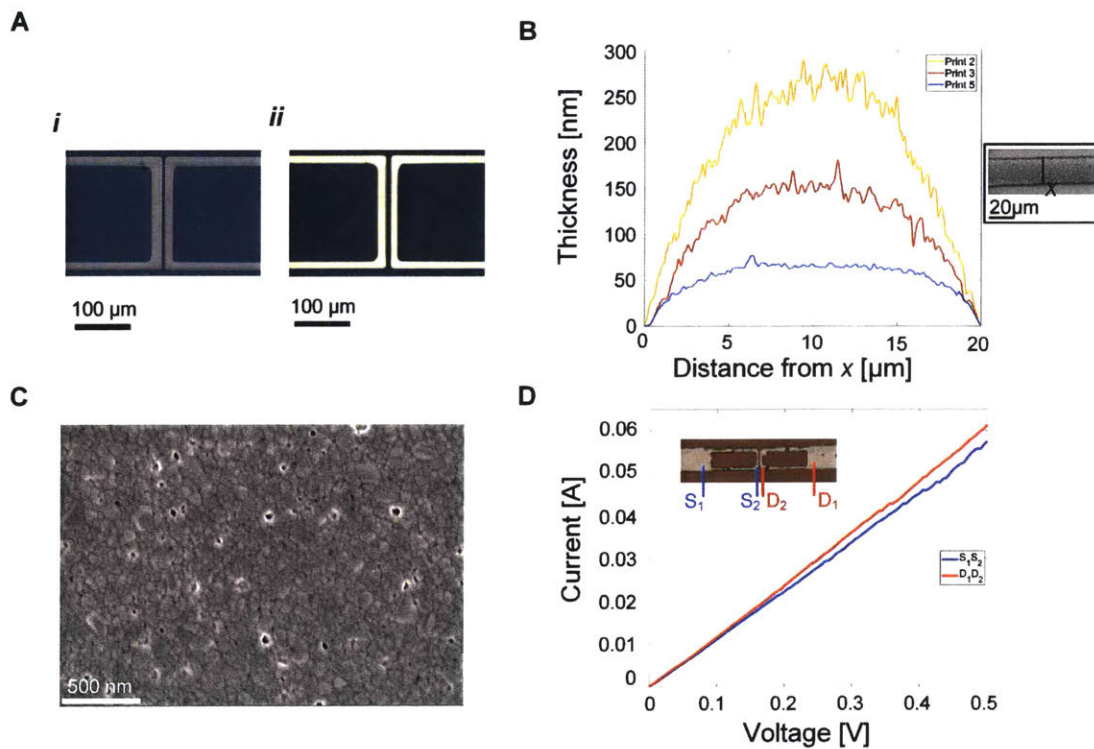
Figure 5-6: Sintering of printed silver nanoparticles to achieve a conductivity of 70% of bulk silver A) Microscope images of printed and silver nanoparticles shows insignificant change in the geometry of the electrodes before and after sintering B) Profilometer measurement shows the profile of the sintered electrodes; thickness decrease with sequential printing from ∼200 nm average thickness to ∼50nm and have an RMS roughness of ∼1 nm C) SEM image of the sintered electrodes shows nanoparticles coarsen and densify by sintering and form a continuous layer with few pores D) Conductivity measurements show that the VI characteristics of source and drain electrodes are linear

5.4.4 Deposition of SWCNT network semiconducting layer by spincoating

The organic solvent based ink used in the device does not require any surface treatment before deposition. To deposit the semiconducting layer, a 300 μl droplet of ink (NanoIntegris, IsoSol-S100, 99.9% purity) was pipetted onto the wafer and then the wafer was spun to 1500 rpm for 15 seconds in a spincoater. The measured density of the network of SWNCTs is $\sim$100 SWCNTs/μm^2(Fig. 5-7). The density must be above the percolation threshold [85, 86]($>$ 40 SWCNTs/μm^2) to have high on-conductance and mobility. Since the ink has 99.9% purity, density does not affect the on-off ratio. The density can be tuned by the volume of the droplet and the spincoating speed and duration.

5.5 Characterization

5.5.1 Transfer characteristics

We measured the transfer characteristics of the fabricated transistors by varying V_g from -10V to +10V and measuring I_d for V_d =500mV, 1V, 3V, 5V,10V. (Fig. 5-8A) shows the transfer characteristics for the transistor with $L \approx 10\mu$m. The on-off ratio of the transistors are $\sim$10^3-10^5 and the threshold voltage varies from 1-8V .

5.5.2 Output characteristics

We measured the output characteristics by varying V_d from -10V to +10V and measuring Id for V_g =500mV, 1V, 3V, 5V, 7V, 9V,10V. (Fig. 5-8B) shows the output characteristics for the transistor with $L \approx 10\mu$m. The maximum ON-current in saturation region varies from 25-275μA when V_g is varied from 500mV-10V.
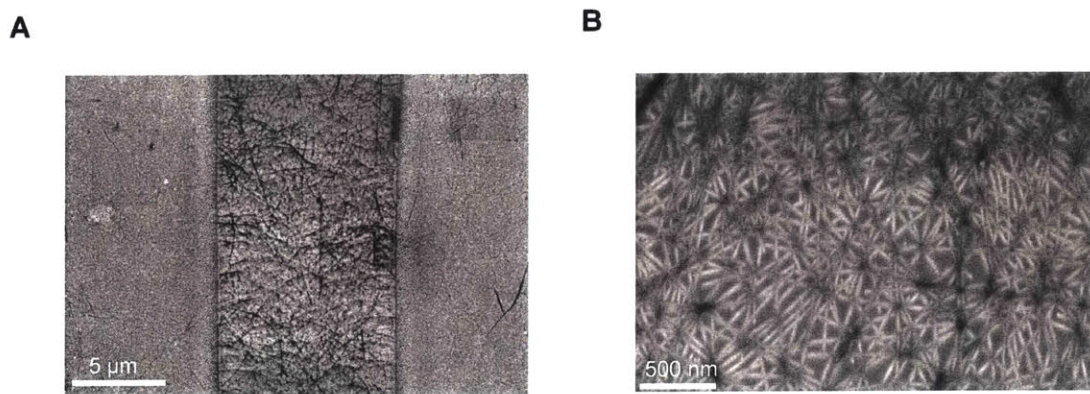
Figure 5-7: Deposition of SWCNT networks with organic solvent based ink A) Top-contact SWCNT semiconducting layer formed from deposition of organic solvent based high-purity (99.9% semiconducting SWCNTs) ink B) The density of SWCNT networks is $\sim$100 SWCNTs/μm^2
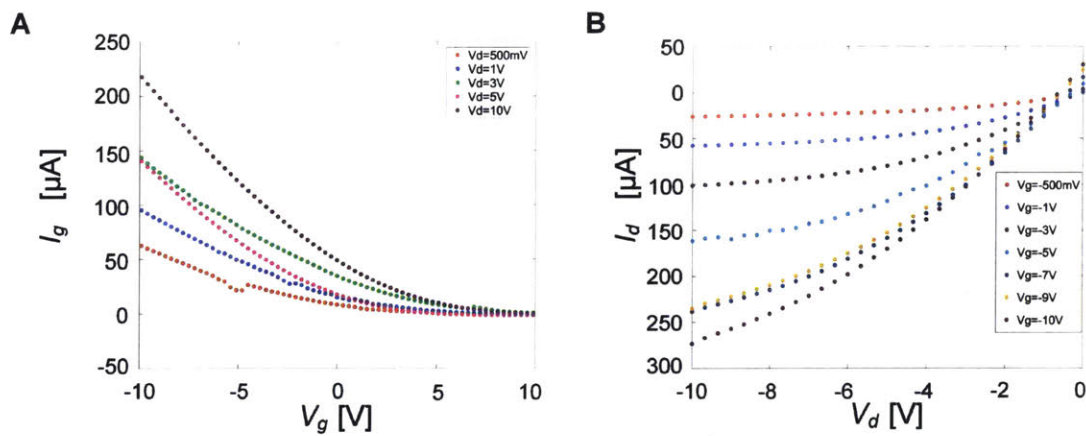
Figure 5-8: Characterization of the transistors (channel length $= 10\mu$m) by the measurement of transfer and output characteristics, calculation of mobility and resistance and their variation with channel length A) Transfer characteristics measured by varying V_g from -10V to +10V for V_d =500mV, 1V, 3V, 5V,10V show the threshold voltage of 1-8V B) Output characteristics measured by varying V_d from -10V to +10V for V_g =500mV, 1V, 3V, 5V, 7V, 9V,10V show the linear and saturation regions with the maximum ON-current in saturation region varying from 25-275μA

5.5.3 Effect of channel length

(Fig. 5-9A) shows the comparison of output characteristics at V_d =1V of three devices with channel lengths varying from 10 -139μm. In the saturation region, maximum ON current $|I_{ON_{max}}|$ increases from $\sim$30-60 μA as the channel length increases from 10 -139 μm. In the linear region, the slope of I_d-V_d plot and hence the transconductance increase with decreasing channel length. This is also shown by the linearly increasing resistance (Fig. 5-9B) from $\sim$75-100 kΩ as the channel length increases from 10 -139 μm. Comment on the resistance values. (Fig. 5-9C) shows the comparison of transfer characteristics at V_d =1V of three devices with channel lengths varying from 10 -139 μm. With decreasing channel length, threshold voltage increase from $\sim$1V to 7V. We calculate the slope near $V_d = V_T$, and calculate the mobility using the following equation (see Supporting Information)

$$\sqrt{I_d} = \sqrt{\frac{\mu C_{ox} W}{2L}}(V_{gs} - V_T) \qquad (5.1)$$

where μ, C_{ox} V_T are mobility, oxide capacitance and threshold voltage respectively. Mobility calculated from the transfer characteristics show that mobility increases from 25 cm^2/Vs for L=10 μm to 95 cm^2/Vs for L=63 μm and then decreases to 80 cm^2/Vs for L=139 μm(Fig. 5-9D). The mobility variation with channel length is likely due to the variation in the SWCNT network density between the devices of different channel lengths. Comment on the mobility values.

5.5.4 Comparison of performance with the prior art

The ON-OFF ratio and the mobility of the transistors are 10^3-10^5 and $\sim$25-95 and these values are comparable to other printed transistors. [23, 24, 81 83, 87 91] We have shown high-speed printing with nanoporous stamps in a prior work. [16] Using nanoporous flexographic printing, we can achieve high speed manufacturing of ultra-thin ($<$500nm) TFTs with high mobility and ON-OFF ratio.

93
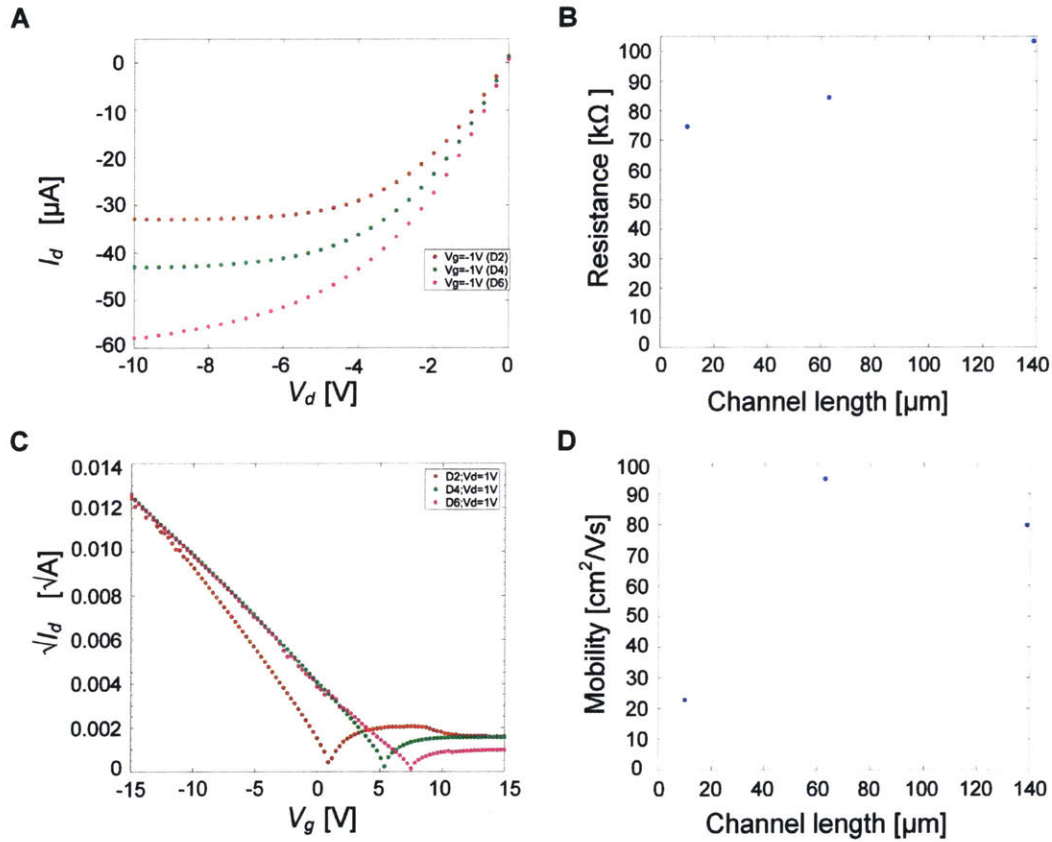
Figure 5-9: Comparison of characteristics of devices with different channel lengths A) Comparison of the output characteristics of three devices (D2: L= 139 μm , D4: L= 63 μm ,D6: L=10 μm) at V_g =-1V show the conductance in the linear region and the maximum ON-current in the saturation region at 10V increasing with decreasing channel length B) Resistance in the linear region increase with channel length C) Comparison of the transfer characteristics of three devices (D2: L= 139 μm , D4: L= 63 μm ,D6: L=10 μm) at V_d =1V show the threshold voltage increase from 1V to 7V with decreasing channel length D) Mobility calculated from the transfer characteristics show variation with channel length due to the variation in the SWCNT network density between the devices of different channel lengths

5.6 Limitations

In this work, we have shown the application of nanoporous flexography to print ultra-thin source and drain electrodes with short channel lengths. Though we have demonstrated a TFT with good performance characteristics, we have not shown a fully printed transistor on flexible substrates. Nevertheless, nanoporous flexography can be used to print gate, dielectric layers in addition to the source and drain electrodes on flexible substrates. By using layer to layer registration and achieving a designed overlap between the S/D electrodes and dielectric layer, leakage currents can be reduced to achieve even higher on-off ratios ($> 10^6$) than what has been achieved in this work.

5.7 Conclusions

We have shown the design and fabrication of ultra-thin, short channel length thin-film transistors using nanoporous flexographic printing. The top-contact bottom gate TFTs were fabricated by printing S/D electrodes on a silicon wafer with a thermally grown SiO_2 dielectric layer and p-doped Si gate layer. The printed electrodes were sintered and the high-purity SWCNTs (99.9% semiconducting) were deposited on the top of the S/D electrodes. The transfer and output characteristics were measured and the on-off ratios, mobility and transconductance values were calculated from the measured characteristics. The measured on-off ratios and the mobilities are 10^3-10^5 and $\sim$25-95. These TFTs are among the thinnest printed transistors with high mobility and on-off ratio. The performance can be further improved by introducing a diffusion barrier layer between the S/D electrodes and the dielectric layer reducing the leakage current and increasing the on-off ratio. This work demonstrates the applicability of nanoporous flexographic printing to fabricate ultra-thin, short channel length transistors with high mobility. The process can be scaled up for high-speed plate to roll manufacturing of TFTs on flexible substrates.

Chapter 6

Quantum Dot Pixels Printed Using Nanoporous Flexography for Spectrometry Application

6.1 Abstract

Quantum dots (QDs) have excellent long-term stability and finely tunable absorption spectra across wide range of spectral wavelengths. QD absorption spectra can be varied continuously over wavelengths ranging from UV to mid-IR by changing the size, shape and composition of the QDs. Using a 195 color QD filter array [92], a point spectrometer has been demonstrated to operate in the visible wavelength to do low cost high resolution visible spectroscopy for drone-based crop field monitoring or food ripening detection applications. Existing printing technologies are not suitable for precision patterning of individual QD micropixels. Here, we use nanoporous flexography for printing high-resolution pixels and color filters for QD spectrometers. The method allows direct printing of electronic ink features with micron-scale lateral dimensions (<10 microns), submicron line edge roughness (< 1 micron) and highly uniform thickness in the sub-100 nm range. We print a sub-array of different QD color pixels, called super pixels(Fig. 6-1) [93].
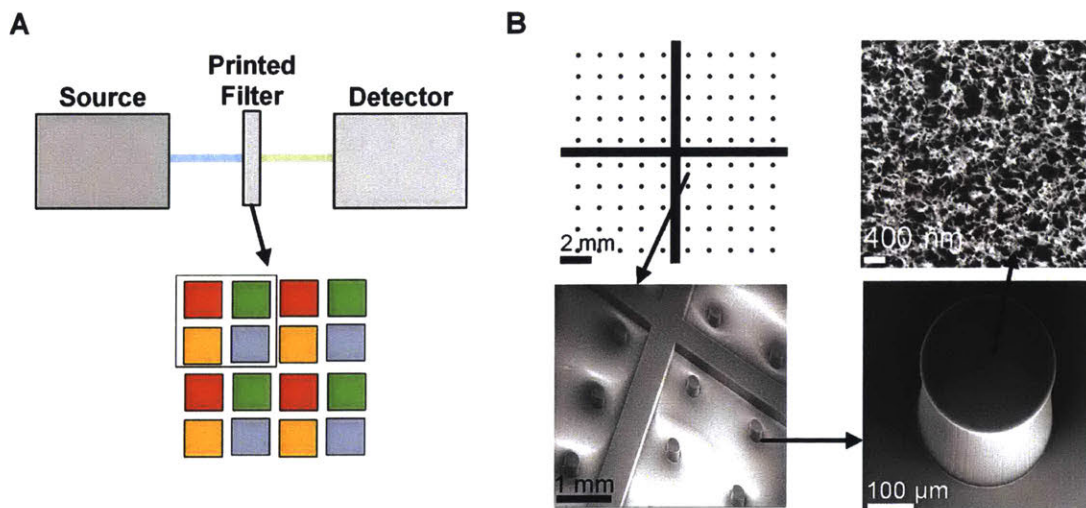
Figure 6-1: Spectrometer and nanoporous printing stamps

6.2 Results and Discussion

6.2.1 Quantum dot ink synthesis and characterization

Quantum dot is an inorganic semiconductor nanoparticle with sizes ranging from 2-15 nm in diameter. The transmission electron microscope image of a typical quantum dot is shown in the figure below. These quantum dots are synthesized at high temperature to achieve high crystallinity and size. monodispersity [92] [93].

6.2.2 Printing CQD pixels and optical characterization

We determined the ink concentration and ink loading [16] required to achieve a printed layer thickness of 300nm-1μm. Fig. 6-2 shows patterns of colloidal quantum dots printed with nanoporous stamps. The thickness and optical absorbance of these patterns were measured using profilometery, confocal microscope imaging and spectrophotometer.

6.2.3 Printing multicolor pixels with a nanoporous stamp

We designed masks consisting of 20x20 mm size chips. These chips were designed to have four quadrants separated by two walls.Fig. 6-1 shows the mask design and a fabricated nanoporous stamp. 25μliters of each of the four CQD inks were pipetted in each of the quadrants and the stamp was spun on a spincoater. The porous stamp wells prevent the mixing of the CQD inks during pipetting and spincoating. The inked stamp has four regions coated with four CQD inks(Figs. 6-1 6-3). A printing apparatus consists of a flexure attached to a XY motion stage holds the inked nanoporous stamp. The glass slide substrate was attached to a fixture with a double sided tape. Behind the glass slide, a microscope connected to a Nikon D5100 DSLR camera is placed. First, the stamp was brought into contact with the substrate and the pixels were printed. Next, using the camera image as the position feedback, XY motion stages were moved so that the stamp was moved along the X or Y directions by an incremental distance equal to the center to center separation

A

B

C

D
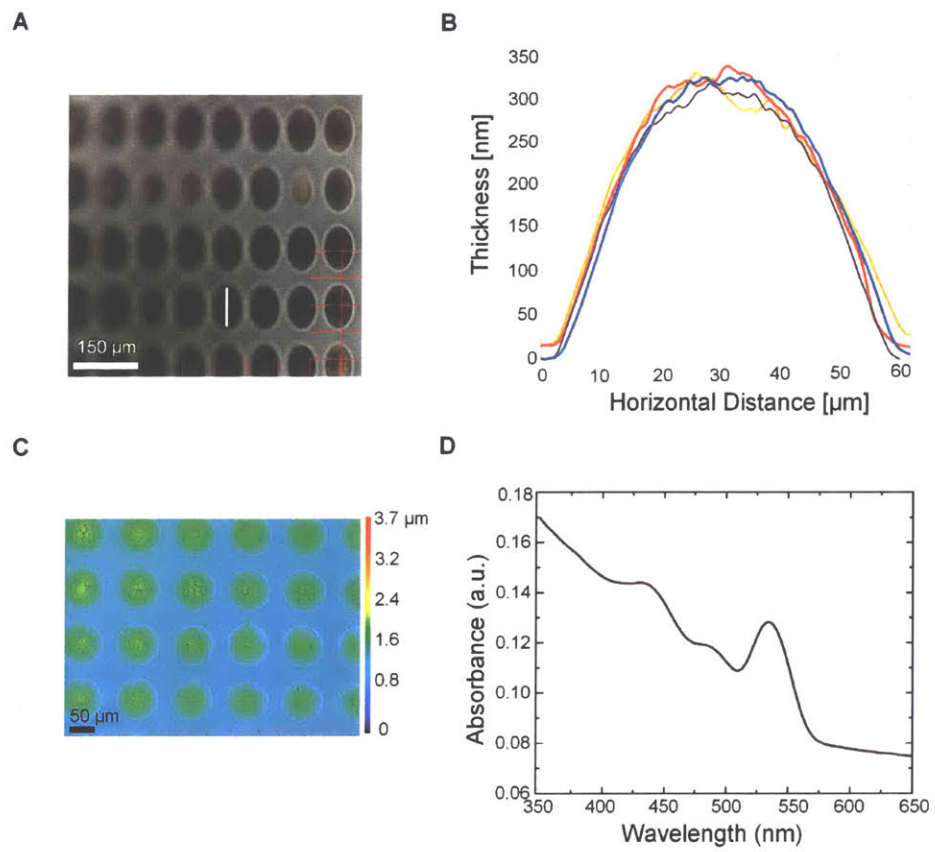
Figure 6-2: Printing quantum dots with nanoporous stamps and characterization

between two pixels within the super pixel. Under ideal conditions, with four steps, a super pixel can be printed. Fig. 6-4 shows two color super pixel printed with the four quadrant nanoporous stamp using the printing apparatus and process.
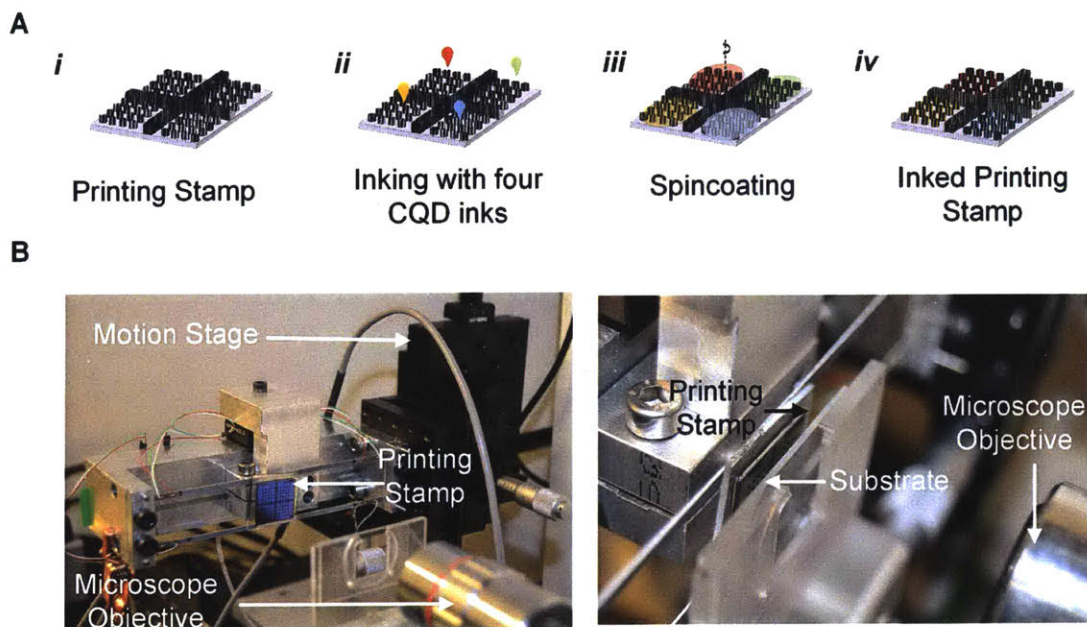
Figure 6-3: Printing Process and Apparatus

6.3 Conclusion

We designed a four quadrant nanoporous stamp. We inked these stamps with four CQD inks, used a precision plate to plate printing apparatus and printed two color super pixels. This work is a proof of concept that demonstrates that multicolor CQD pixels with desired optical properties can be printed using nanoporous flexographic printing stamps. There is further work required in the following areas - printing 10 x 10 super pixel in 10 x 10 mm dimension, optical calibration on QD filter chip,

A

B

1 mm
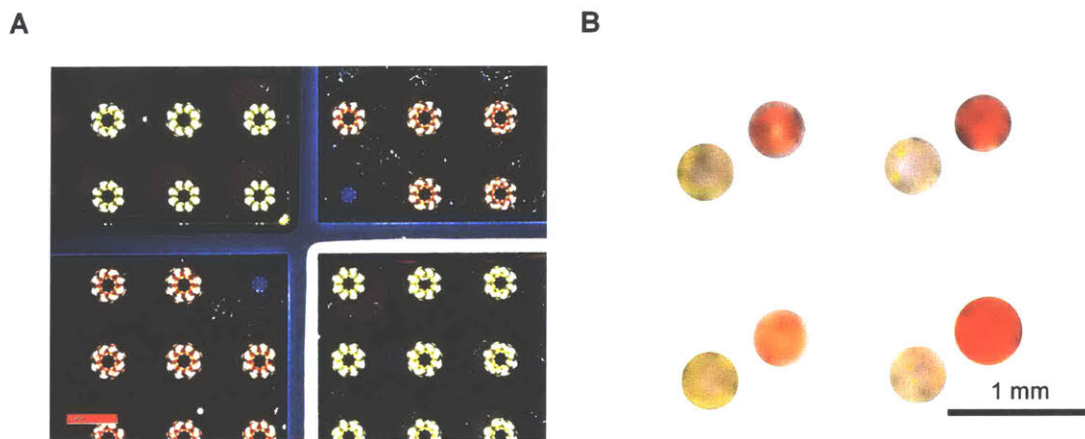
Figure 6-4: Printing two color super pixels with nanoporous stamps

integration onto a CCD detector and developing and optimizing the spectrum/spatial reconstruction algorithm.

Chapter 7

Conclusions

7.1 Thesis Contributions

7.1.1 Fundamentals of flexographic printing with nanoporous stamps

To print devices such as transistors, printing uniform ultra-thin films in a controllable manner is a critical process capability. This study provides the understanding of process physics and the predictive models. The contributions of this work include the following.

1. **High-speed imaging of liquid transfer from a nanoporous stamp to a spherical substrate :** A custom-built high-magnification, high speed imaging printing apparatus to print with nanoporous stamps on spherical lenses was used to conduct the experiments.

2. **Approach speed determines the spreading dynamics:**

   - at low speeds ($v_a < v^*$), wetting is driven by capillary force and independent of approach speed.

   - at high speeds ($v_a > v^*$), wetting is driven by contact and wetting speed scales with approach speed.

3. **Retraction speed determines the transferred liquid volume:** During retraction, a liquid bridge forms between the stamp and the substrate. At a critical bridge height ($h_b = 2\pi r_b$), the bridge ruptures transferring liquid from the stamp to the substrate

   - at low speeds ($v_r < 2v^*$), flow from the nanoporous stamp fills the liquid bridge between the stamp and substrate leading to a high volume of transfered liquid volume

   - at high speeds ($v_r > 2v^*$), flow from the nanoporous stamp is negligible leading to transfering of a thin liquid film

4. **Respreading on precursor films influences print lateral resolution:** The transferred liquid spreads to fill the shape of the prior contact area, forming a thin film; and the contact area is determined by the contact pressure and surface roughness.

7.1.2 Applications of nanoporous flexographic printing

1. **Printed S/D electrodes for thin-film transistors**

   (a) Fabricated ultra-thin (<500nm) thin-film transistors (TFTs) with short channel length ($L \sim 10\mu m$) and high-mobility. Flexographic printing with nanoporous stamps was used to print the source and drain electrodes consisting of sintered silver nanoparticles

   (b) Demonstrated that the TFTs have high-mobility ($\sim$25-95) and on-off ratios ($\sim 10^3 - 10^5$) comparable to other TFTs fabricated with single-walled carbon nanotubes (SWCNTs) network as the channel material

2. **Printed quantum dot color filters for imaging spectrometer**

   (a) Demonstrated printing two color super pixels using nanoporous stamps.

   (b) Designed and fabricated stamps with four quadrants that can be inked with four different quantum dot inks with different absorption spectra.

(c) Developed a printing apparatus with registration capability and printed two color super pixels.

7.1.3 Scaling the process

1. Designed and developed a desktop printing apparatus to do printing experiments with nanoporous flexographic stamps. The unique features of the machine are

   - Flexure-displacement sensor subsystem to control the stamp-substrate force to a minimum of 0.2 mN

   - Independently driven rotary and linear motion stages synchronized to provide slip-free smooth motion at low (<1mm/s)and high speeds(>0.1m/s)

   - Strain gages and tip-tilt stage to achieve alignment along the moving stamp-substrate contact line

2. Demonstrated printing of micron sized features with silver ink on PET substrates at low (=1mm/sec) and high speeds (>0.1m/s)

7.2 Future Work

7.2.1 Fundamentals of flexographic printing with nanoporous stamps

1. **Effect of stamp porosity** The study of spreading and retraction dynamics during printing with nanoporous shows that the critical speed v^* is a function of stamp porosity. The visualization experiments with nanoporous stamps with varying porosity will be valuable to gain further understanding of the role of stamp porosity on the spreading and retraction dynamics. Fig. 7-1 shows preliminary results from printing experiments conducted with nanoporous stamps with different porosities. In these experiments, nanoporous stamps with different coating thicknesses were fabricated (as outlined in Chapter 2) and printing

experiments were conducted. In the extreme case of low porosity, the volume of ink in the stamp is the lowest and hence the transferred volume is the lowest.In the other extreme of almost no coating, though the porosity is maximum, the stamps will experience elastocapillary densification and hence the volume of ink in the stamp is the lowest. Between the two extremes, accordingly, an optimal coating thickness will exist for maximizing the volume of ink loaded in the stamp and transferred to the substrate.

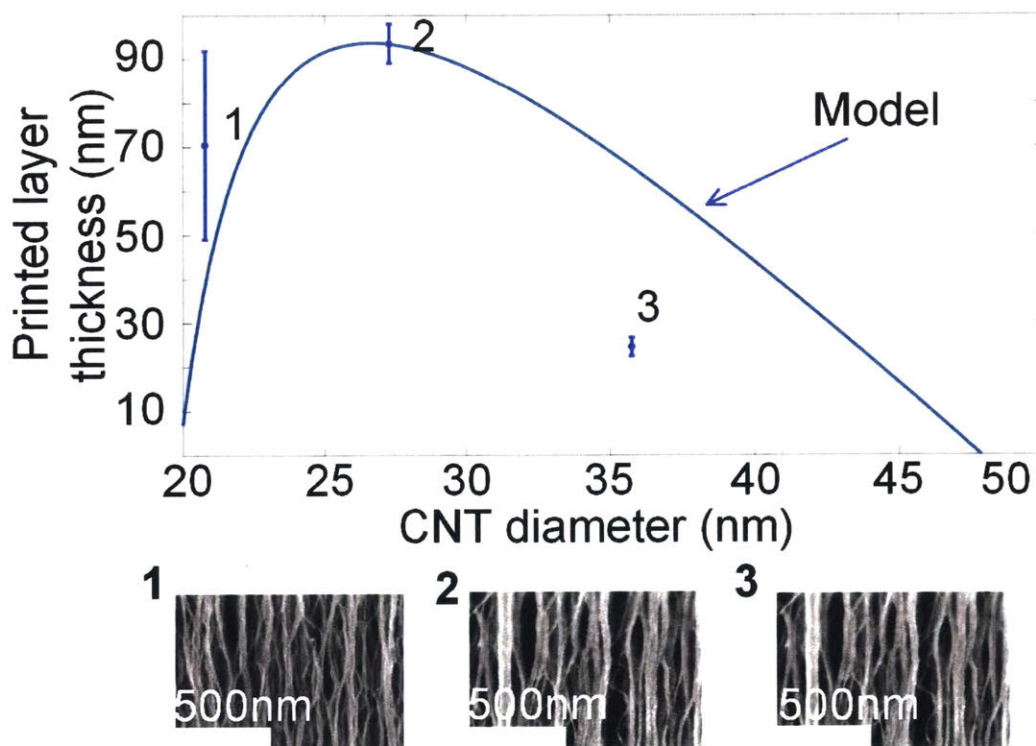Figure 7-1: Printed layer thickness variation with stamp porosity

2. **Deterministic inking of nanoporous stamps** The experiments presented use an inking procedure that works well for printing devices and to conduct visualization studies presented in the thesis. However, there are two questions that remains unanswered

   (a) How can we quantify the volume of ink in the stamp after spincoating ?

(b) Are there alternative inking methods that can load the stamp with a defined volume of ink ?

We conducted experiments where laser scanning confocal microscope was used as a tool to image the inked stamp and measure the quantity of ink in the stamp. Nanoporous stamp was inked using spincoating. After spincoating, excess ink was removed from the stamp by contacting the inked stamp with a non-patterned CNT forest. Then, the inked stamp was used to conduct a series of prints on slides. Confocal images of the stamp was taken after spincoating, second and sixth print and the roughness of the inked stamp surface was obtained from the confocal microscope images of the stamp at various stages. Fig. 7-2 shows the confocal images and the comparison of roughness values at different stages. These are insufficient to calculate the percentage change in the volume of ink in the stamp. There is some loss of ink during the spincoating process and due to evaporation. It is important to be able to determine the volume of ink in the stamp at the start of a printing experiment. The ink volume in the stamp is an unknown parameter that affects the accuracy of the transfered ink volume predictions presented in Chapter 3.

3. **Driving pressure** (ΔP) is treated as a fitting parameter in the models presented in Chapter 3. A physics based model or a set of well-designed experiments to determine the pressure gradient will make the spreading and retraction dynamics model predictions more precise.

4. **Understanding of the role of stamp deformation on liquid transfer** The stamp deformation likely plays an important role in the ink transfer dynamics while printing with nanoporous stamps. This work does not consider the effect of stamp deformation and it needs further research.

5. **Process physics studies with the plate to roll printing apparatus** The primary objective of designing and fabricating the plate to roll printing apparatus was to use it as a platform for studying the effect of processs parameters
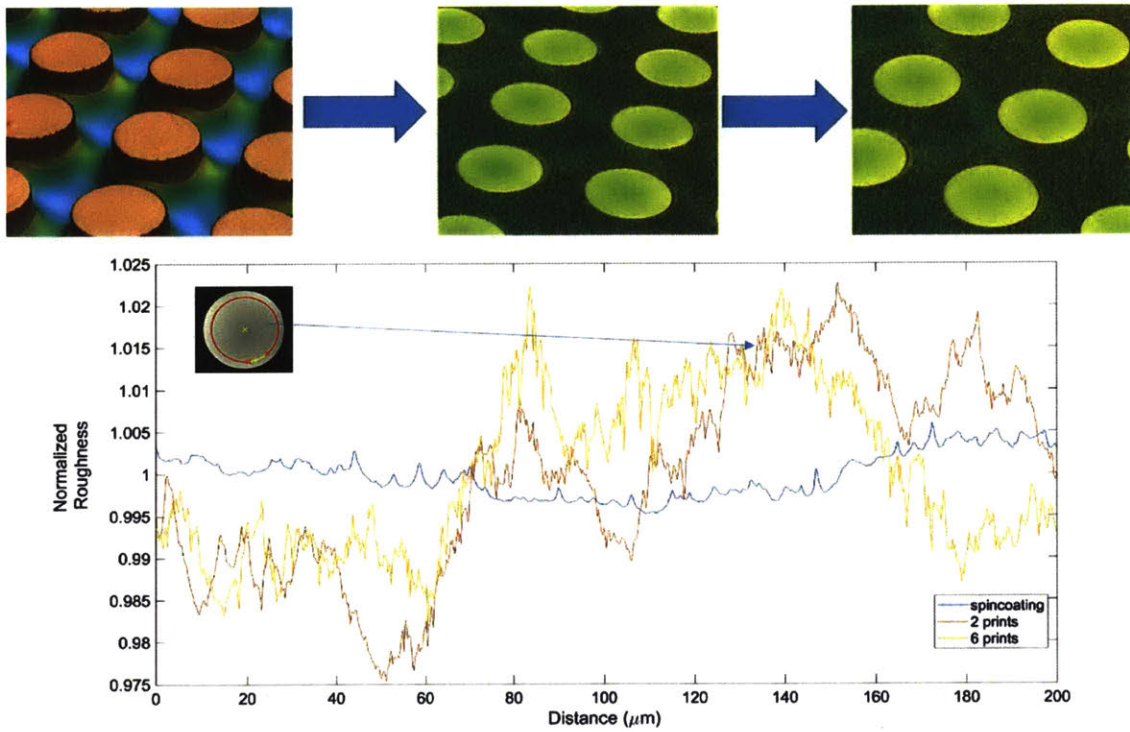
Figure 7-2: Confocal microscope imaging to measure ink volume on the stamp surface

(example : printing speed) on print quality (example : printed layer thickness). In chapter 3, we presented a relationship (Eq. 3.9)between the tangental speed in the P2R apparatus and the retraction speed in the P2P printing experiments. Further studies with the P2R apparatus are required to validate the relationship between printing speed and printed layer thickness and gain further understanding of the physics of nanoporous flexographic printing.

7.2.2 Applications of nanoporous flexographic printing

1. **Thin-film transistors** In this work, we have shown the application of nanoporous flexography to print ultra-thin source and drain electrodes with short channel lengths. Though we have demonstrated a TFT with good performance characteristics, we have not shown a fully printed transistor on flexible substrates. Nevertheless, nanoporous flexography can be used to print gate, dielectric layers in addition to the source and drain electrodes on flexible substrates. By using layer to layer registration and achieving a designed overlap between the S/D electrodes and dielectric layer, leakage currents can be reduced to achieve even higher on-off ratios ($> 10^6$) than what has been achieved in this work.

2. **Uniform printing across 20x20mm area** Printing features (example : QD color pixels) across a 20x20 mm area was not realized due to imperfections in sample and experimental setup. These include Stamp feature height non-uniformity, non-uniform inking and stamp-substrate alignment.

3. **Transparent conductive electrodes** We demonstrated printing of transparent conductive films with silver nanoparticle inks. There are challenges in sintering these electrodes with line widths $<3\mu$m. This needs further studies. Fig. 7-4 shows the SEM image of printed and sintered honeycomb patterns. This is likely due to non-uniform printing as the images show continuous sintered regions where the lines meet and dewetted regions otherwise. This leads to discontinuities. Printing experiments were performed with aqueous silver nanoparticle inks from Novacentrix. The print (Fig. 7-5) show good replication

of stamp patterns and the effectiveness of flash sintering process has not yet been studied.
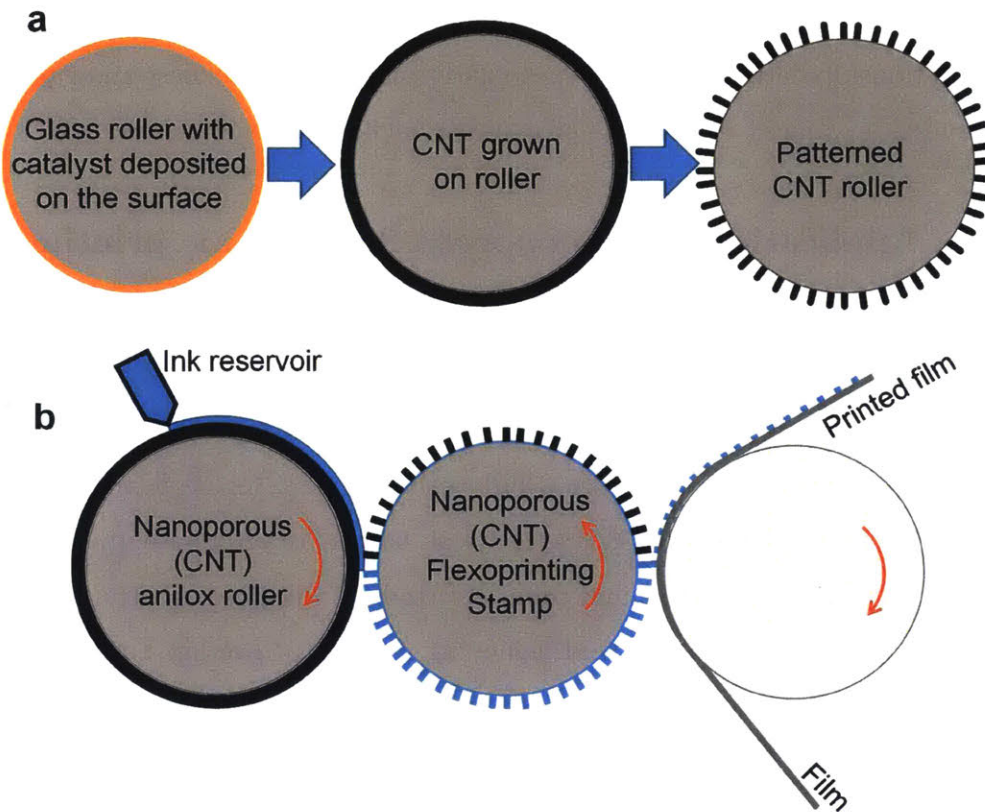
Figure 7-3: Nanoporous stamp roller for flexographic printing

7.2.3 Scaling the process

1. **Nanoporous flexographic stamp roller** The experiments presented in this thesis were conducted with nanoporous stamps fabricated on silicon wafers. Industrial scale flexography stamps are typically on rollers to enable continuous high-throughput manufacturing. Nanoporous stamps on rollers (Fig. 7-3) can be made either by growing CNTs on copper foils and then wrapping the copper foils around rigid rollers or by growing CNTs on quartz rollers.

2. **Wafer size nanoporous stamp** The stamps used in the studies presented in
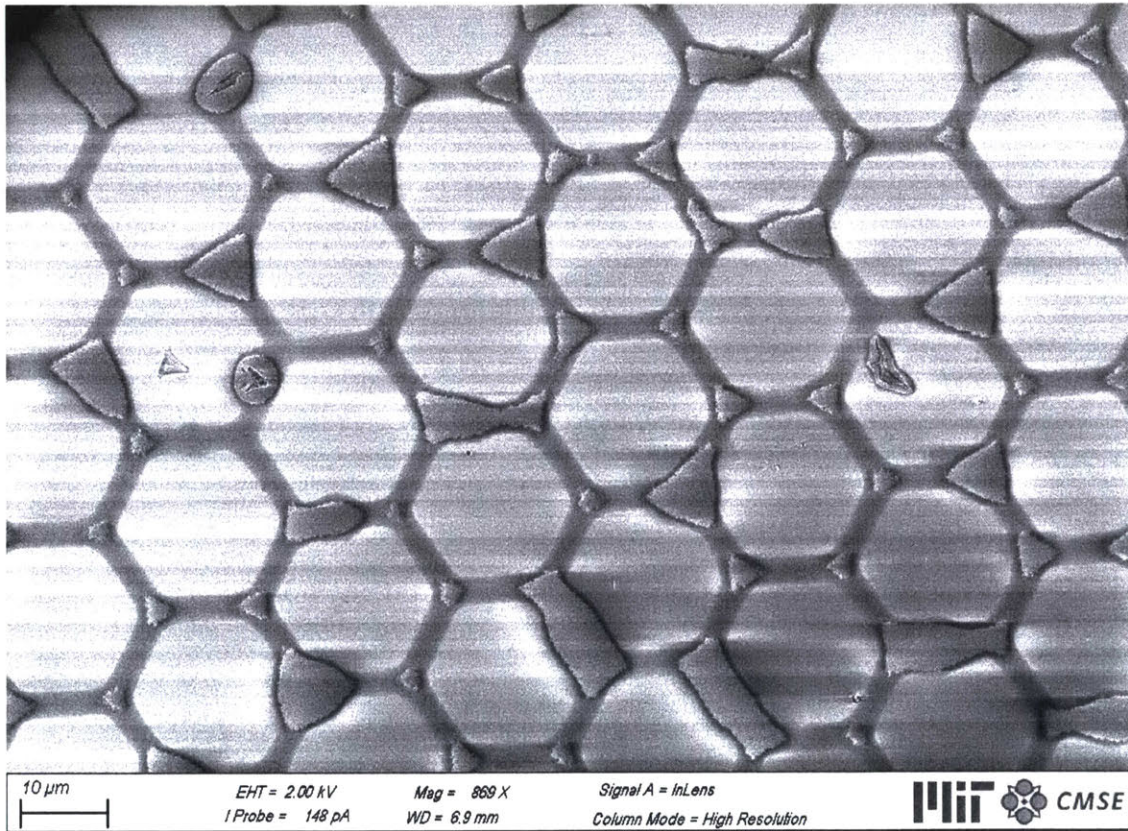
Figure 7-4: SEM image of printed and sintered honeycomb patterns (Print number = 23,Sintering temperature=300 ^{0}C and time = 15 seconds
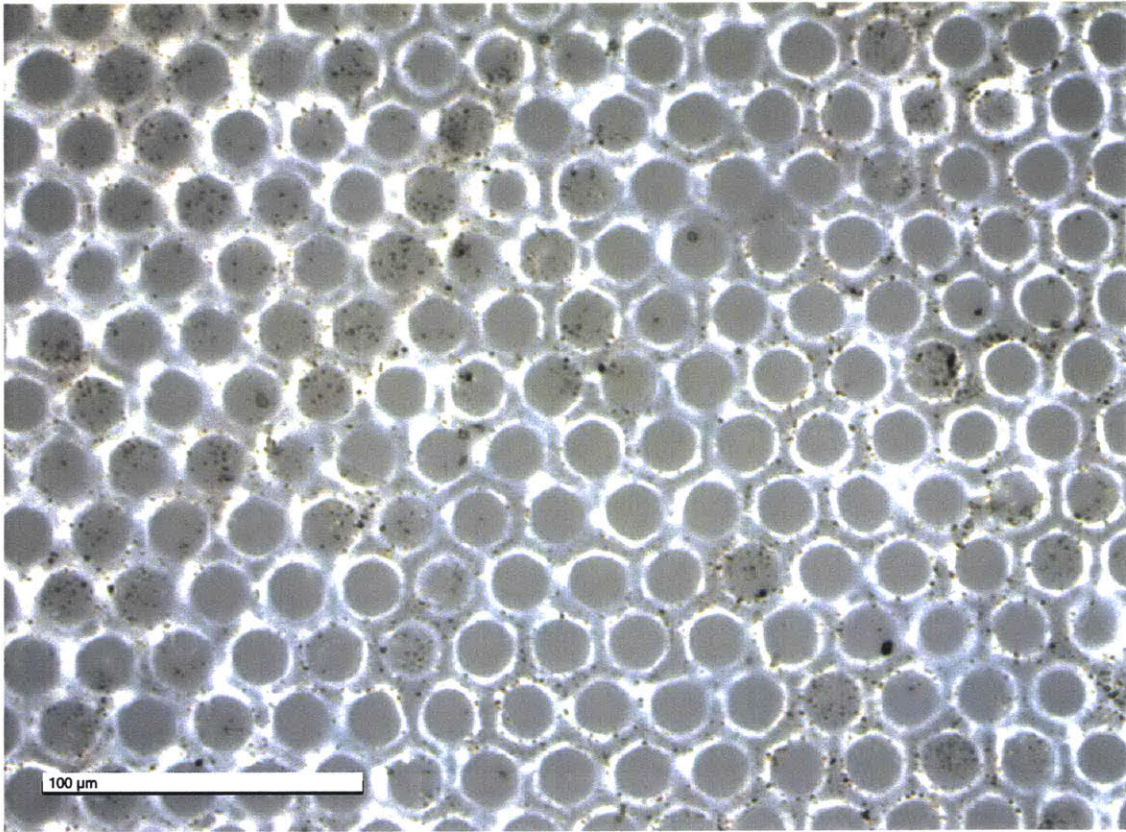
Figure 7-5: Optical microscope image of printed honeycomb patterns (Print number = 2)

this thesis were < 25x25mm size. The tube furnace used in the CVD process for growing CNTs is 1" in diameter and this limits the size of the nanoporous stamps that can be fabricated currently. Using commercially available systems (Aixtron Black Magic) and making 4-6" wafer size CNT stamps will enable larger size application demonstrations of commercial interest (example : TFT arrays).

Appendix A

Microscope for High Speed Imaging

1. **Magnification of the system** $M = \frac{h_i}{h_o} = \frac{f_2}{EFL}$

2. **Effective Focal Length** For the infinity corrected objective, effective focal length can be calculated from RTL and its magnification. For example, the microscope designed for high speed imaging of ink transfer uses a Mitutoyo objective with RTL =200 and magnification = 20 $EFL = \frac{RTL}{M}$

Figure A-1: Schematic of the Microscope used in the High Speed Imaging System

Appendix B

Masks

The mask design files are located in the Mechanosynthesis group masks folder.

20 mm
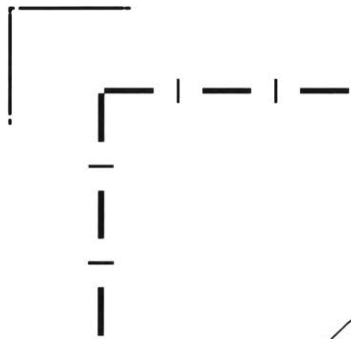
4″ wafer

inch wafer QR Codes.pdf

4" wafer
Dhanush, 03102019

20 mm

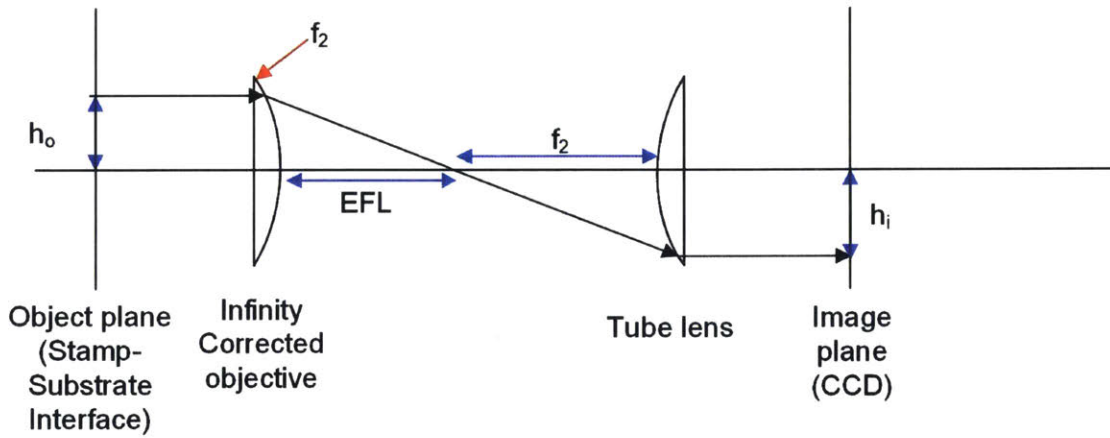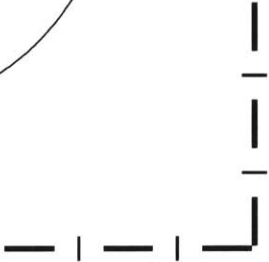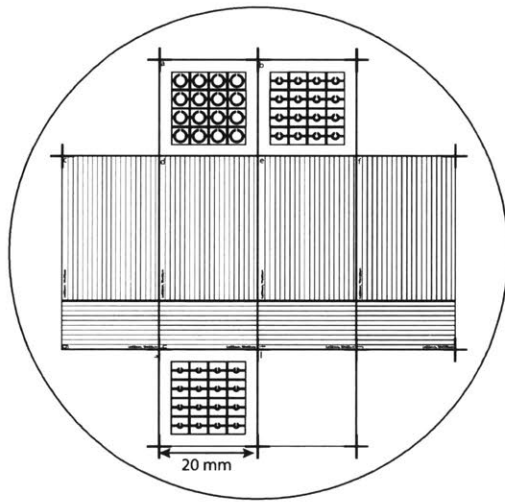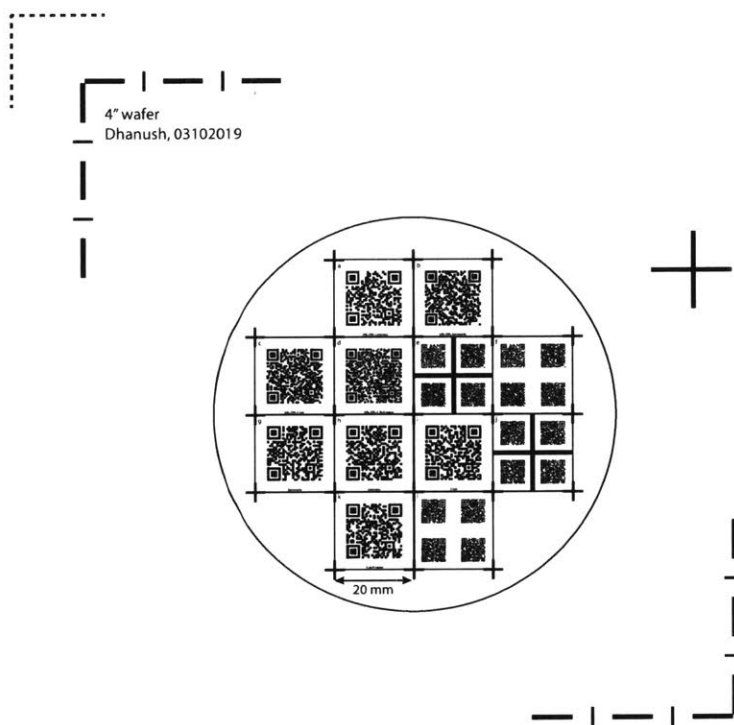Figure B-2: Mask design for fabrication of nanoporous stamp to print QR Codes. File name : 4 inch wafer QR Codes.ai

Appendix C

List of Videos

The videos listed here are available as supporting information of our article [18]

1. **S1-approach-10mmpersec-1fps** The video (capture rate : 10kfps, playing rate : 1 fps) shows the liquid spreading on the substrate when the stamp approaches it at the speed of 10 mm/sec. The stamp consists of circles of 100 microns diameter and separated by 30 microns.

2. **S2-retract-10mmpersec-10fps** The video (capture rate : 10kfps, playing rate : 1 fps) shows the evolution of the liquid bridge when the stamp retracts from the substrate at the retraction speed of 10mm/sec. The stamp consists of circles of 100 microns diameter and separated by 30 microns.

3. (a) **S3a-circle-approach-1fps** (capture rate : 10kfps, playing rate : 1 fps)

   (b) **S3b-circle-retract-before-rupture-10fps** (capture rate : 10kfps, playing rate : 10 fps)

   (c) **S3c-circle-retract-after-rupture-10fps** (capture rate : 10kfps, playing rate : 10 fps)

   These three videos show the (steps 1-8 outlined in Figure 3) liquid spreading during contact, liquid bridge evolution and rupture during retraction, and drop respreading on the substrate when the printing experiment is conducted with a circular stamp.

4. (a) **S4a-annulus-approach-100fps**(capture rate : 1kfps, playing rate : 100 fps)

   (b) **S4b-annulus-retract-before rupture-10fps**(capture rate : 1kfps, playing rate : 10 fps)

   (c) **S4c-annulus-retract-after rupture-1000fps**(capture rate : 1kfps, playing rate : 1k fps)

   These three videos show the (steps 1-8 outlined in Figure 3) liquid spreading during contact, liquid bridge evolution and rupture during retraction, and drop respreading on the substrate when the printing experiment is conducted with a stamp of annular cross section.

5. (a) **S5a-approach-Squares-10fps**(capture rate : 1kfps, playing rate : 10 fps)

   (b) **S5b1-retract-Squares-1000fps**(capture rate : 1kfps, playing rate : 1k fps)

   (c) **S5b2-retract-Squares-1000fps**(capture rate : 1kfps, playing rate : 1k fps)

   These three videos show the (steps 1-8 outlined in Figure 3) liquid spreading during contact, liquid bridge evolution and rupture during retraction, and drop respreading on the substrate when the printing experiment is conducted with a stamp of square cross section.

6. **S6a-point1mmpersec-approach-100fps**(capture rate : 1kfps, playing rate : 100 fps) The video shows the liquid spreading on the substrate when the stamp approach speed is 0.1 mm/sec.

7. **S6b-1mmpersec-approach-100fps**(capture rate : 1kfps, playing rate : 100 fps) The video shows the liquid spreading on the substrate when the stamp approach speed is 1 mm/sec.

8. **S6c-10mmpersec-approach-1fps**(capture rate : 10kfps, playing rate : 1 fps) The video shows the liquid spreading on the substrate when the stamp approach speed is 10 mm/sec.

9. **S6d-50mmpersec-approach-10fps**(capture rate : 25kfps, playing rate : 10 fps) The video shows the liquid spreading on the substrate when the stamp approach speed is 50 mm/sec.

10. **S7a-point1mmpersec-retract-100fps**(capture rate : 1kfps, playing rate : 100 fps) The video shows the base of the liquid bridge on the substrate when the stamp retracts at a speed of 0.1 mm/sec.

11. **S7b-1mmpersec-retract-10fps**(capture rate : 1kfps, playing rate : 10 fps) The video shows the base of the liquid bridge on the substrate when the stamp retracts at a speed of 1 mm/sec.

12. **S7c1-10mmpersec-retract-before-rupture-10fps**(capture rate : 10kfps, playing rate : 10 fps) The video shows the base of the liquid bridge on the substrate before rupture when the stamp retracts at a speed of 10 mm/sec.

13. **S7c2-10mmpersec-retract-after-rupture-10fps**(capture rate : 10kfps, playing rate : 10 fps) The video shows the base of the liquid bridge on the substrate after rupture when the stamp retracts at a speed of 10 mm/sec.

14. **S7d-50mmpersec-retract-100fps**(capture rate : 25kfps, playing rate : 100 fps) The video shows the base of the liquid bridge on the substrate when the stamp retracts at a speed of 50 mm/sec.

Bibliography

[1] K. Flamm, "Measuring Moore's Law: Evidence from Price, Cost and Quality Indexes," *National Bureau of Economic Research*, pp. 1–46, 2018.

[2] A. Kato, "Chronology of Lithography Milestones," *Program*, no. May, 2007.

[3] Y. Khan, M. Garg, Q. Gui, M. Schadt, A. Gaikwad, D. Han, N. A. Yamamoto, P. Hart, R. Welte, W. Wilson, S. Czarnecki, M. Poliks, Z. Jin, K. Ghose, F. Egitto, J. Turner, and A. C. Arias, "Flexible Hybrid Electronics: Direct Interfacing of Soft and Hard Electronics for Wearable Health Monitoring," *Advanced Functional Materials*, vol. 26, no. 47, pp. 8764–8775, 2016.

[4] Y. H. Jung, H. Zhang, S. J. Cho, and Z. Ma, "Flexible and Stretchable Microwave Microelectronic Devices and Circuits," *IEEE Transactions on Electron Devices*, vol. 64, no. 5, pp. 1881–1893, 2017.

[5] G. Grau, J. Cen, H. Kang, R. Kitsomboonloha, W. J. Scheideler, and V. Subramanian, "Gravure-printed electronics: Recent progress in tooling development, understanding of printing physics, and realization of printed devices," *Flexible and Printed Electronics*, vol. 1, no. 2, 2016.

[6] A. E. Ostfeld, I. Deckman, A. M. Gaikwad, C. M. Lochner, and A. C. Arias, "Screen printed passive components for flexible power electronics," *Scientific Reports*, vol. 5, pp. 1–11, 2015.

[7] S. Khan, L. Lorenzelli, and R. S. Dahiya, "Technologies for printing sensors and electronics over large flexible substrates: A review," *IEEE Sensors Journal*, vol. 15, no. 6, pp. 3164–3185, 2015.

[8] C. Cao, J. B. Andrews, A. Kumar, and A. D. Franklin, "Improving Contact Interfaces in Fully Printed Carbon Nanotube Thin-Film Transistors," *ACS Nano*, vol. 10, no. 5, pp. 5221–5229, 2016.

[9] Y. Takeda, K. Hayasaka, R. Shiwaku, K. Yokosawa, T. Shiba, M. Mamada, D. Kumaki, K. Fukuda, and S. Tokito, "Fabrication of Ultra-Thin printed organic TFT CMOS logic circuits optimized for low-voltage wearable sensor applications," *Scientific Reports*, vol. 6, no. April, pp. 1–9, 2016.

[10] J. Kim, J. Oh, K.-M. Jung, K. Park, Y.-S. Kim, and J.-H. Jeon, "Ultrathin Flexible Thin Film Transistors with CYTOP Encapsulation by Debonding Process," *Semiconductor Science and Technology*, 2019.

[11] K. Fukuda and T. Someya, "Recent Progress in the Development of Printed Thin-Film Transistors and Circuits with High-Resolution Printing Technology," *Advanced Materials*, vol. 29, no. 25, 2017.

[12] R. C. Kattumenu, "Flexography printing of silver based conductive inks on packaging substrates," *Western Michigan University. Department of Paper Engineering, Chemical Engineering and Imaging*, 2008.

[13] A. A. Darhuber, S. M. Troian, and S. Wagner, "Physical mechanisms governing pattern fidelity in microscale offset printing," *Journal of Applied Physics*, vol. 90, no. 7, pp. 3602–3609, 2001.

[14] J. Johnson, *Aspects of Flexographic Print Quality and Relationship to some Printing Parameters*, vol. PhD Thesis. 2008.

[15] S. Kumar, "Liquid Transfer in Printing Processes: Liquid Bridges with Moving Contact Lines," *Annual Review of Fluid Mechanics*, vol. 47, no. 1, pp. 67–94, 2015.

[16] S. Kim, H. Sojoudi, H. Zhao, D. Mariappan, G. H. McKinley, K. K. Gleason, and A. J. Hart, "Ultrathin high-resolution flexographic printing using nanoporous stamps," *Science Advances*, vol. 2, p. e1601660, dec 2016.

[17] H. Sojoudi, S. Kim, H. Zhao, R. K. Annavarapu, D. Mariappan, A. J. Hart, G. H. McKinley, and K. K. Gleason, "Stable Wettability Control of Nanoporous Microstructures by iCVD Coating of Carbon Nanotubes," *ACS Applied Materials and Interfaces*, vol. 9, no. 49, pp. 43287–43299, 2017.

[18] D. D. Mariappan, S. Kim, M. S. Boutilier, J. Zhao, H. Zhao, J. Beroz, U. Muecke, H. Sojoudi, K. Gleason, P. T. Brun, and A. J. Hart, "Dynamics of Liquid Transfer from Nanoporous Stamps in High-Resolution Flexographic Printing," *Langmuir*, vol. 35, no. 24, pp. 7659–7671, 2019.

[19] D. Mariappan, S. Kim, and A. Hart, "Plate to roll apparatus for flexography using nanoporous stamps," in *Proceedings - ASPE 2016 Spring Topical Meeting: Precision Mechatronic System Design and Control*, 2016.

[20] S. Kim, H. Sojoudi, H. Zhao, D. Mariappan, G. H. McKinley, K. K. Gleason, and A. J. Hart, "Ultrathin high-resolution flexographic printing using nanoporous stamps," *Science Advances*, vol. 2, p. e1601660, dec 2016.

[21] M. Gupta and K. K. Gleason, "Initiated chemical vapor deposition of poly(1H,1H,2H,2H-perfluorodecyl acrylate) thin films," *Langmuir*, vol. 22, no. 24, pp. 10047–10052, 2006.

[22] J. Li, M. Bedewy, A. O. White, E. S. Polsen, S. Tawfick, and A. John Hart, "Highly Consistent Atmospheric Pressure Synthesis of Carbon Nanotube Forests by Mitigation of Moisture Transients," *Journal of Physical Chemistry C*, vol. 120, no. 20, pp. 11277–11287, 2016.

[23] C. M. Homenick, R. James, G. P. Lopinski, J. Dunford, J. Sun, H. Park, Y. Jung, G. Cho, and P. R. Malenfant, "Fully Printed and Encapsulated SWCNT-Based Thin Film Transistors via a Combination of R2R Gravure and Inkjet Printing," *ACS Applied Materials and Interfaces*, vol. 8, no. 41, pp. 27900–27910, 2016.

[24] P. M. Grubb, H. Subbaraman, S. Park, D. Akinwande, and R. T. Chen, "Inkjet printing of high performance transistors with micron order chemically set gaps," *Scientific Reports*, vol. 7, no. 1, pp. 1–8, 2017.

[25] J. Park, M. Kim, S. W. Yeom, H. J. Ha, H. Song, Y. Min Jhon, Y. H. Kim, and B. K. Ju, "Flexible ambipolar organic field-effect transistors with reverse-offset-printed silver electrodes for a complementary inverter," *Nanotechnology*, vol. 27, no. 22, 2016.

[26] K. Byun, H. Subbaraman, X. Lin, X. Xu, and R. T. Chen, "A $3\mu m$ channel, inkjet printed CNT-TFT for phased array antenna applications," in *Proceedings of the 2013 IEEE Texas Symposium on Wireless and Microwave Circuits and Systems, WMCS 2013*, 2013.

[27] Y. Zhou, A. Gaur, S.-H. Hur, C. Kocabas, M. a. Meitl, M. Shim, and J. a. Rogers, "p-Channel, n-Channel Thin Film Transistors and pn Diodes Based on Single Wall Carbon Nanotube Networks," *Nano Letters*, vol. 4, no. 10, pp. 2031–2035, 2004.

[28] B. R. Want, "Automating Everything," 2003.

[29] Y. Kim, A. Chortos, W. Xu, Y. Liu, J. Y. Oh, D. Son, J. Kang, A. M. Foudeh, C. Zhu, Y. Lee, S. Niu, J. Liu, R. Pfattner, Z. Bao, and T. W. Lee, "A bioinspired flexible organic artificial afferent nerve," *Science*, vol. 360, no. 6392, pp. 998–1003, 2018.

[30] D. Kuzum, H. Takano, E. Shim, J. C. Reed, H. Juul, A. G. Richardson, J. De Vries, H. Bink, M. A. Dichter, T. H. Lucas, D. A. Coulter, E. Cubukcu, and B. Litt, "Transparent and flexible low noise graphene electrodes for simultaneous electrophysiology and neuroimaging," *Nature Communications*, vol. 5, no. May, pp. 1–10, 2014.

[31] C. MacKin and T. Palacios, "Large-scale sensor systems based on graphene electrolyte-gated field-effect transistors," *Analyst*, vol. 141, no. 9, pp. 2704–2711, 2016.

[32] H. Debéda, C. Lucat, and V. Pommier-Budinger, "Printed Piezoelectric Materials for Vibration-based Damage Detection," *Procedia Engineering*, vol. 168, pp. 708–712, 2016.

[33] R. Søndergaard, M. Hösel, D. Angmo, T. T. Larsen-Olsen, and F. C. Krebs, "Roll-to-roll fabrication of polymer solar cells," *Materials Today*, vol. 15, no. 1-2, pp. 36–49, 2012.

[34] F. C. Krebs, "Fabrication and processing of polymer solar cells: A review of printing and coating techniques," *Solar Energy Materials and Solar Cells*, vol. 93, no. 4, pp. 394–412, 2009.

[35] J. Perelaer, P. J. Smith, D. Mager, D. Soltman, S. K. Volkman, V. Subramanian, J. G. Korvink, and U. S. Schubert, "Printed electronics: the challenges involved in printing devices, interconnects, and contacts based on inorganic materials," *Journal of Materials Chemistry*, vol. 20, no. 39, p. 8446, 2010.

[36] B. L. Allen, P. D. Kichambare, and A. Star, "Carbon nanotube field-effect-transistor-based biosensors," *Advanced Materials*, vol. 19, no. 11, pp. 1439–1451, 2007.

[37] D. Song, F. Zare Bidoky, W. J. Hyun, S. B. Walker, J. A. Lewis, and C. D. Frisbie, "All-Printed, Self-Aligned Carbon Nanotube Thin-Film Transistors on Imprinted Plastic Substrates," *ACS Applied Materials and Interfaces*, vol. 10, no. 18, pp. 15926–15932, 2018.

[38] T. Cosnahan, A. A. Watt, and H. E. Assender, "Modelling of a vacuum metallization patterning method for organic electronics," *Surface and Coatings Technology*, vol. 336, no. August 2017, pp. 128–132, 2017.

[39] P. F. Moonen, I. Yakimets, and J. Huskens, "Fabrication of transistors on flexible substrates: From mass-printing to high-resolution alternative lithography strategies," *Advanced Materials*, vol. 24, no. 41, pp. 5526–5541, 2012.

[40] Y. E. Chadov AV, "Investigation of the transfer of a liquid from one solid surface to another. I. Slow transfer. Method of approximate calculation," *Kolloidn. Zh.*, vol. 41, pp. 700–3, 1979.

[41] S. Kumar, "Liquid Transfer in Printing Processes: Liquid Bridges with Moving Contact Lines," *Annual Review of Fluid Mechanics*, vol. 47, no. 1, pp. 67–94, 2015.

[42] C. A. Yakhnin ED, "Investigation of the transfer of a liquid from one solid surface to another. II. Dynamic transfer," *Kolloidn. Zh.*, vol. 41, pp. 1034–39, 1983.

[43] H. Chen, T. Tang, and A. Amirfazli, "Liquid transfer mechanism between two surfaces and the role of contact angles," *Soft Matter*, vol. 10, no. 15, p. 2503, 2014.

[44] H. Chen, a. Amirfazli, and T. Tang, "Modeling liquid bridge between surfaces with contact angle hysteresis.," *Langmuir : the ACS journal of surfaces and colloids*, vol. 29, no. 10, pp. 3310–9, 2013.

[45] H. Chen, T. Tang, H. Zhao, K.-Y. Law, and A. Amirfazli, "How pinning and contact angle hysteresis govern quasi-static liquid drop transfer," *Soft Matter*, vol. 12, no. 7, pp. 1998–2008, 2016.

[46] H. Chen, T. Tang, and A. Amirfazli, "Fast Liquid Transfer between Surfaces: Breakup of Stretched Liquid Bridges," *Langmuir*, vol. 31, no. 42, pp. 11470–11476, 2015.

[47] H. Chen, T. Tang, and A. Amirfazli, "Effects of surface wettability on fast liquid transfer," *Physics of Fluids*, vol. 27, no. 11, 2015.

[48] C. H. Huang, M. S. Carvalho, and S. Kumar, "Stretching liquid bridges with moving contact lines: Comparison of liquid-transfer predictions and experiments," *Soft Matter*, vol. 12, no. 36, pp. 7457–7469, 2016.

[49] B. Qian and K. S. Breuer, "The motion, stability and breakup of a stretching liquid bridge with a receding contact line," *Journal of Fluid Mechanics*, vol. 666, pp. 554–572, 2011.

[50] W. M. Rohsenow, J. P. Hartnett, and Y. I. Cho, *Handbook of heat transfer media*. 1998.

[51] G. W. Jackson and D. F. James, "The permeability of fibrous porous media," *The Canadian Journal of Chemical Engineering*, vol. 64, no. 3, pp. 364–374, 1986.

[52] H. Zhao, C. Jacob, H. A. Stone, and A. J. Hart, "Liquid Imbibition in Ceramic-Coated Carbon Nanotube Films," *Langmuir*, vol. 32, no. 48, pp. 12686–12692, 2016.

[53] G. H. McKinley, "Visco-Elasto-Capillary Thinning and Break-Up of Complex Fluids," *Polymer*, vol. 2005, no. 05, pp. 1274–1277, 2005.

[54] D. de Gennes, P-G ; Brochard-Wyart, F ; Quéré, *Capillarity and Wetting PhenomenaDrops, Bubbles, Pearls, Waves*. 2002.

[55] L. H. Tanner, "The spreading of silicone oil on horizontal surfaces," *J. Phys. D : Appl. Phys.*, vol. 12, no. 1838, pp. 1473–1485, 1979.

[56] C. Ranfeld, "Wet etching of printed silver layers using an etch resist structured by flexography," 2015.

[57] E. Tamjid and B. H. Guenther, "Rheology and colloidal structure of silver nanoparticles dispersed in diethylene glycol," *Powder Technology*, vol. 197, no. 1-2, pp. 49–53, 2010.

[58] A. Kosmala, R. Wright, Q. Zhang, and P. Kirby, "Synthesis of silver nano particles and fabrication of aqueous Ag inks for inkjet printing," *Materials Chemistry and Physics*, vol. 129, no. 3, pp. 1075–1080, 2011.

[59] C. G. De Kruif, E. M. Van Iersel, A. Vrij, and W. B. Russel, "Hard sphere colloidal dispersions: Viscosity as a function of shear rate and volume fraction," *The Journal of Chemical Physics*, vol. 83, no. 9, pp. 4717–4725, 1985.

[60] D. B. Genovese, "Shear rheology of hard-sphere, dispersed, and aggregated suspensions, and filler-matrix composites," *Advances in Colloid and Interface Science*, vol. 171-172, pp. 1–16, 2012.

[61] J. F. Brady, "The rheological behavior of concentrated colloidal dispersions," *The Journal of Chemical Physics*, vol. 99, no. 1, pp. 567–581, 1993.

[62] Y. Noguchi, T. Sekitani, T. Yokota, and T. Someya, "Direct inkjet printing of silver electrodes on organic semiconductors for thin-film transistors with top contact geometry," *Applied Physics Letters*, vol. 93, no. 4, pp. 1–4, 2008.

[63] L. Shiyong, W. Ning, X. Wencai, and L. Yong, "Preparation and rheological behavior of lead free silver conducting paste," *Materials Chemistry and Physics*, vol. 111, no. 1, pp. 20–23, 2008.

[64] W. J. Tseng and C. N. Chen, "Dispersion and rheology of nickel nanoparticle inks," *Journal of Materials Science*, vol. 41, no. 4, pp. 1213–1219, 2006.

[65] C. N. Chen, C. T. Huang, W. J. Tseng, and M. H. Wei, "Dispersion and rheology of surfactant-mediated silver nanoparticle suspensions," *Applied Surface Science*, vol. 257, no. 2, pp. 650–655, 2010.

[66] T. J. Sadowski and R. B. Bird, "NonNewtonian Flow through Porous Media. I. Theoretical," *Transactions of the Society of Rheology*, vol. 9, no. 2, pp. 243–250, 2002.

[67] R. M. Mckinley, H. Jahns, and W. W. Harris, "Flow in Porous Media," vol. 12, no. 1, pp. 17–20.

[68] D. Mariappan, S. Kim, and A. Hart, "Plate to roll apparatus for flexography using nanoporous stamps," in *Proceedings - ASPE 2016 Spring Topical Meeting: Precision Mechatronic System Design and Control*, 2016.

[69] S. Alem, N. Graddage, J. Lu, T. Kololuoma, R. Movileanu, and Y. Tao, "Flexographic printing of polycarbazole-based inverted solar cells," *Organic Electronics: physics, materials, applications*, vol. 52, no. October 2017, pp. 146–152, 2018.

[70] B. T. Mogg, T. Claypole, D. Deganello, and C. Phillips, "Flexographic printing of ultra-thin semiconductor polymer layers," *Translational Materials Research*, vol. 3, no. 1, p. 015001, 2016.

[71] A. Vena, E. Perret, S. Tedjini, G. E. P. Tourtollet, A. Delattre, F. Garet, and Y. Boutant, "Design of chipless RFID tags printed on paper by flexography," *IEEE Transactions on Antennas and Propagation*, vol. 61, no. 12, pp. 5868–5877, 2013.

[72] "Flexographic printing-assisted fabrication of ZnO nanowire devices," *Nanotechnology*, vol. 24, no. 19, 2013.

[73] D. Valdec, I. Zjakic, and M. Milkovic, "The influence of variable parameters of flexographic printing on dot geometry of pre-printed printing substrate," *Tehnicki Vjesnik*, vol. 20, no. 4, pp. 659–667, 2013.

[74] C. M. Homenick, R. James, G. P. Lopinski, J. Dunford, J. Sun, H. Park, Y. Jung, G. Cho, and P. R. Malenfant, "Fully Printed and Encapsulated SWCNT-Based Thin Film Transistors via a Combination of R2R Gravure and Inkjet Printing," *ACS Applied Materials and Interfaces*, vol. 8, no. 41, pp. 27900–27910, 2016.

[75] J. Park, M. Kim, S.-W. Yeom, H. J. Ha, H. Song, Y. Min Jhon, Y.-H. Kim, and B.-K. Ju, "Flexible ambipolar organic field-effect transistors with reverse-offset-printed silver electrodes for a complementary inverter," *Nanotechnology*, vol. 27, no. 22, p. 225302, 2016.

[76] B. Derby, "Inkjet Printing of Functional and Structural Materials: Fluid Property Requirements, Feature Stability, and Resolution," *Annual Review of Materials Research*, vol. 40, no. 1, pp. 395–414, 2010.

[77] "Lion Precision Capacitance Probe Manual."

[78] "Aerotech Linear Motion Stage Manual."

[79] S. K. Garlapati, M. Divya, B. Breitung, R. Kruk, H. Hahn, and S. Dasgupta, "Printed Electronics Based on Inorganic Semiconductors: From Processes and Materials to Devices," *Advanced Materials*, vol. 30, no. 40, pp. 1–55, 2018.

[80] B. Wang, W. Huang, L. Chi, M. Al-Hashimi, T. J. Marks, and A. Facchetti, "High- k Gate Dielectrics for Emerging Flexible and Stretchable Electronics," *Chemical Reviews*, vol. 118, no. 11, pp. 5690–5754, 2018.

[81] J. Zaumseil, "Single-walled carbon nanotube networks for fl exible and printed electronics," *Semiconductor Science and Technology*, vol. 30, no. 7, p. 74001, 2015.

[82] "Carbon Nanotubes for Thin Film Transistor: Fabrication, Properties, and Applications," *Journal of Nanomaterials*, vol. 2013, pp. 1–16, 2013.

[83] C. Cao, J. B. Andrews, A. Kumar, and A. D. Franklin, "Improving Contact Interfaces in Fully Printed Carbon Nanotube Thin-Film Transistors," 2016.

[84] C. Cao, J. B. Andrews, and A. D. Franklin, "Completely Printed, Flexible, Stable, and Hysteresis-Free Carbon Nanotube Thin-Film Transistors via Aerosol Jet Printing," *Advanced Electronic Materials*, vol. 3, p. 1700057, may 2017.

[85] C. Kocabas, N. Pimparkar, O. Yesilyurt, S. J. Kang, M. A. Alam, and J. A. Rogers, "Experimental and theoretical studies of transport through large scale, partially aligned arrays of single-walled carbon nanotubes in thin film type transistors," *Nano Letters*, vol. 7, no. 5, pp. 1195–1202, 2007.

[86] Y. Zhou, A. Gaur, S. H. Hur, C. Kocabas, M. A. Meitl, M. Shim, and J. A. Rogers, "p-Channel, n-channel thin film transistors and p-n diodes based on single wall carbon nanotube networks," *Nano Letters*, vol. 4, no. 10, pp. 2031–2035, 2004.

[87] P. M. Grubb, F. Mokhtari Koushyar, T. Lenz, A. Asghari, G. Gan, W. Xia, H. Dalir, H. Subbaraman, and R. T. Chen, "High Speed Roll-to-Roll Printable Transistor Enabled by a Pulsed Light Curable CNT Ink," *Journal of Manufacturing and Materials Processing*, vol. 3, no. 2, p. 33, 2019.

[88] M. Yu, H. Wan, L. Cai, J. Miao, S. Zhang, and C. Wang, "Fully Printed Flexible Dual-Gate Carbon Nanotube Thin-Film Transistors with Tunable Ambipolar Characteristics for Complementary Logic Circuits," *ACS Nano*, vol. 12, pp. 11572–11578, 2018.

[89] S. Jang, B. Kim, M. L. Geier, M. C. Hersam, and A. Dodabalapur, "Short Channel Field-Effect-Transistors with Inkjet-Printed Semiconducting Carbon Nanotubes," *Small*, vol. 11, no. 41, pp. 5505–5509, 2015.

[90] J. Vaillancourt, H. Zhang, P. Vasinajindakaw, H. Xia, X. Lu, X. Han, D. C. Janzen, W. S. Shih, C. S. Jones, M. Stroder, M. Y. Chen, H. Subbaraman, R. T. Chen, U. Berger, and M. Renn, "All ink-jet-printed carbon nanotube thin-film transistor on a polyimide substrate with an ultrahigh operating frequency of over 5 GHz," *Applied Physics Letters*, vol. 93, no. 24, 2008.

[91] S. P. Schießl, N. Fröhlich, M. Held, F. Gannott, M. Schweiger, M. Forster, U. Scherf, and J. Zaumseil, "Polymer-sorted semiconducting carbon nanotube networks for high-performance ambipolar field-effect transistors," *ACS Applied Materials and Interfaces*, vol. 7, no. 1, pp. 682–689, 2015.

[92] J. Bao and M. G. Bawendi, "A colloidal quantum dot spectrometer," *Nature*, vol. 523, no. 7558, pp. 67–70, 2015.

[93] J. J. Yoo, D. D. Mariappan, S. Kim, J. Zhao, K. Gleason, M. Bawendi, and A. J. Hart, "Printing Colloidal Quantum Dot Spectrometer using Nanoporous Flexography," in *MRS Fall Meeting Poster Session*, 2018.